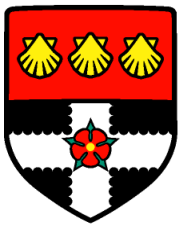

University of Reading

Understanding the historical changes and future projections of summer heatwaves over China under climate change

---

Mingming Zhang

A thesis submitted in fulfilment of the requirements for the degree of

Doctor of Philosophy

PhD Atmosphere, Oceans and Climate

Department of Meteorology

School of Mathematical, Physical and Computational Sciences

January 2025

University of Reading

Declaration

I confirm that this is my own work and the use of all material from other sources has been properly and fully acknowledged.

Mingming Zhang

Abstract

Heatwaves (HWs) are weather events characterized by extreme hot surface air temperature anomalies that persist for several days. This thesis aims to understand the drivers and physical processes of HW changes over different parts of China during the recent decades and their projected changes in the future at different global warming levels (GWLs).

In the recent decades (1995-2020), Compound (hot in day and night) and Nighttime HWs across China and Daytime HWs over central China have increased significantly compared with the period 1961-1994, which is mainly due to increases in seasonal mean warming. The increases of HW properties are predominantly explained by external forcing changes in which greenhouse gas changes play a dominant role and aerosol changes lead to a weak increase (decrease) over Northern (Southern) China.

Climate model projections point to a future in which China faces an increased frequency, enhanced intensity and extended duration of Compound HWs. Overall, seasonal mean warming dominates HW property changes and it is related to an increase of downward longwave radiation and increase of shortwave radiation (under SSP5-8.5) over eastern China. Shortwave radiation changes tend to play a weaker role for surface warming under SSP3-7.0 than under SSP5-8.5, due to greater aerosol changes under SSP3-7.0. Moreover, there is a considerable model spread in the projected HW property changes with the water vapor feedback and shortwave cloud radiative effect being two important factors.

During summer 2022, a record-breaking heatwave occurred over eastern China. The anthropogenic influences and the likely future changes of a similar event are assessed using climate model simulations. Anthropogenic forcings have increased likelihood of the 2022-like summer heatwave event by about 3 times relative to the world with natural forcings. Climate model projections show that the likelihood of such an extreme event over eastern China increases exponentially with increasing GWL.

Acknowledgements

First of all, I would like to thank all my PhD supervisors: Buwen Dong, Jon Robson and Reinhard Schiemann. I am extremely thankful for your guidance and help during my research period, which encouraged me to finish this thesis. You have always been very patient in giving me suggestions and ideas. I am truly blessed to have this opportunity to learn from you all. I would also like to thank my monitoring committee meeting members: Andy Turner and Laura Wilcox. Thank you for the meeting discussions and giving me so many valuable suggestions about my research. Furthermore, thanks to the Department of Meteorology in Reading to provide me with study environment and resources.

I am really grateful for the help and encouragement from my dear friends. Thank you to Nina and Tianru. When I just arrived in a strange country, although you were affected by jet lag in China, you always accompanied and encouraged me. Thank you to Jingyue, Shiyu, Yaxin and Runhua. It's my pleasure to make friends with you in Reading. The trips we experienced will always be my precious memory. Thanks to Rui for always congratulate me on my birthday. And I would also like to thank Buwen and Buwen's family for inviting me to celebrate the Christmas Day during the last four years.

Last but not least, I would like to thank my family. When I proposed to study abroad, you respected my thought and gave me the greatest support. Thank you so much for always being there and your understanding. I love you so much.

Authorship of papers

This thesis contains two lead-author papers. This first paper (Chapter 3) has been published in *Climate Dynamics*. The second paper (Chapter 5) is under review with *Environmental Research Communications*. The results are unmodified from the submitted/accepted manuscripts. The estimated contributions of the candidate (Mingming Zhang) are listed as below.

Zhang, M., Dong, B., Schiemann, R., Robson, J.,Summer compound heatwaves over China: projected changes at different global warming levels and related physical processes. *Clim Dyn* (2024c). https://doi.org/10.1007/s00382-023-07001-4

Estimated contributions: 85%. Data collection and analysis were performed by MZ. The first draft of this paper was written by MZ. BD, RS and JR helped to revise the manuscript.

Zhang, M., Dong, B., Robson, J., Schiemann, R., Anthropogenic influences on 2022-like summer heatwaves over the Yangtze River valley and projected changes in the likelihood of the event. *Environ Res Commun* (2025), under review.

Estimated contributions: 85%. Data collection and analysis were performed by MZ. The first draft of this paper was written by MZ. BD, RS and JR helped to revise the manuscript.

Contents

Chapter 1

Introduction

1.1 Motivation

1.1.1 The impacts of heatwaves

Heatwaves (HWs) are weather events characterized by extreme hot surface air temperatures that persist for several days (Sun et al., 2014), and thus may lead to devastating effects on human health, agriculture, economy, and natural ecosystems (e.g., Bras et al., 2021; Alizadeh et al., 2022).

At the global scale, previous studies have investigated the severe impacts of HWs on society (Hatvani-Kovacs et al., 2016; Campbell et al., 2018; Chambers et al., 2020; Zhao et al., 2024). Exposed to high temperatures, humans are under the threat of a variety of diseases, including diabetes, asthma, poor mental health, cardiovascular disease and so on (Ebi et al., 2021). Globally, the number of heat-related deaths is about 489,075 from 2000 to 2019. The distribution of heat-related deaths varies geographically, with more than half over Asia (Zhao et al., 2021, Fig. 1.1). HWs and drought are often considered the most damaging climatic stressors for wheat (Zampier et al., 2017). Since around 2000, compound heat and drought extremes have led to up to 30% yield losses, which are closely related with the poor harvests (Lesk et al., 2022). Moreover, Callahan and Mancin (2022) found that intensified extreme heatwaves decrease economic growth in relatively warm tropical regions significantly but have weak influence on economic growth in relatively cool midlatitude regions. During 1992-2013, the cumulative losses have been estimated to be $16-$50 trillion globally due to extreme heat related events.

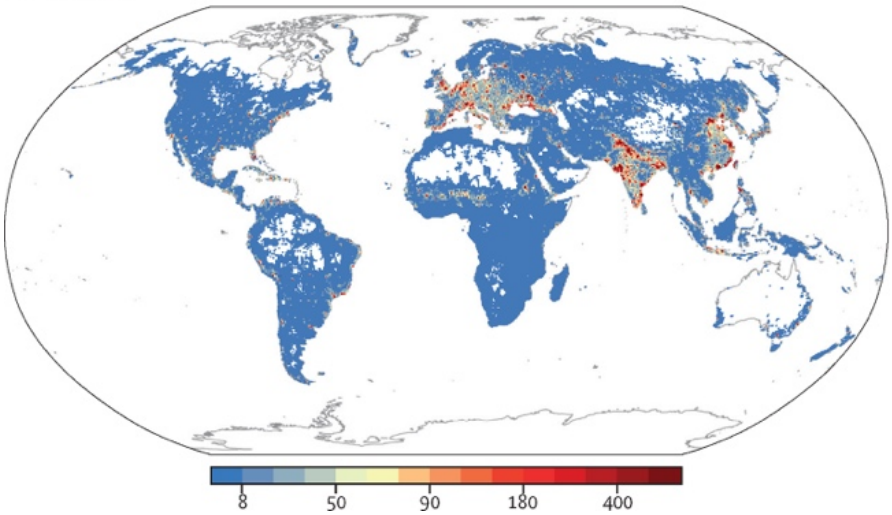

Figure 1.1 Average heat-related annual excess deaths in 2000-19 at a spatial resolution of 0·5° × 0·5°. Figure adapted from Zhao et al. (2021) (Figure 2.c therein)

China is one of the countries which has been strongly influenced by extreme temperatures and frequent HWs (Ding et al., 2010; Ren et al., 2011). Eastern China shows a large number of heat-related deaths compared with other regions (Fig. 1.1). Over the past four decades, the deaths related with HWs have increased dramatically in China, with the record of 26,486 deaths seen in 2017 (Chen et al., 2022). Females, the elderly and people with less education are more vulnerable to HWs (Yang et al., 2019). Zhang et al., (2023b) found that the hazard of compound drought and hot events (CDHEs) has doubled in 1991-2014 compared with 1967-1990. The exposure of croplands to CDHEs increases across China, with the largest relative increase over North China. Due to the impacts of HWs, the total economic losses account for approximately 1%-10% city Gross domestic product (GDP) every year (Wang et al., 2023b).

1.1.2 The historical changes of summer heatwaves over China

To better understand the spatiotemporal characteristics of summer HWs over China, Deng et al. (2019) analyzed the first three leading modes of HWs days, which account for 21.2%, 14.6% and 8.4% of the total variances (Fig. 1.2). The first mode reflects an increased trend in northern China, while the second and third modes represent two distinct interannual variations over the Yangtze River and southern China, respectively (Deng et al., 2019).

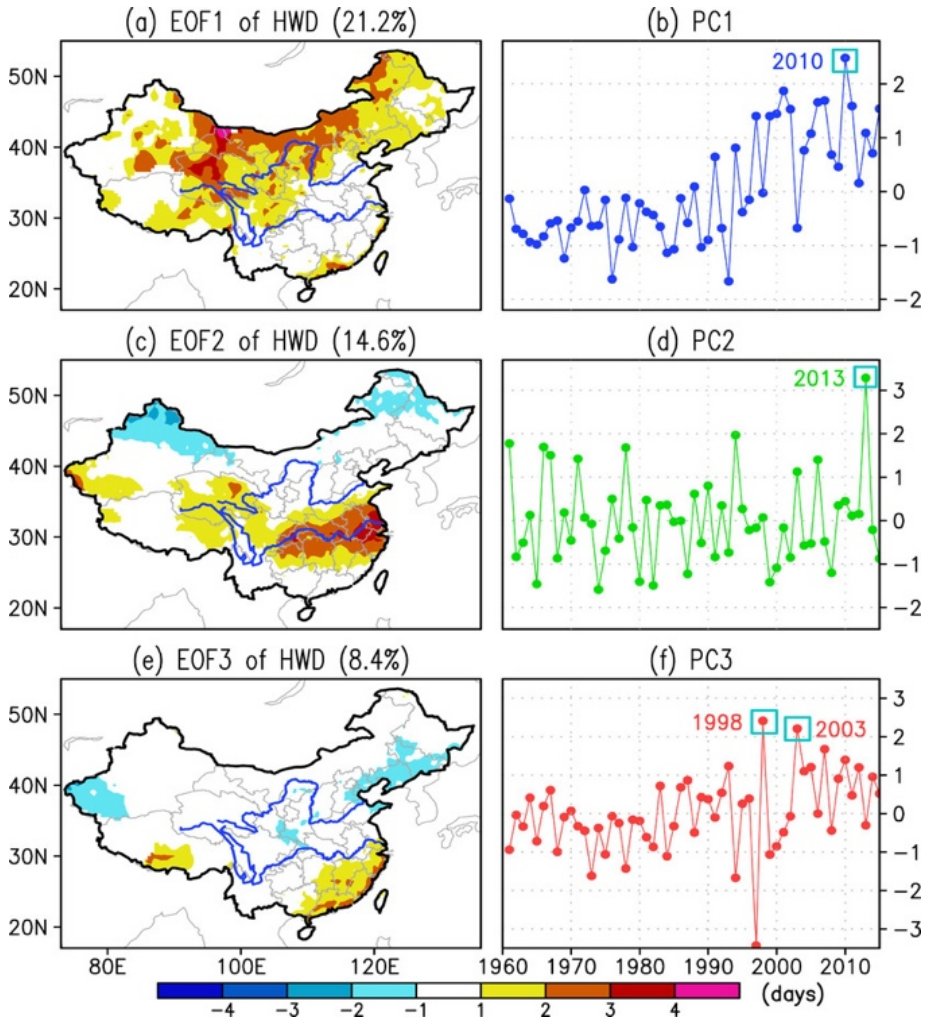

Figure 1.2 (a), (c), (e) The spatial patterns for the first three empirical orthogonal function (EOF) modes of China heatwave day (HWD) during the period of 1961-2015, and (b), (d), (f) the corresponding time series. HWD is identified as the total hot days during each summer. Figure adapted from Deng et al. (2019) (Figure 3 therein).

The first mode shows a pattern with anomalous more HWs occurring over Northwest and Northern China during its positive phase and the corresponding principal component shows an increased trend during the past six decades, which seems to relate to the global warming (Ren et al., 2017). In recent decades, heatwaves (HWs) are indeed becoming more frequent and severe over China as a result of climate change (Sun et al., 2014; Deng et al., 2019; Zhao, 2020; Wang and Yan, 2021). Since the late 1990s, the frequency of the extreme HWs has increased most significantly over North China and central northern China, while the occurrence of mild HWs has increased most significantly over Jianghuai and South China (Xie et al., 2020). The frequency and intensity of regional wet HWs related with both temperature and relative humidity have also increased remarkably since the 1990s (Ding and

Qian, 2011). From the warming acceleration period (1961-1997) to the warming slowdown period (1998-2017), the probability of HWs with both duration and intensity exceeding the 100-yr return levels exhibits an increase by 16% across China (Li et al., 2021). Chen and Li (2017) found that Compound HWs (hot in both daytime and nighttime) and Nighttime HWs increased significantly in frequency, duration, intensity and areal extent during 1961-2010. The frequency of Compound HWs exhibits the largest increasing rate over the eastern China and Northwest China with a significant trend of 0.44 events decade^{-1}, in contrast to an insignificant trend of 0.00 events decade^{-1} for purely Daytime HWs and a significant trend of 0.09 events decade^{-1} for purely Nighttime HWs (An and Zuo, 2021).

The spatial distributions of the second and third modes show strong signal over the Yangtze River region and Southeast China (Fig. 1.2c, e), which mainly show interannual variability of HWs. The third mode shows a dipole pattern characterized by positive (negative) anomalies in Southeast (Northeast) China which is similar to the dipole pattern identified by Zhu et al. (2020). The interannual variability of summer HWs over eastern China also shows decadal-multidecadal fluctuations. During the early period (1979-1993), the second mode with a maximum over the Yangtze River region is the dominant pattern showing large interannual variability. However, the dominant pattern of interannual variability in the recent period (1994-2012) is the north-south dipole pattern (Choi et al., 2020).

In recent years, the extreme heatwave events are more likely to occur over China. Two notable heatwave cases related with the third mode occurred in 1998 and 2003, respectively. During the 1998 heatwave, the daily number of deaths in Shanghai was over three times the summer daily average (Tan et al., 2004). The summer of 2003 also experienced a long heatwave over the Southeast China. Shanghai recorded the hottest summer in 2003 compared with the past 50 years (Tan et al., 2007). During 2022, a record-breaking heatwave event appeared over the regions from the Sichuan Basin to the middle and lower reaches of the Yangtze River valley, which is similar to the second mode. The summer daily maximum temperature (Tmax) showed positive anomalies over this region with anomalies above 6℃ around the mid-August. The intensity of this regional heatwave is the strongest since 1961

(National Climate Center, 2022), which led to that 4.49 million people were in need of subsistence assistance due to the associated drought and 4,284 million hectares of crops had been affected (Ministry of Emergency Management, 2022). This extreme heatwave event is the hottest since 1960 with an estimated return period of at least 100 years (Liang et al., 2024).

In summary, China is facing more frequent, hotter and longer HWs under the influence of global warming, and extreme heatwave events are more likely to occur during recent decades compared to earlier decades. Considering the adverse impacts of HWs on society, it's necessary to systematically study the historical changes of HWs in different parts of China, to understand physical processes, and to assess how heatwaves will change in the future in order to assist the policymakers to mitigate the risks associated with these extremes.

1.2 The definitions of heatwaves

A heatwave is a prolonged period of much-warmer-than-average weather, which typically lasts for several days or a few weeks. Although HWs pose significant risks all over the world, there is no universally generic definition of heatwave (Awasthi et al., 2022).

According to the temperature criterion, the definitions of HWs can be classified into two categories (Wang et al., 2017): one is based on an absolute threshold, which applies a fixed value of temperature. Since exceeding critical temperature thresholds may trigger nonlinear responses or systemic failures in crop yields and human heat tolerance (Perkins and Alexander, 2013; Zhao et al., 2017), heatwaves are commonly defined using absolute threshold in fields as agriculture and human health. Hansen et al. (2008) defined a heatwave, which the Tmax exceeds 35°C for 3 or more consecutive days, to investigate the effect of HWs on mental health in Australia. Similarly, Chen et al. (2013) focused on HWs in China which last for 3 or more days with an absolute threshold of 32°C. To analyze the global HWs, NOAA used a definition which the Tmax exceeds 37°C for a continuous of 2 days or more (NOAA, 2013). In the later Global Climate Reports, NOAA changed the absolute threshold with 33.59°C and 32.65°C for a continuous period of 3 days or more (NOAA, 2016). The differences of using absolute threshold to analyze HWs in previous studies are mainly

manifested in the determination of the magnitude of threshold and the duration of heatwave event.

The other category of the definitions of HWs is based on a relative threshold, which is characterized by a certain number of consecutive days above a fixed percentile of the temperature distribution during the reference local climatology (You et al., 2017). For example, Wang and Yan (2021) used the 90^{th} percentile threshold of Tmax for each calendar day which is determined from the multiyear samples of 15 days over the reference period. Dong et al. (2016) compared the HWs with different intensity in Beijing by using different relative threshold of 90^{th},93^{th} and 95^{th}. Considering the model biases of simulating temperature, researches mostly define HWs by using the relative threshold (Hoffmann et al., 2018; Xu and Zhang, 2022). Furthermore, each grid-box can have its own relative threshold, which is suitable for analyzing the regional scales of HWs.

In recent research, many studies have made some advances in the definition of Compound extreme events (Tripathy et al., 2023; Wang et al., 2023a; Wu et al., 2023a), which is a combination of climatic events that together constitute an extreme event (Baldwin et al., 2019). The impact of Compound extreme events on the natural ecosystems and human society may be more severe than that of the single extreme events (Barichivich et al., 2021). The HWs discussed in previous studies are mainly based on Tmax (Luo et al., 2020; Ullah et al., 2022), whereas Nighttime HWs defined by daily minimum temperature (Tmin) also have impact on human health and society with little to no relief from nighttime cooling (Chen et al., 2014). Compared with the HWs based on only Tmax or Tmin, Compound HWs describe the combined adverse impacts from both Daytime HWs and Nighttime HWs (Chen and Zhai, 2017). Wu et al. (2023a) discussed the local conditions which control the occurrence of these three types of HWs (Fig. 1.3). Daytime HWs are accompanied by increases in solar radiation and decreases in humidity, precipitation, soil moisture and cloud cover. While for Nighttime HWs, the atmosphere becomes moister and cloudier, leading to more longwave radiation emitted to the surface at night, which raises nighttime temperature. All these local conditions are responsible for the Compound HWs. Many recent studies discussed the Compound HWs over China (Xie et al., 2022; Guo et al., 2023; Ding and Chen

2024). For example, Li et al., (2017) defined a heatwave with both hot day and hot night to analyze the variations of Compound HWs over China. A hot day only (night only) is defined as one with Tmax (Tmin) above 90th percentile.

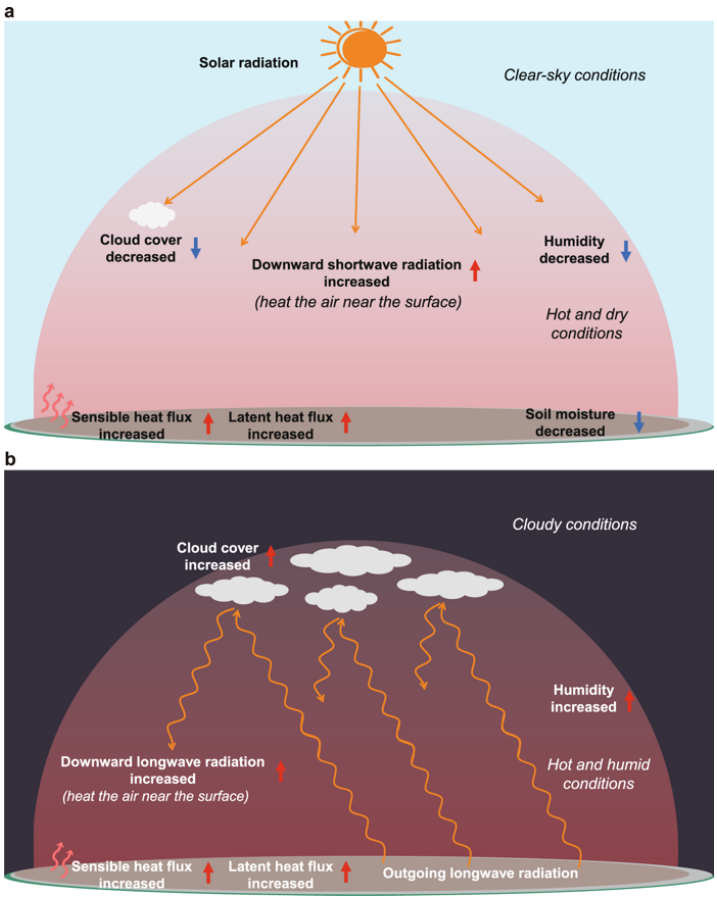

Figure 1.3 The diagram summarizes the physical processes associated with the (a) daytime and (b) nighttime heatwaves. The blue downward arrow indicates a decrease, and the red upward arrow indicates an increase during the heatwave. Figure adapted from Wu et al. (2023a) (Figure 11 therein).

1.3 The factors which are responsible for the changes of heatwaves over China

1.3.1 The factors related to the decadal changes

Anthropogenic forcing has increased the frequency of most extreme HWs around the world (Horton et al., 2015). Anthropogenic forcing includes greenhouse gas, aerosols, and land cover and land usage changes produced by human activities, which mainly contribute to the observed summer temperature over eastern China during 1955-2012 (Sun et al., 2014). The increased greenhouse gases (GHG) forcing largely accounts for the observed decadal trends of summer hot extremes in Northern Hemisphere (Wang et al., 2020). Based on an atmosphere-ocean-mixed-layer coupled model, Chen and Dong (2019) found that the changes in GHG concentrations play the dominant role for the decadal changes of hot

extremes over China and the anthropogenic aerosol (AA) forcing changes lead to decreases in hot extremes over Southeastern China and increases over Northern China via aerosol-radiation interaction and AA induced atmosphere-cloud feedback since mid-1990s. Su and Dong (2019a) discussed the roles of anthropogenic forcing on the decadal changes of Daytime HWs, Nighttime HWs and Compound HWs by using the Met Office Unified Model–Global Ocean Mixed Layer model 1. They found that the GHG changes have dominant influences on all the three types of HWs and the AA changes make significant impacts on Daytime HWs. The increases in GHG lead to the increases of these three types of HWs over China both directly via the strengthened greenhouse effect and indirectly via land-atmosphere and circulation feedbacks. Due to the AA changes, the frequency and intensity of Daytime HWs decrease over Southeastern China and the increase over Northeastern China.

Modes of climate variability can also modulate HWs over China under a warming background. For the abrupt increase of HWs around the mid-1990s, Wei et al. (2023) found the combined impacts of El Niño–Southern Oscillation (ENSO), Atlantic Multidecadal Oscillation (AMO), and Indian Ocean Dipole (IOD) play an important role. Figure 1.4 (Wang et al., 2017) shows the schematic interpretations of ocean-atmosphere interaction. For the decadal changes of HWs over China, the notable warming of sea surface temperature over the Tropical Western Pacific (TPWP) Ocean leads to a significant increase in convective activity in this region. Along with the anomalous convective activity, the increased diabatic heating over the TPWP triggers a northward propagating Rossby wave train along East Asia, which leads to descending motion and less precipitation and thus favors the occurrences of HWs over China. Liang et al. (2022) investigated the contributions of climate change, anthropogenic activities, land surface processes and atmospheric circulation to the decadal changes of HWs over mainland China. Compared with the modes of climate variability, anthropogenic forcing has a dominant contribution to the decadal trends of HWs over China.

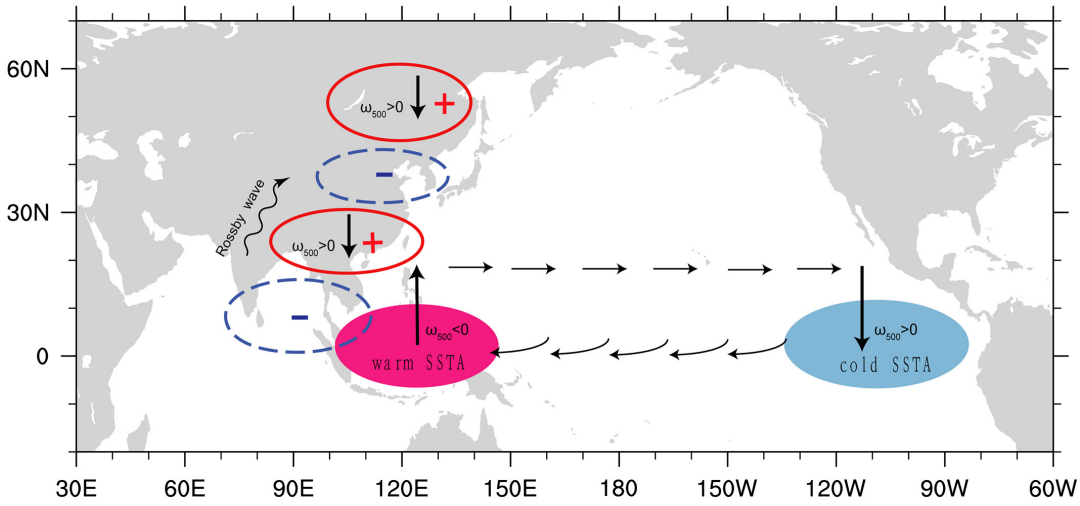

Figure 1.4 Schematic representation of atmospheric response to diabatic heating forcing centered around 120°E at the equator. Positive (+) and negative (−) signs indicate the increased and decreased geopotential height at 500-hPa. Figure adapted from Wang et al. (2017) (Figure 16 therein)

1.3.2 The factors related to the interannual variations

The second and third modes from Fig. 1.2 show the interannual variability of HWs over China. For these two modes, the positive and negative sea surface temperature anomalies over the tropical western and eastern Pacific, respectively, strengthen the Walker circulation and then contribute to convective activity over the TPWP as well (Wang et al., 2017, Fig. 1.4). For the second mode, the extreme temperature events generally occur over the Yangtze River region under the positive phase of the NAO (Zhu et al., 2020). The positive phase of the NAO corresponds to a dipole circulation pattern over the Atlantic Ocean, where the anomalous high pressure extends northeastward from the North Atlantic to northern Russia, then inducing a southeastward propagating wave train over East Asia and anomalous anticyclones over the Yangtze River region (Deng et al., 2019). For the third mode, associated with heatwaves over southern China, is dominated by the Indian Ocean and northwest Pacific warm SSTs owing to the transition phase of El Niño to La Niña (Deng et al., 2019). These warm SST anomalies excite above-normal highs over southern Chian, accompanied by descending air motions, clear skies, decreased precipitation, and increased solar radiation, which jointly cause a drier and hotter soil condition that favors the emergence of daytime HWs (Fig. 1.3, Deng et al., 2019).

1.3.3 The factors related to extreme heatwave events

During the mid-summer of 2013, Central and Eastern China was hit by an extreme heatwave event with the warmest summer on record (Fig. 1.2c, d). This extreme event is associated with a positive 500-hPa geopotential height anomaly. Based on CAM5.1 (MIROC5), the anthropogenic forcing causes a seventeen- (four-)fold increase of the likelihood of this event (Ma et al., 2017). The 2015 summer in western China set the new record for the regionally averaged seasonal temperature. Under the human influence, the probability of occurrence of the 2015 western China extreme heatwave increases at least 42-fold for the highest daily minimum temperature (Sun et al., 2016). The northward movement of the South Asian high (SAH) center dominates this extreme heatwave event over Northwest China (Miao et al., 2016). In July-August of 2022, an extreme heatwave event affected the middle and lower reaches of the Yangtze River. The eastward-shifted SAH and the westward-shifted Western Pacific Subtropical High (WPSH) are the two main drivers of this event. As the SAH extends eastward, the East Asian westerly jet tends to shift northward, which could have caused persistent descending motion over East China (Zhang et al., 2024a). Meanwhile, the westward-shifted WPSH also causes descending motion and widespread warming in southern China (Gong et al., 2024). The anthropogenic forcing and anomalous atmospheric circulation have increased the occurrence probability of this extreme heat by approximately 62.0 and 2.6 times, respectively (Wang et al., 2024).

In summary, the decadal changes of HWs over China are predominantly influenced the anthropogenic forcing. Unforced climate variability mainly contributes to the interannual variability of HWs over China. For the extreme heatwave events, the anthropogenic forcing tends to increase the probability of the occurrence of events and the associated atmospheric circulation anomalies are the dominant driver of the events.

1.4 The future projections of heatwaves over China

As the global mean surface temperature (GMST) increases under different future forcing scenarios, it is expected that there will be an increase of warm extremes over China (Zhou et al., 2014; Hu and Sun, 2020; Chen and Dong, 2021). Based on Weather Research Forecasting (WRF) model simulations, Wang et al. (2019) discussed the future changes of

HWs in future period (2031-2055) relative to the present (1981-2005). There are notable increases in HWs all over China. Stronger HWs with longer duration and stronger intensity will occur more often in the future period. Based on dynamical downscaling simulations using RegCM4, the ensemble results showed that the increasing rates of HWs are 0.33 event per decade for frequency and 0.38°C per decade for magnitude under RCP4.5 scenario over China towards the end of 21st century (Xie et al., 2021). Su and Dong (2019b) investigated the projected changes of Daytime HWs, Nighttime HWs and Compound HWs during the mid-21st century (2045-2055) relative to the present day (1994-2011) under RCP4.5. In the mid-21st century, all three types of HWs will occur more frequently with strengthened intensity and prolonged duration. The Compound HWs increases by 4-5 times in frequency, and twice in intensity and duration. The future changes of Nighttime HWs are larger than those of Daytime HWs. The projection about the probability of the extreme heatwave event is also an important research topic. Wang et al (2024) found that the 2022-like extreme heatwave event over the middle and lower reaches of the Yangtze River is projected to occur almost every 2 years by the 2050s under the SSP5-8.5 or by the 2070s under the SSP2-4.5. The 2022 summer heatwave in the middle reaches of the Yangtze River could occur every 8.5 years by 2070-2100 under the SSP3-7.0 (Hua et al., 2023).

In December 2015, the parties of the United Nations Framework Convention on Climate Change (UNFCCC, 2015) signed the Paris Agreement and proposed a goal as 'holding the increase in the global average temperature to well below 2.0 °C above pre-industrial levels and pursuing efforts to limit the temperature increase to 1.5 °C above pre-industrial levels.'. Therefore, the evaluation of future projections based on target global warming levels, instead of a fixed time period, has become increasingly important. The HWs over China will become more frequent, longer and intensified at the 1.5°C and 2°C GWLs, with the largest increases over Xinjiang and southern China (Yang et al., 2020). Moreover, Raftery et al. (2017) projected that the likely range of GMST increase is 2.0-4.9 °C with a median of 3.2°C by the end of the 21st century. Moreover, Jehn et al. (2022) quantitatively assessed the frequency of mentions related to different GWLs in the IPCC AR6 report. Figure 1.5 (Jehn et al. 2022) revealed that only 14% of temperature-related discussions focus

on GWLs exceeding 2°C, indicating a predominant emphasis on lower GWLs in recent assessments. Jehn et al. (2021) demonstrated that scenarios involving higher-end warming (≥3°C) are substantially underrepresented not only in the IPCC reports but also across the broader climate research literature, suggesting a potential bias toward best-case scenarios. Meanwhile, Fig 1.5 also shows that the using of GWLs rather than specific years provides a more robust, policy-relevant, and scenario-independent basis for future climate projections.

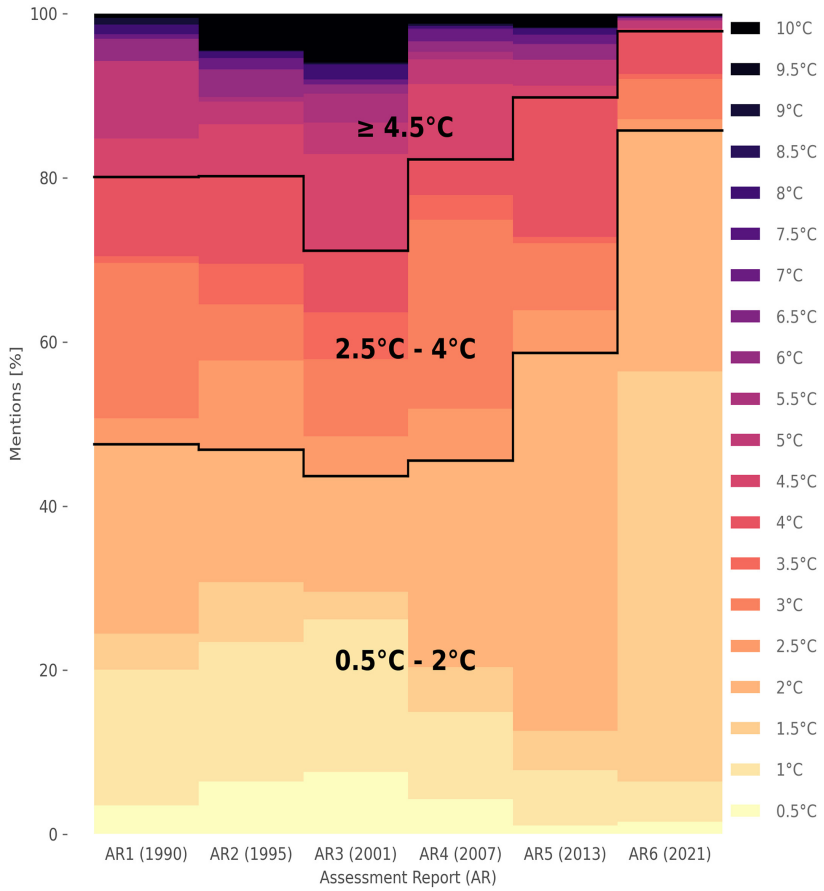

Figure 1.5 Occurrences of temperatures mentioned in the IPCC assessment reports over time. Includes all working group reports, special reports, and synthesis reports published until 11 April 2022 with more than 10 temperature mentions overall. Figure adapted from Jehn et al. (2022) (Figure 1 therein).

1.5 Current knowledge gap on HWs, thesis aim and scientific questions

1.5.1 Current knowledge gap on HWs

According to the occurrence time and different impacts, HWs can be classified into Compound HWs (hot in both day and night), Daytime HWs (hot in day only) and Nighttime HWs (hot in night only) by using relative thresholds (Gershunov et al. 2009; Luo et al. 2022). Based on the observed dataset of 753 stations over China, previous studies found that there

are significant decadal changes in Daytime HWs, Nighttime HWs, and Compound HWs during summer over China across the mid-1990s (Chen and Li, 2017; Su and Dong, 2019a). However, the distribution of the stations in this observed dataset is heterogeneous and there are few stations over the western China. The CN05.2 daily gridded dataset with a 0.5-degree resolution is based on 2416 stations over China managed by the National Climate Center of the China Meteorological Administration (Jiang et al., 2016; Yu et al., 2023). By using this new dataset, it may improve the understanding on the spatial patterns of the historical changes of HWs over China.

The fluctuations of GMST are the joint effects of external forcing and internal variability, particularly on decadal scales (Meehl et al., 2013; Gu et al., 2024). Over the last hundred years, the decadal GMST variations are predominantly governed by external forcing (Dong et al., 2017). Jeong et al. (2024) found that the contributions of external forcing to the warming rate over East Asia increase from -0.2 to 0.1K decade^{-1} from the preindustrial period to until about the 1980s to 0.4K decade^{-1} in the recent decades. The warming of GMST controls the HWs changes across the world (Argueso et al., 2016). Therefore, it's worth to analyze the role of external forcing on the historical changes of HWs in different parts of China and to investigate physical processes.

External forcing involves both natural forcing and anthropogenic external forcings which include GHG forcing, AA forcing, and land cover and land usage changes produced by human activities (Meehl et al., 2012). Some recent studies found that the anthropogenic forcing plays the dominant role for the decadal changes of HWs over China based on single model experiment (Chen and Dong., 2019; Su and Dong, 2019a). However, multi-model methods are needed to address model uncertainties to some extent in detection and attribution studies (Hegerl and Zwiers, 2011). Furthermore, the Coupled Model Intercomparison Project Phase 6 (CMIP6) models provide the most up-to-date simulations of future climate and show a general improvement in simulating extreme climate in China compared with previous phases (Chen et al., 2020). Therefore, to obtain robust conclusions about the roles of GHG forcing and AA forcing on the historical changes of HWs over

different regions of China and to understand physical processes, the multi-model ensemble simulations of CMIP6 models are good resources.

In the future climate, the proportion of compound HWs to the total HW events will increase and be the most frequent one that populations are exposed to (Wang et al., 2020, Xie et al., 2022). However, a very limited number of studies have discussed the future changes of Compound HWs over China during some fixed future time periods (Su and Dong, 2019b; Xie et al., 2022). Considering the increasing importance of the evaluation of future projections based on target GWLs and the high projected GMST by the end of 21st century, it is necessary to focus on the future Compound HWs changes at the target GWLs of 1.5°C, 2°C, 3°C and 4°C to assist the local government in making policy decisions and mitigating the risks associated with these hot extremes. Model uncertainty is one of the important sources of this projection uncertainty (Lehner et al., 2020). Even where there is a general agreement among the models on the projected sign of climate changes due to global warming, the magnitude of the change can vary widely (John et al., 2022). For future projections of HWs over China, most studies show multi-model mean results and have not assessed the model uncertainty in the climate projections (e.g. Zhou et al., 2014; Hu and Sun, 2020). Therefore, the model uncertainty in the projected Compound HWs over China at different GWLs is worth to be investigated.

During summer 2022, the Yangtze River Region experienced a record-breaking heatwave event since 1961, which led to huge losses to crops and economy. Previous studies explored the human influence on this extreme event (Zhang et al., 2023b; Wang et al., 2024). However, the previous studies mainly discussed the role of anthropogenic forcings by comparing the probabilities of this event based on all forcing and natural-only forcing. Considering the components of the anthropogenic forcings, investigating the respective effects of GHG and AA on this event can help us better understand the role of human activity. For the future projections of the probability of this kind of heatwave event, the previous studies focused on the future changes during some fixed periods (such as 2050s, 2070s, 2100s) and the assessment on the variations of the probability of this kind of heatwave event with the increasing GWLs is still lacking.

1.5.2 Thesis aim and scientific questions

The main aim of this thesis is to understand the drivers and physical processes of HWs changes over different parts of China during the recent decades and their projected changes in the future at different GWLs. The thesis focuses on summer period (June-July-August) when HWs are most frequent. Based on observations and CMIP6 multi-model ensemble simulations, this thesis focuses on the following questions:

Q1: How have summer Daytime HWs, Nighttime HWs and Compound HWs changed during the historical period over China? What are the spatial characteristics of these changes?

Q2: What role does the external forcing play on the historical changes of HWs? What are the relative roles of greenhouse gas forcing and aerosol forcing on the historical changes of HWs over China? What are the physical processes responsible for the responses to external forcing and historical changes of HWs?

Q3: How will summer Compound HWs over China change in the future at different global warming levels? What is the model uncertainty in the future projections of summer Compound HWs over China and what are the associated physical processes?

Q4: How does the anthropogenic forcing influence the likelihood of the 2022 extreme HWs over the Yangtze River region? How will the likelihood of this kind of event change in the future at different global warming levels?

1.6 Thesis structure

The remainder of this thesis is structured as follows:

Chapter 2: This chapter presents the observed historical changes of summer Daytime HWs, Nighttime HWs and Compound HWs over China and investigates spatial characteristics of the changes. Based on CMIP6 multi-model ensembles, the role of changes in external forcing on the historical changes of these three types of HWs over China and the relative roles of changes in greenhouse gas forcing and anthropogenic aerosol forcing are investigated. The associated physical processes are elucidated.

Chapter 3: In this chapter, the future changes in frequency, intensity and duration of summer Compound HWs over China at the 1.5°C, 2°C, 3°C and 4°C GWLs under the SSP3-

7.0 and SSP5-8.5 scenarios are assessed and the related physical processes are investigated. This chapter has been published in *Climate Dynamics* (Zhang et al. 2024).

Chapter 4: There is a model uncertainty of the future projections in Compound HWs, which is found from Chapter 3. In this chapter, the models used are classified into high-change models and low-change models and the differences in future changes of summer Compound HWs properties between these two groups of models are discussed and physical processes involved are investigated.

Chapter 5: This chapter analyzes the observed characteristics of the 2022 summer heatwave event and the influence of anthropogenic forcings on the probability of the 2022-like heatwave event. The future projections of the 2022-like summer heatwave events over China at different GWLs are also discussed. This chapter is under review in the journal of *Environmental Research Communications*.

Chapter 6: This chapter summarizes the main conclusions of the thesis, and describes options for future work.

Chapter 2

Understanding the historical changes of summer heatwaves over China

In recent decades, heatwaves (HWs) are becoming more frequent and severe over China (Zhao, 2020; Wang and Yan, 2021), which can lead to severe damage to society. Some recent studies have shown that anthropogenic forcing plays the dominant role for the decadal changes of HWs over China (Chen and Dong, 2019; Su and dong, 2019a). However, these previous studies are mainly based on single model experiments and so the robustness of the conclusions needs to be assessed using multi-model simulations. Therefore, this chapter focuses on addressing **the first two scientific questions**:

i) How have summer Daytime HWs, Nighttime HWs and Compound HWs changed during the historical period over China? What are the spatial characteristics of these changes?

ii) What role does the external forcing play on the historical changes of HWs? What are the relative roles of greenhouse gas forcing and aerosol forcing on the historical changes of HWs over China? What are the physical processes responsible for the responses to external forcing and historical changes of HWs?

This chapter aims to investigate the role of external forcings on the observed historical changes of the three types of summer HWs over China by utilizing the CMIP6 multi-model ensemble to quantify the relative roles of changes in greenhouse gas forcing and anthropogenic aerosol forcing.

2.1 Introduction

Heatwaves (HWs), where the surface air temperature continues to be excessively hot for an extended period of time (Coumou and Rahmstorf, 2012; Seneviratne et al., 2014), which can pose a threat to agriculture, human health, economy and ecosystems (Smoyer-Tomic et al., 2003; Campbell et al., 2018; Callahan et al., 2022; Yin et al., 2023a). For example, the crop losses related to HWs and drought tripled over the last five decades in

Europe (Brás et al., 2021). Furthermore, the total estimated damages attributed to the HWs occurring in four recent hot years (2003, 2010, 2015 and 2018) amounted to 0.3%–0.5% of European GDP, which is 0.5 to 2.5 times more than the averaged losses during the historical period (García-León et al., 2021). Therefore, the significant adverse impacts of HWs highlight the importance of studying HWs.

In recent decades, HWs have become more frequent across the world (Donat et al., 2013; Su and Dong, 2019a; Liao et al., 2021; Perkins-Kirkpatrick and Lewis, 2020; Singh et al., 2021). Regionally, HWs are also becoming more frequent and severe over China (Piao et al., 2010; Ye et al., 2014; Sun et al., 2014; Wang et al., 2017; Zhao, 2020; Wang and Yan, 2021). Since the late 1990s, the frequency of the extreme HWs has increased most significantly over North China and central northern China, while the occurrence of mild HWs has increased most significantly over Jianghuai and South China (Xie et al., 2020). The hottest summer during period 1955-2013 over Eastern China took place in 2013 and the average number of heatwave days was 31 days, which was over twice as many as the climatological average of 1955-1984 (Sun et al., 2014). According to the occurrence time and different impacts, HWs can be divided into Compound HWs (hot in both day and night), Daytime HWs and Nighttime HWs (Gershunov et al., 2009; Luo et al., 2022). Chen and Li (2017) found that Compound HWs and Nighttime HWs increased significantly in frequency, duration, intensity and areal extent during 1961-2010.

The fluctuations of global mean surface temperature (GMST) are the joint effects of external forcing and internal variability, particularly on decadal scales (Meehl et al., 2013; Gu et al., 2024). Over the last hundred years, the decadal GMST variations are dominantly governed by external forcing (Dong et al., 2017). Jeong et al. (2024) found that the contributions of external forcing to the warming rate over East Asia increase from -0.2 to 0.1K decade^{-1} to 0.4K decade^{-1} in the recent decades. About the historical changes of HWs over China, the role of external forcing remains an open question. External forcing involves both natural and anthropogenic external forcings (Meehl et al., 2012). Some recent studies have shown that anthropogenic forcing plays the dominant role for the decadal changes of HWs over China (Freychet et al., 2018; Chen et al., 2019; Su and Dong, 2019a) in which the

greenhouse gas changes influence all three types of HWs and the anthropogenic aerosol has significant impacts on Daytime HWs (Su and Dong, 2019a). However, the previous studies are mainly based on single model experiments and robustness of the conclusions needs to be assessed using multi-model simulations.

The models that contribute to the Coupled Model Intercomparison Project Phase 6 (CMIP6) show a general improvement in simulating extreme climate in China compared with previous phases (Chen et al., 2020). Therefore, in order to get more robust conclusions on the drivers and physical processes governing the observed historical changes of the Compound HWs, Daytime HWs and Nighttime HWs over China, we aim to use the multi-model ensemble mean from CMIP6. This chapter is organized as follow: Section 2.2 introduces the data and methods used. Section 2.3 shows the observed historical changes of heatwaves over China. Section 2.4 discusses the roles of different forcings on the historical changes of heatwaves and the related physical processes are shown in Section 2.5. The conclusions and discussions are summarized in Section 2.6.

2.2 Data and Methods

2.2.1 Data

The daily gridded CN05.2 temperature dataset during 1961-2020 which is derived from the National Meteorological Information Center is used as the observational data with a resolution of 0.5° x 0.5° (Jiang et al., 2016; Yu et al., 2023).

The multimodel simulations from CMIP6 historical all forcing simulations, single forcing simulations from the Detection and Attribution Model Intercomparison Project (DAMIP) and the Scenario Model Intercomparison Project (ScenarioMIP) are used in this study (Eyring et al., 2016). The SSP2-4.5 experiment is used to extend the historical simulations from 2014 to 2020. To analyze the relative roles of different anthropogenic forcings, the hist-GHG and hist-AER experiments during the period 1961-2020 from the DAMIP are used. The simulations from the hist-GHG experiment are forced by well-mixed greenhouse gas changes only and the simulations from the hist-AER experiment are forced by changes in aerosol forcing only (Gillett et al., 2016). The models used are listed in Table 2.1.

Table 2. 1 The list of models used in Chapter 2

	Model	Resolution (lon x lat)	# of Members	
			Historical (1961-2014) SSP2-4.5 (2015-2020)	Hist-GHG Hist-AER (1961-2020)
1	BCC-CSM2-MR	320x160	3	3
2	FGOALS-g3	180x80	1	3
3	CanESM5	128x64	19	10
4	CNRM-CM6-1	256x128	10	3
5	ACCESS-ESM1-5	192x144	3	3
6	ACCESS-CM2	192x144	3	3
7	MIROC6	256x128	10	3
8	IPSL-CM6A-LR	144x143	7	6
9	MRI-ESM2-0	320x160	5	5
10	HadGEM3-GC31-LL	192x145	5	4
11	NorESM2-LM	144x96	3	3

The model outputs of daily minimum temperature (Tmin), average temperature and maximum temperature (Tmax) and monthly radiation and atmospheric circulation variables are analyzed in the following sections. All model data is regridded to a 1.5° × 1.5° grid using bilinear interpolation in order to facilitate the intercomparison.

2.2.2 Methods

In order to define HWs, a relative threshold on each calendar day is calculated as the daily 90th percentile of Tmax or Tmin in summer (June, July, August) based on 15-day samples centered on that day during the baseline period of 1961–1990 (Della-Marta et al., 2007) in observations and CMIP6 historical multi-ensemble simulations. All the HWs are divided into three types:

Compound HWs: at least three consecutive days with simultaneous hot days and hot nights (Tmax ≥ 90^{th} percentile and Tmin ≥ 90th percentile).

Daytime HWs: at least three consecutive hot days (only Tmax ≥ 90th percentile), without consecutive hot nights.

Nighttime HWs: at least three consecutive hot nights (only Tmin ≥ 90th percentile), without consecutive hot days.

The HWs are characterized using their frequency, intensity and duration. The frequency is the number of events within a year. The intensity of each event is calculated by averaging the daily temperature anomalies above the corresponding thresholds within the event. Particularly, the intensity of Compound HWs is the sum of the averaged Tmax and Tmin temperature anomalies above the corresponding thresholds within the event. The intensity for a particular year is computed by averaging the intensity of all events occurring in that year. The duration is defined as the total number of days from the beginning to the end of an event. The HWs properties of each ensemble member are calculated individually relative to its own Tmax 90th percentile and Tmin 90th percentile in order to correct model systematic bias on simulated HW properties. To treat each model equally, the multi-member mean is calculated in each model first and then the multi-model ensemble mean is derived from all models.

2.3 The observed historical changes of summer heatwaves over China

The spatial distributions of the frequency, intensity and duration of Compound HWs, Daytime HWs and Nighttime HWs during the 1961-2020 based on observations are shown in Figure 2.1. The frequency of Compound HWs is the smallest among the three types of HWs (Fig. 2.1a). The largest frequency centers appear over the Tibetan Plateau, Yangtze River and Northwest China. The intensity of Compound HWs over the northern part of China is much larger than the southern area (Fig. 2.1d). The largest intensity appears over Northeast China with a value of 7.69℃. The Compound HWs last much longer over the northeast margin of the Tibetan Plateau and the Yangtze River (Fig. 2.1g). The longest duration of Compound HWs can reach 5.34 days over the Yangtze River.

For Daytime HWs, the frequency over the western China and northern part of Northeast China are larger with the largest frequency of 1.76 events per year (hereafter as events·a^{-1}). Daytime HWs show more intense intensity over the western part of Northeast China (Fig. 2.1e). The largest intensity appears over Northeast China with a value of 2.22℃. The Tibetan Plateau shows longer duration of Daytime HWs with the largest duration of 4.82 days (Fig. 2.1h).

For Nighttime HWs, it appears most frequently over China among the three types of HWs (Fig. 2.1c). The Tibetan Plateau is the most frequent region with the largest frequency of 2 events·a^{-1}. The intensity over Northwest China and Northeast China is more intense than the other regions with the largest intensity of 1.79℃ (Fig. 2.1f). The Nighttime HWs over the Tibetan Plateau have the longest duration with a value of 5.44 days (Fig. 2.1i).

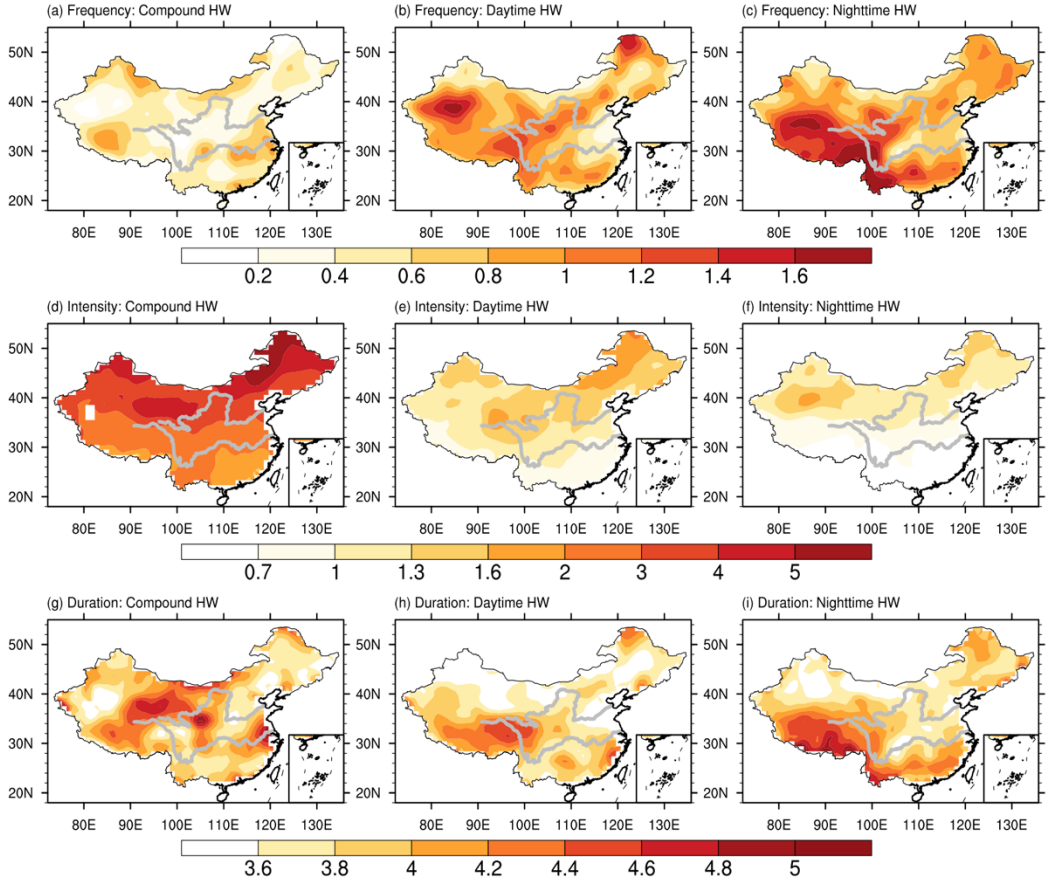

Figure 2.1 The spatial distributions of the summer (JJA) mean frequency (a-c, units: events·a^{-1}), intensity (d-f, units: ℃) and duration (g-i, units: days) of Compound, Daytime, Nighttime HWs during 1961-2020 over China based on CN05.2 observations dataset.

Figure 2.2 shows the time series of how the observed properties of HWs have changed averaged over the entire China. Compound HWs and Nighttime HWs show significant positive trends with an abrupt increase in frequency, intensity, and duration around the mid-1990s. The largest increase in frequency and duration of HWs, as measured by a linear trend fitted over 1960-2020, is found for Nighttime HWs. Daytime HWs also show positive trends during the 1961-2020, but these increases are smaller than for Nighttime or Compound HWs. Indeed, the trends of the frequency and duration of Daytime HWs are non-significant, but there is still an obvious increase in intensity around the mid-1990s. Therefore, the

differences in HWs properties between the period 1995-2020 and the period 1961-1994 are regarded as the historical changes of HWs in the following analysis.

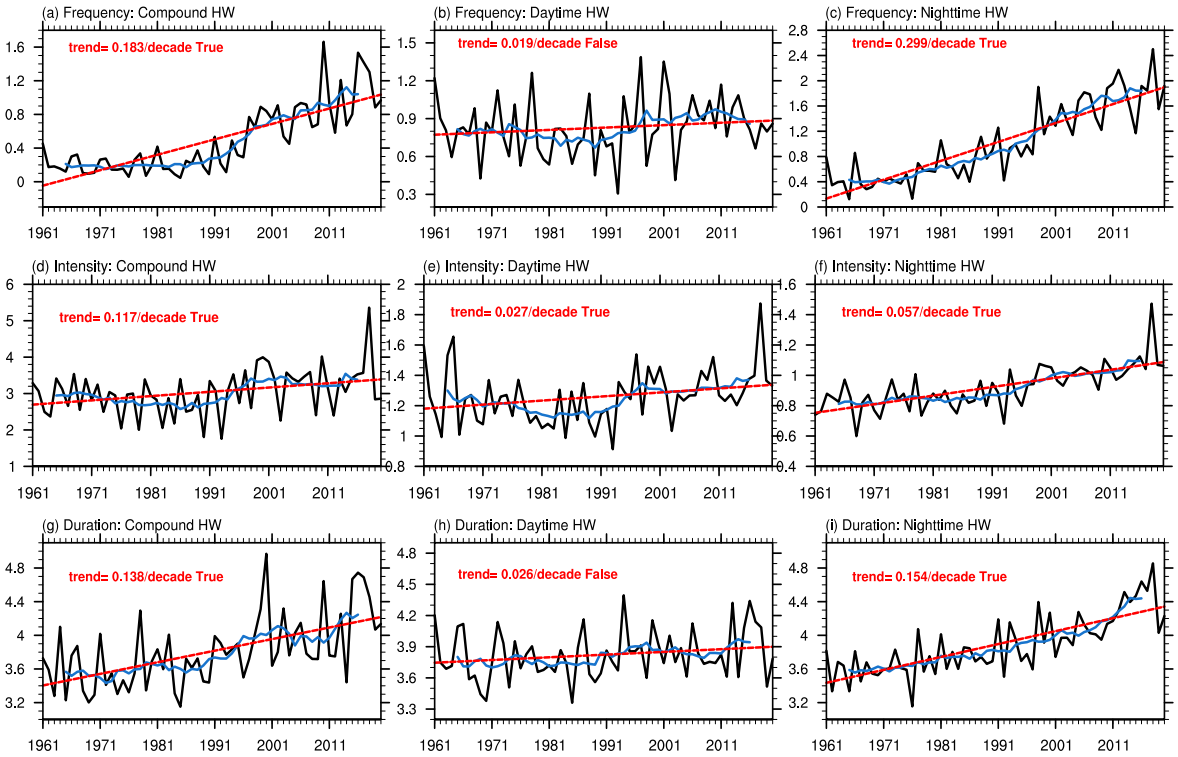

Figure 2.2 The time series of the frequency (a-c, units: events·a^{-1}), intensity (d-f, units: ℃) and duration (g-i, units: days) of Compound, Daytime, Nighttime HWs averaged over the entire China during 1961-2020 (black line) based on observations. Red dashed line is the linear regression line. Blue solid line is the 9-year running mean line. True or False indicates whether the trend is significantly different to 0 at the significance level of 0.05 using a Student's t-test.

Figure 2.3a shows the differences in the mean frequency between the time periods 1995-2020 and 1961-1994 as a function of intensity for Daytime HWs averaged over the entire China. Although there is no increase in frequency of daytime HWs when averaged over the entire China, there is an increase in frequency of the most intense daytime HWs. There are less low-intensity Daytime HWs and more high-intensity Daytime HWs during 1995-2020 than 1961-1994. By classifying the Daytime HWs into high-intensity and low-intensity HWs using the intensity threshold of 1℃, figure 2.3b shows that the frequency trend of high-intensity Daytime HWs do in fact show significant positive trend over 1960-2020, whilst low-intensity Daytime HWs show a non-significant decrease. These results indicate that the non-significant increase in frequency of Daytime HWs over the entire China during 1961-2020 may be caused by the decrease of low-intensity events.

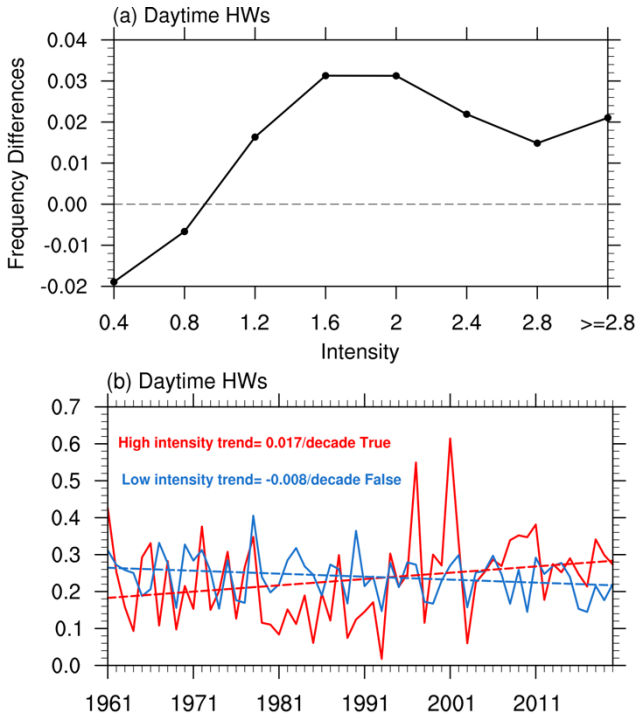

Figure 2.3 (a) The differences in mean frequency of different intensity Daytime HWs averaged over the entire China between 1995-2020 and 1961-1994 (units: events·a^{-1}) based on observations. (b) The time series of the frequency of low (blue line) and high intensity (red line) based on an intensity threshold of 1℃. Daytime HWs averaged over the entire China (units: events·a^{-1}). Dashed lines are the linear regression lines. True or False indicates whether the trend is significantly different to 0 at the significance level of 0.05 using a Student's t-test.

The spatial distributions of historical changes in properties of these three types of HWs are shown in Fig. 2.4, which shows that spatial changes in HW properties are regionally distinct. The frequency changes of Compound HWs show significant positive variations across much of China, except for the regions between the Yangtze River and Yellow River (Fig. 2.4a). The largest increase in frequency appears over the southeastern coastal areas with a value of 2.60 events·a^{-1}. The intensity and duration of Compound HWs increase over most regions of China, especially over the central China and western China with the largest increases of 3.52℃ and 4.07 days (Fig. 2.4d, g). For Daytime HWs, the frequency increases significantly over part regions of the central China, Northwest China and Northeast China (Fig. 2.4b). The intensity over the central China increases significantly during the recent years (Fig. 2.4e). However, the historical changes in HW properties are not very significant in most other regions. For Nighttime HWs, the frequency almost increases significantly over

the entire China, expect for Southeast China (Fig. 2.4c). The largest increase is 3.21 events·a^{-1} over the Tibetan Plateau. The intensity increases most over Northwest China with a value of 0.92℃ (Fig. 2.4f). The historical changes of duration increase across China during the recent years and the largest increase appears over the Tibetan Plateau with a value of 3.30 days (Fig. 2.4i).

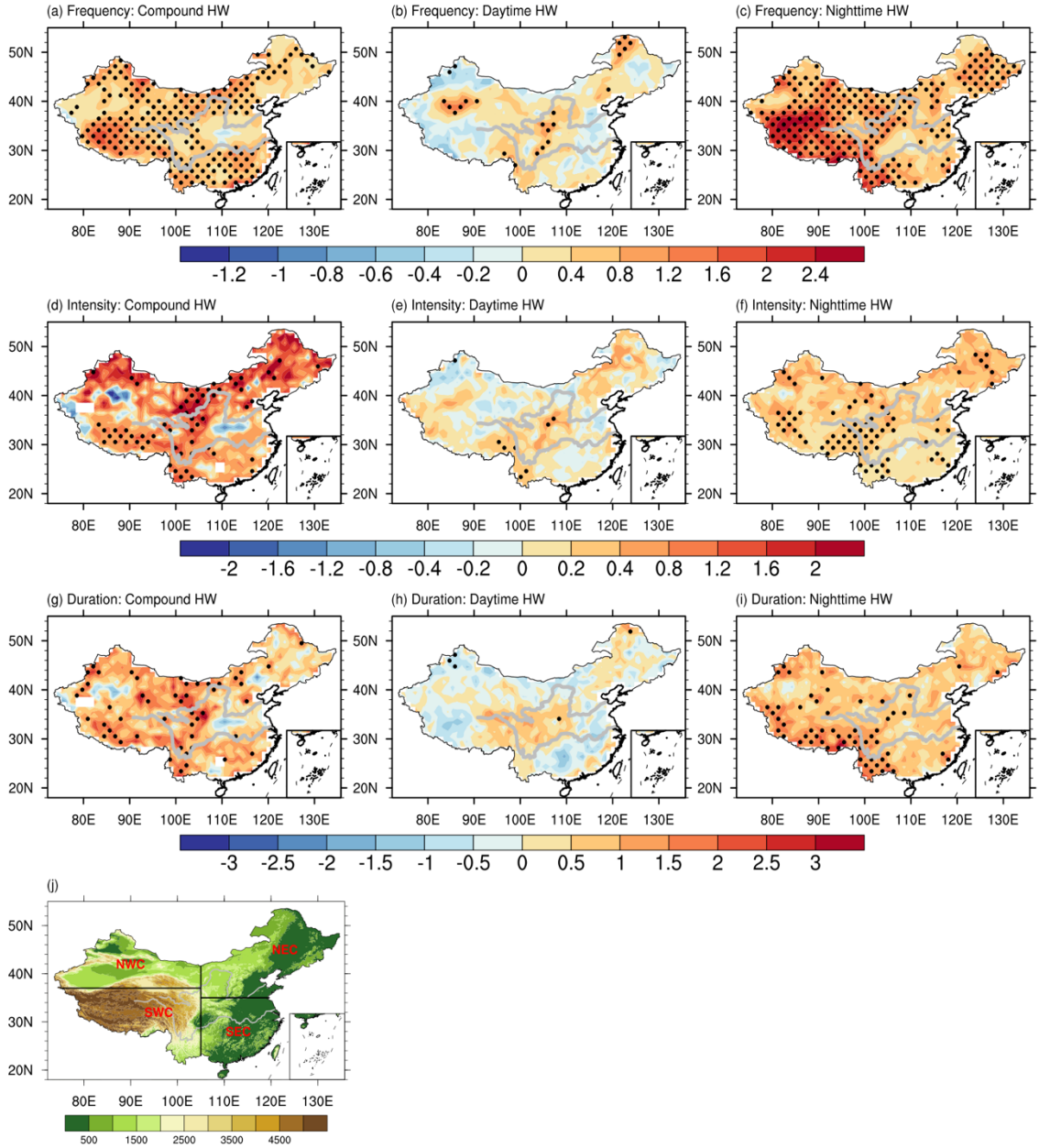

Figure 2.4 The spatial distributions of the differences in frequency (a-c, units: events·a^{-1}), intensity (d-f, units: ℃) and duration (g-i, units: days) of Compound, Daytime, Nighttime HWs between the period 1995-2020 and 1961-1994 based on observations. Black dots represent the regions where the changes are significant at the 0.05 level using a Student's t-test. (j) The topography (units: m) over the study regions. The subregions analyzed in the study are distinguished by black lines and they are Southeast China (SEC), Northeast and North China (NEC), Northwest China (NWC) and Southwest China (SWC).

According to the regional climate and the topography over China (Song et al., 2011), we also quantify the historical changes for four subregions (Fig. 2.4j). These are Northeast and North China (NEC; 35°-54°N, 105°-134.5°E), Southeast China (SEC; 21°-35°N, 105°-123°E), Southwest China (SWC; 21°-37°N, 73°-105°E) and Northwest China (NWC; 37°-50°N, 73°-105°E).

The regionally averaged historical changes of the three types of HWs from the 1961-1994 to 1995-2020 over the entire China and subregions are shown in Fig. 2.5. For frequency (Fig. 2.5a), Compound HWs and Nighttime HWs increase significantly over the entire China and the four subregions during the recent years. Except for SEC, the historical changes of Nighttime HWs are the largest among the three types of HWs. Compared with other subregions, SWC shows the largest increases in frequency of Compound HWs and Nighttime HWs with a value of 0.75 events·a^{-1} and 1.57 events·a^{-1}, respectively. Daytime HWs only increase significantly over NEC.

For intensity (Fig. 2.5b), the historical changes of Compound HWs are the most intense among the three types of HWs across China. The largest increases of Compound HWs and Nighttime HWs appear over NEC and NWC, which are over 1.06℃ and 0.34℃, respectively. The historical changes of these two types of HWs over SEC are the smallest among the subregions. Daytime HWs show significant historical increases over SEC and SWC and the largest increase appear over SWC with a value of 0.17℃.

For duration (Fig. 2.5c), the magnitude of historical changes of Compound HWs and Nighttime HWs over the entire China are similar. SWC exhibits the largest increases of Compound HWs and Nighttime HWs, which can reach over 1 day. The area-averaged historical changes of Daytime HW properties are small, especially for duration and they are non-significant over all regions (Fig. 2.5).

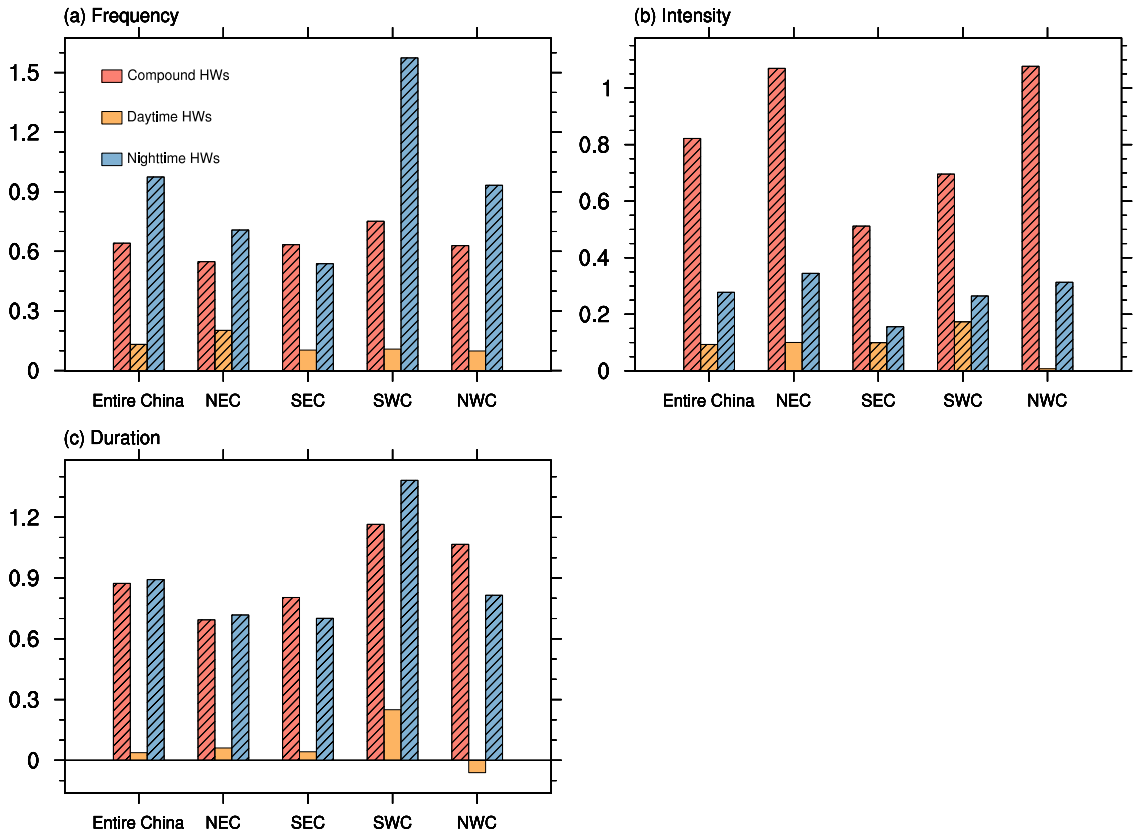

Figure 2.5 The observed area-averaged historical changes in frequency (a, units: events·a^{-1}), intensity (b, units: °C) and duration (c, units: days) of Compound (red bars), Daytime (yellow bars), Nighttime (blue bars) HWs between the period 1995-2020 and 1961-1994 based on a difference pattern. The shaded marks on bars show that the difference between the two periods are significantly different at the significant level of 0.05 based on a Student's t-test.

2.4 The model performance on simulating temperature and heatwaves over China

The above results show that there have been significant observed changes of HWs over China on decadal timescales, especially Compound HWs and Nighttime HWs. To assess the role of external forcings and quantify relative roles of different forcings on the historical changes of these three types of HWs, we use 11 CMIP6 multi-model ensemble historical simulations and DAMIP single forcing simulations. However, to ensure confidence in such attribution results, it is important to first evaluate that these models can successfully simulate the important features of HWs over China.

The ability of the models to simulate Tmax and Tmin climatologies in summer during 1961-2020 are shown in Fig. 2.6 and Fig. 2.7. We find that the models chosen for this study can represent the temperature distribution over China well. For example, the models capture

the spatial distribution of summer Tmax and Tmin (Fig. 2.6), and the pattern correlation coefficients of multi-model ensemble mean can reach 0.95 (Fig 2.7). Furthermore, the spatial variations of most models and the multi-model ensemble mean are close to the reference point (REF), indicating that models show better agreement with observations.

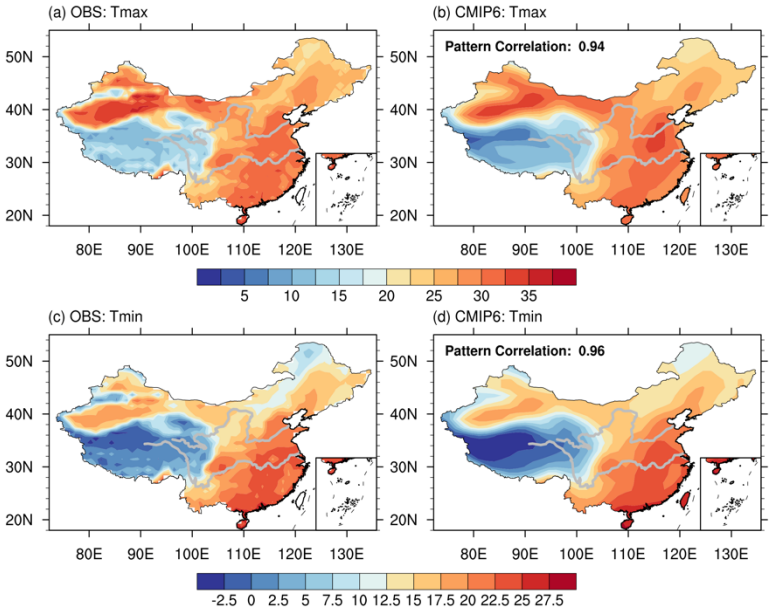

Figure 2.6 The spatial patterns of climatology in summer mean Tmax and Tmin (units: °C) during the historical climate (1961-2020) based on observations and CMIP6 multimodel mean simulations. The pattern correlation coefficients between observation and model in Tmax and Tmin are presented on the top left of (b) and (d).

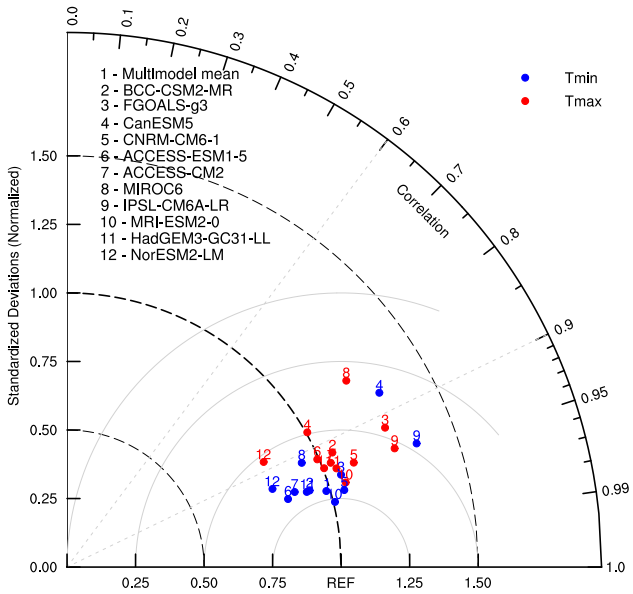

Figure 2.7 The Taylor diagram of climatological-mean spatial distribution of summer mean Tmax and Tmin during 1961-2020 of each CMIP6 model and the multi-model ensemble mean. The x-axis corresponds to the standard deviation axis at perfect correlation (r=1), representing the reference direction for comparing models with observations (Taylor, 2011). The reference point (REF) corresponds to the observational dataset.

The models can largely represent the main characteristics and spatial variations of these three types of HWs in terms of frequency, intensity and duration during the historical period (Fig. 2.8-Fig. 2.10), especially the locations of some high value centers. For example, both model and observation show large frequency and long duration in Nighttime HWs over Southern China. The pattern correlation coefficients of the three properties of Nighttime HWs between observations and the multi-model mean simulations can reach over 0.70. The spatial patterns of intensity of the simulated Compound HWs and Daytime HWs show similar distributions to those based on observations with correlation coefficients of 0.88 and 0.85, respectively. The duration of the observed and simulated Daytime HWs also have similar pattern with a correlation coefficient of 0.71.

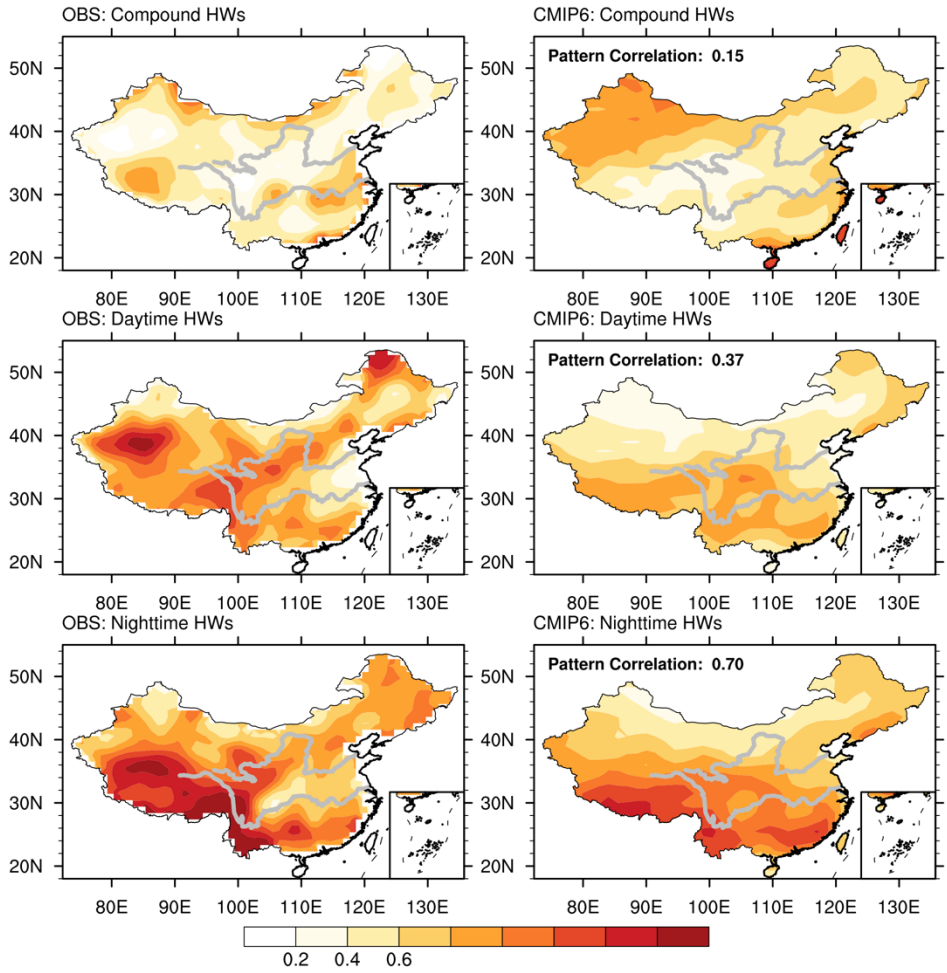

Figure 2.8 The spatial distributions of the summer mean frequency (units: events·a^{-1}) of Compound HWs, Daytime HWs and Nighttime HWs during 1961-2020 over China in observations and CMIP6 multi-model mean historical simulations. The pattern correlation coefficients between observation and model in different HWs are presented on the top left of the simulated panels.

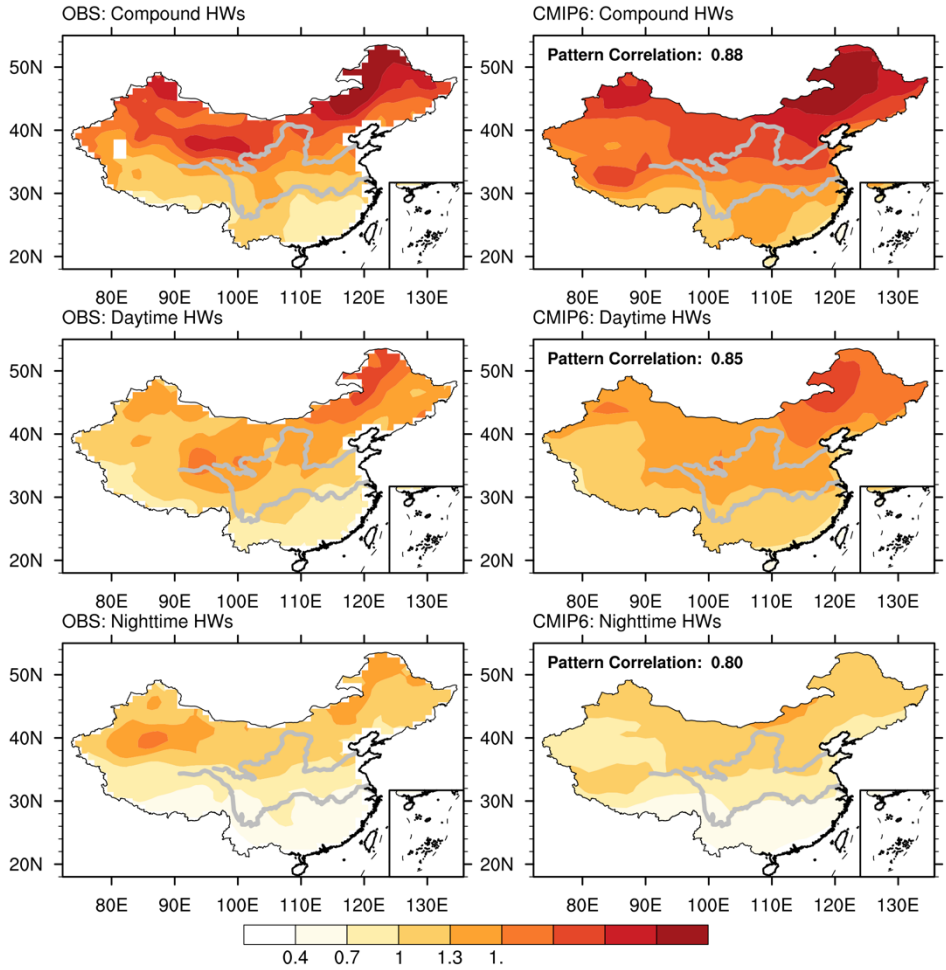

Figure 2.9 Same as Fig. 2.8, but for intensity (units: ℃).

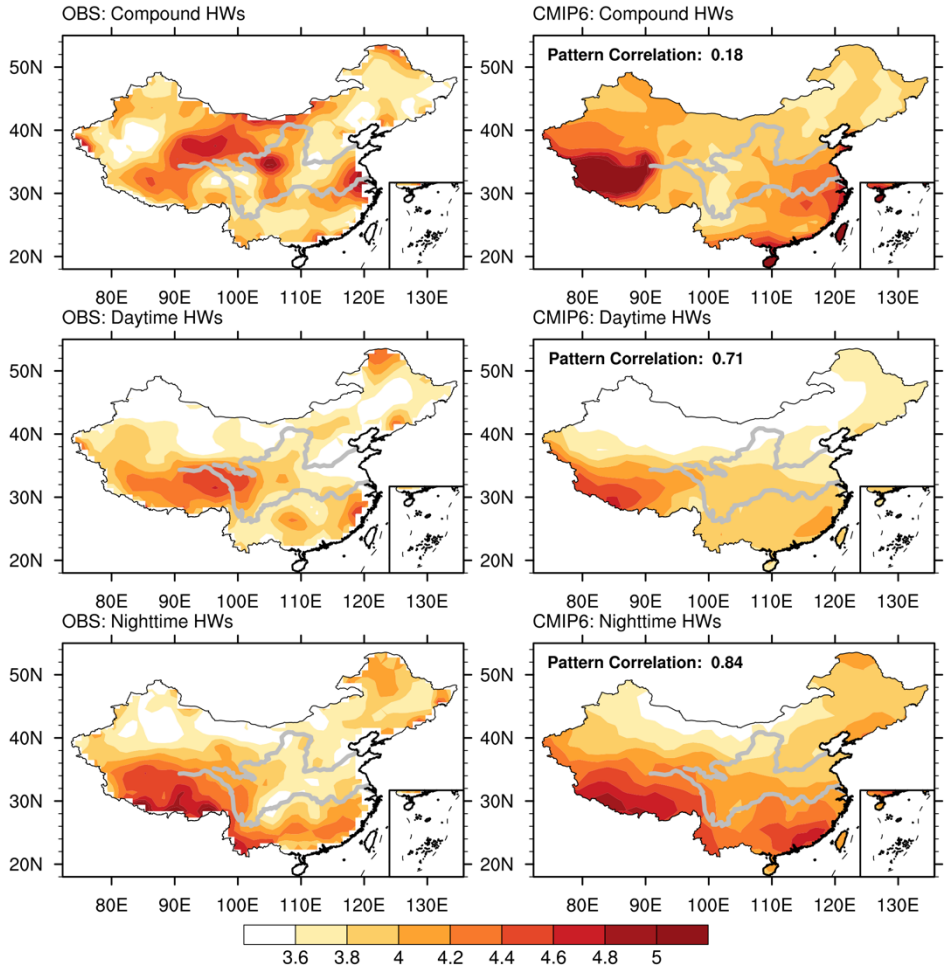

Figure 2.10 Same as Fig. 2.8, but for duration (units: days).

However, the models do have some clear biases. For example, models struggle to successfully simulate climatological spatial distributions of the frequency and duration of Compound HWs and the frequency of Daytime HWs, and with low spatial correlation coefficients are found. The biases mainly appear over the western part of China, which may be related with the relatively large biases in simulating temperature over the western China than the other regions (Fig. 2.11). Meanwhile, the original meteorological station data of the CN05.2 gridded dataset has relatively small number of stations over the western China, especially the western part of the Tibetan Plateau, which may have an influence over this region. Although the biases might affect the simulated HWs over the western China, the analysis show that the multi-model ensemble mean of the 11 models from CMIP6 can still capture the main features of the observed HWs during the historical period.

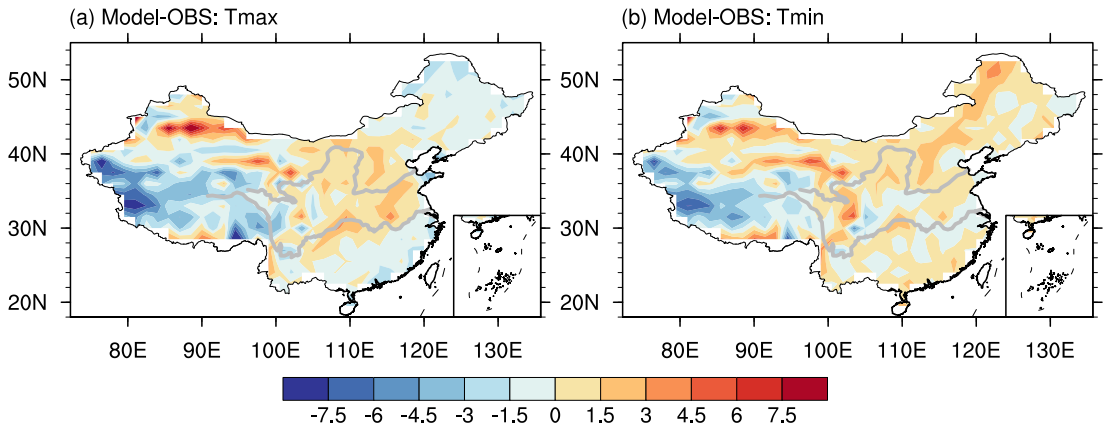

Figure 2.11 The spatial patterns of the differences in the climatology of summer mean Tmax (a) and Tmin (b) during the historical climate (1961-2020) between CMIP6 multimodel mean simulations and observations (units: °C).

2.5 The roles of different forcings on the historical changes of summer heatwaves

The simulated historical changes in HWs over China, shown using the multi-model ensemble mean, is shown in Fig. 2.12-2.14. The regional averaged changes over the entire China and the four subregions are quantified in Fig. 2.15. The figures suggest that the CMIP6 historical simulations capture the main large-scale changes in the frequency, intensity, and duration of all three types of HWs seen in observations. For example, the observed historical changes of Compound HWs and Nighttime HWs show increased frequency, intensity and duration over much of China and the simulated historical changes under external forcing show significant increases over the entire China (Fig. 2.12; Fig. 2.14). For Daytime HWs, the historical changes in frequency, intensity and duration show significant increases over the central China both in observations and under external forcing (Fig. 2.13). Furthermore, examining the regional averages (Fig. 2.15) suggest that the magnitudes of the historical changes under external forcing is similar to the observed ones in most regions except that models overestimate changes in HW duration. Therefore, these results indicate that external forcings have played an important role in the historical changes of HWs over China.

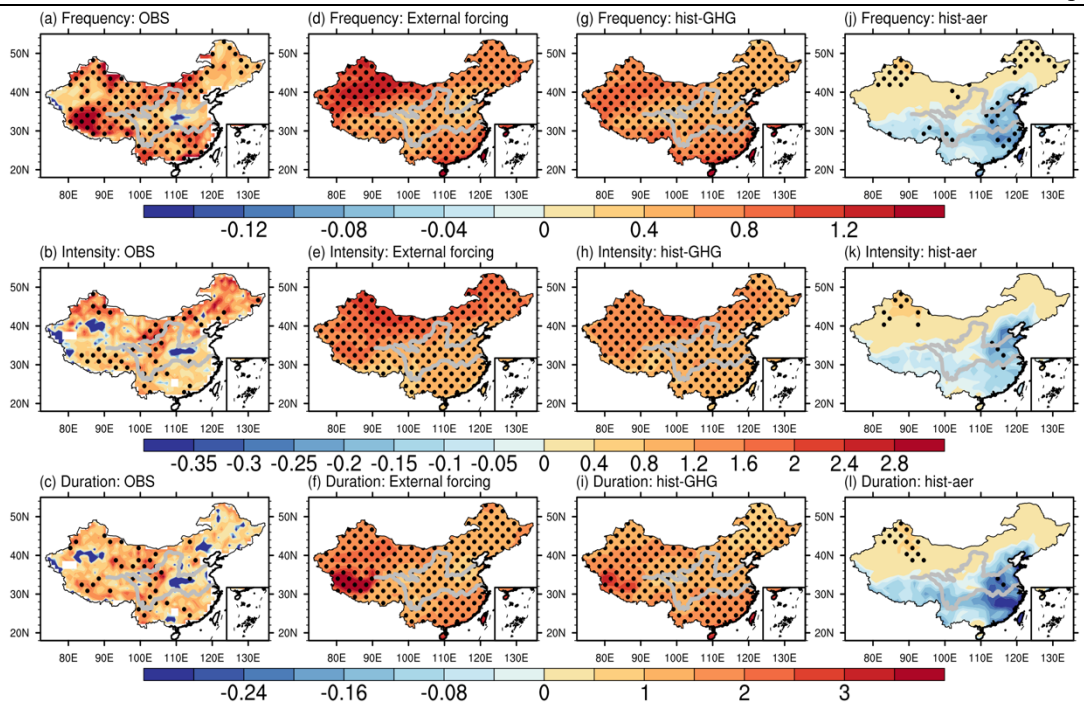

Figure 2.12 The spatial distributions of the historical changes in frequency (units: events·a^{-1}), intensity (units: ℃) and duration (units: days) of Compound HWs between 1995-2020 and 1961-1994 in observations and multimodel mean simulations under different forcings. Shading regions in observation denote the historical changes between the two are significantly different based on the Student's t-test and a significant level of 0.05. Shading regions in simulations denote regions where at least 8 out of the 11 models agree in the sign of changes. Note that contour levels are not equidistant.

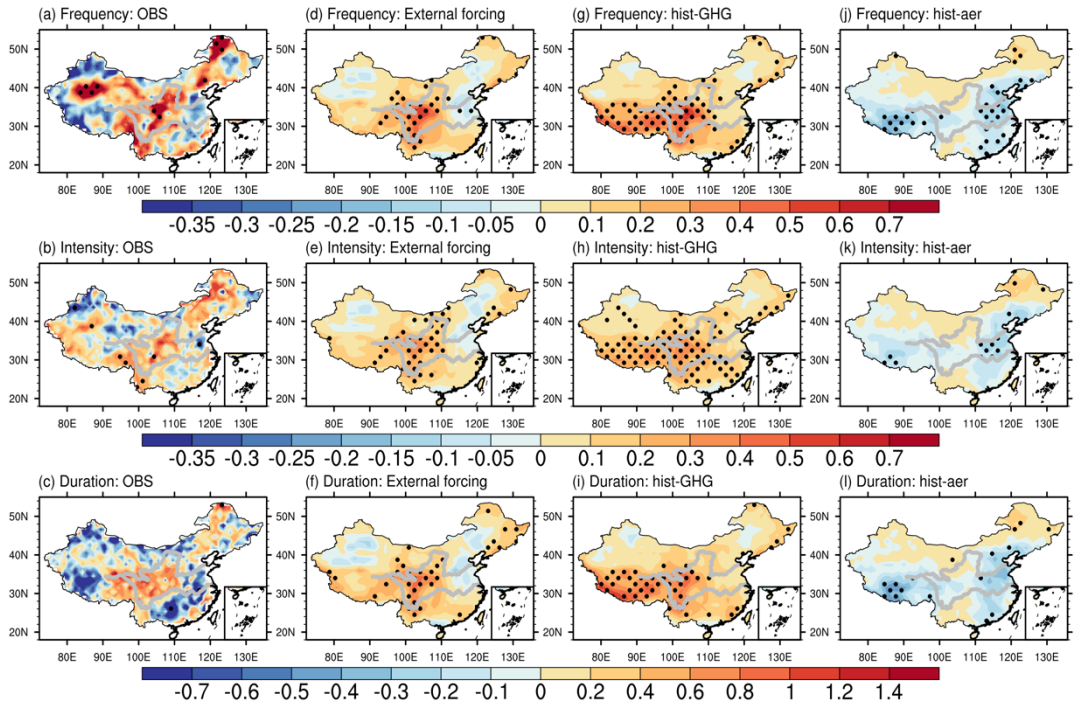

Figure 2.13 Same as Fig. 2.12, but for Daytime HWs.

Fig. 2.12-Fig. 2.14 also shows the roles of greenhouse gas forcing (GHG) and aerosol forcing (AA) on the historical changes of HWs over China. For Compound HWs, GHG plays

a dominant role on the historical increases of HW frequency, intensity and duration over the entire China in CMIP6 historical simulations (Fig. 2.12g-i). In contrast, AA leads to a dipole pattern of changes in frequency, intensity and duration with positive changes over the northern part of China and negative changes over the southern part of China (Fig. 2.12j-l). For Daytime HWs, GHG contributes to the increases of HWs over the Tibetan Plateau and the central China (Fig. 2.13g-i). AA induces a significant decrease in the historical changes over the Tibetan Plateau and North China (Fig. 2.13j-l). Nighttime HWs show significant increases over the entire China in responses to GHG, which explains the increases under external forcing across China (Fig. 2.14g-i). AA plays a negative role over the southern part of China and contributes to the increases over the northern part of China, but with a weaker magnitude (Fig. 2.14j-l).

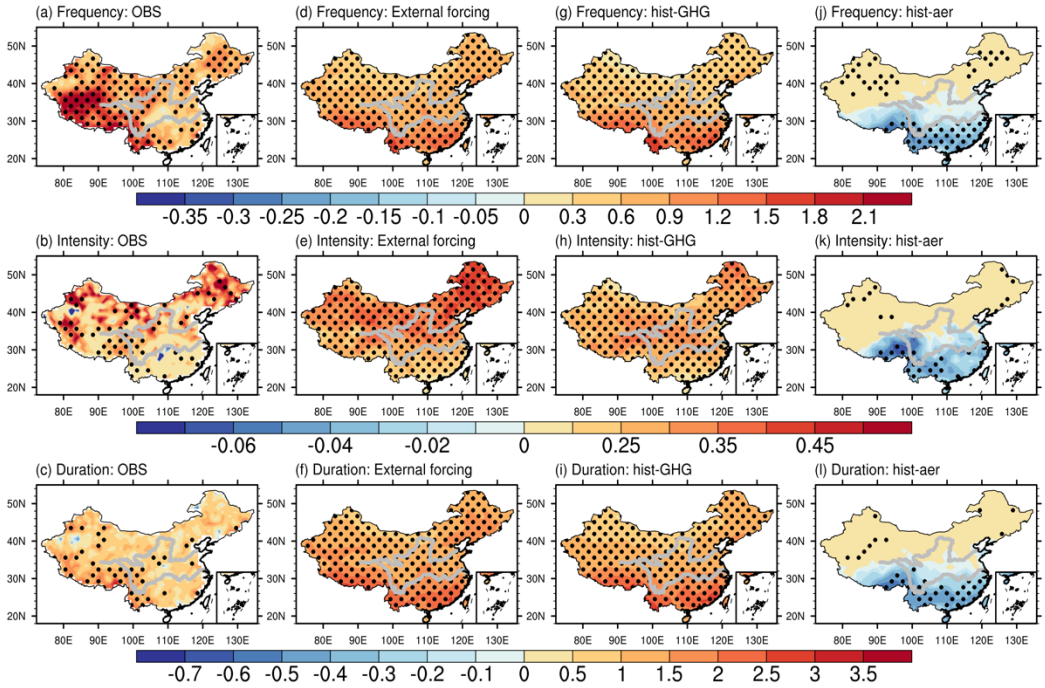

Figure 2.14 Same as Fig. 2.12, but for Nighttime HWs.

Overall, although both GHG and AA contribute to changes in the properties of HWs over China in multi-model ensemble mean simulations, it is changes in GHG that dominates. For example, Figures 2.15 shows that the magnitudes of the historical changes of the three types of HWs under GHG are much larger under just changes in AA. Furthermore, the simulated GHG changes dominates spatial variations of HWs over China, as evidenced by pattern correlation coefficients between the historical changes under external forcing and GHG generally >0.9 (see Table 2.2).

Table 2.2 The spatial pattern correlation coefficients of the historical changes in frequency, intensity and duration of Compound HWs, Daytime HWs and Nighttime HWs between historical all-forcings and greenhouse gas forcing.

	Compound HWs	Daytime HWs	Nighttime HWs
Frequency	0.95	0.87	0.98
Intensity	0.92	0.77	0.95
Duration	0.98	0.88	0.98

Although the external forcing is clearly driving changes in HWs, there are some interesting regional differences found (Fig. 2.15). For Compound HWs, NWC clearly shows the largest historical changes in frequency and intensity under external forcing. However, the increase in HW properties due to GHG only have small differences between the subregions. AA tends to increase the historical changes of Compound HWs over NEC and NWC, while it also tends to decrease the historical changes over SEC and SWC. For Daytime HWs, the largest historical changes under external forcing and GHG forcing appear over SWC. NWC shows the smallest historical changes of the three properties under external forcing and GHG. AA leads to a decrease in historical changes under SWC and SEC, but with a weak magnitude. For Nighttime HWs, the historical changes in frequency and duration over SEC and SWC under external forcing and GHG are larger than the other regions. The magnitudes of the historical changes in intensity under external forcing and GHG are similar over each region. The increases in the three properties over NEC and NWC and decreases over SEC and SWC due to AA forcing are consistent with the dipole pattern shown in Fig. 2.14.

In summary, the above results demonstrate that the historical changes of all three types of observed HWs are predominantly explained by the changes in external forcing. In terms of the relative roles of different anthropogenic external forcings, GHG changes play a dominant role in the historical increases of HWs, but AA is important for shaping the regional response. In particular, AA changes make positive contributions on the historical changes over the northern part of China and negative contributions over the southern part of China, but the magnitude is weak.

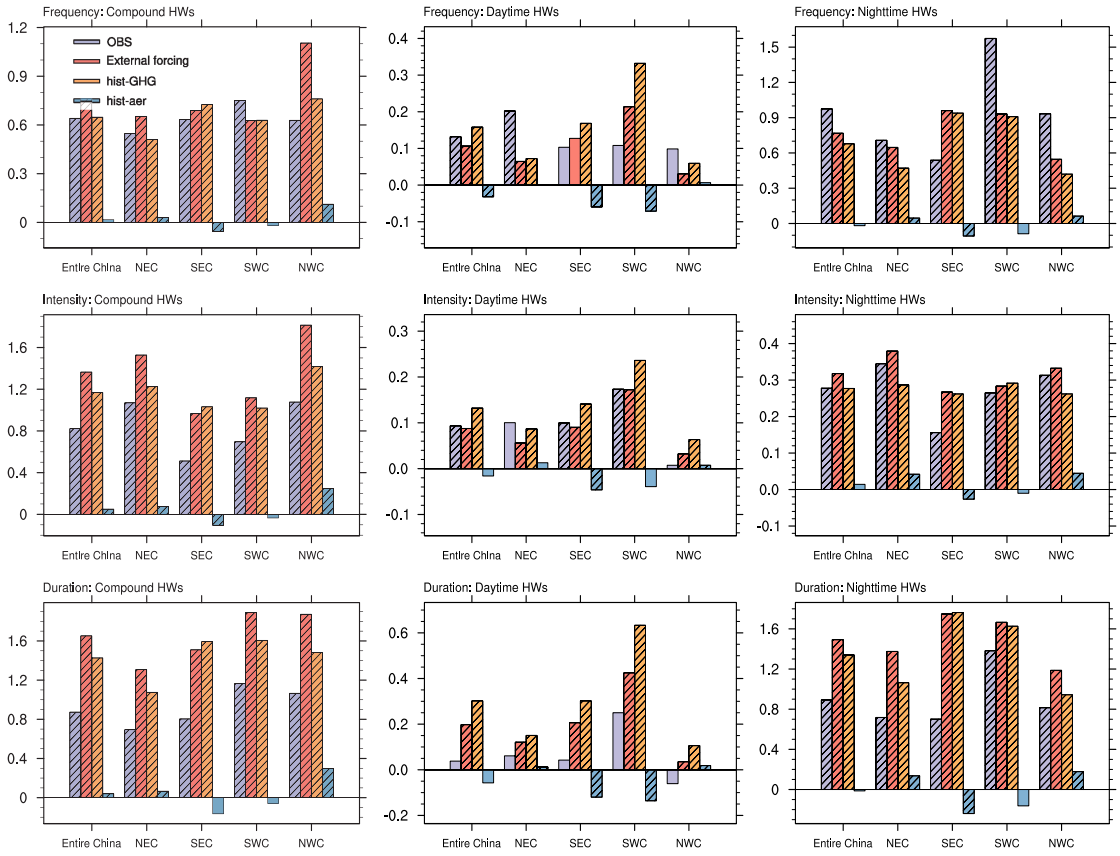

Figure 2.15 The area-averaged historical changes in frequency (top row, units: events·a^{-1}), intensity (middle row, units: ℃) and duration (bottom row, units: days) of Compound HWs (left column), Daytime HWs (middle column) and Nighttime HWs (right column) between the period 1995-2020 and 1961-1994 based on observations and multimodel mean simulations under different forcings. The shaded marks on bars represent the historical changes between the two periods have passed the t-test at the significant level of 0.05. Shading marks in simulations denote the changes where at least 8 out of the 11 models agree in the sign of changes.

2.6 The physical processes responsible for the historical changes of heatwaves under different forcings

Given that external forcings lead to large simulated changes in HWs, we now turn our attention to understanding the important physical processes. Previous work has shown that the changes in the properties of HWs can be explained by changes in seasonal-mean temperatures and temperature variability (Argueso et al., 2016; Su and Dong, 2019a).

Fig. 2.16 shows the probability density functions (PDFs) of the simulated regional-mean daily Tmax and Tmin in summer during the two time periods in CMIP6 historical ensemble simulations. In each region, the PDFs of daily temperature for 1995-2020 are shifted to the right relative to those for 1961-1994. After removing the corresponding local

time mean Tmax and Tmin at each time period, the distributions of daily temperature anomalies during the two periods are very similar, indicating that the daily Tmax and Tmin over these two periods has similar temperature variability.

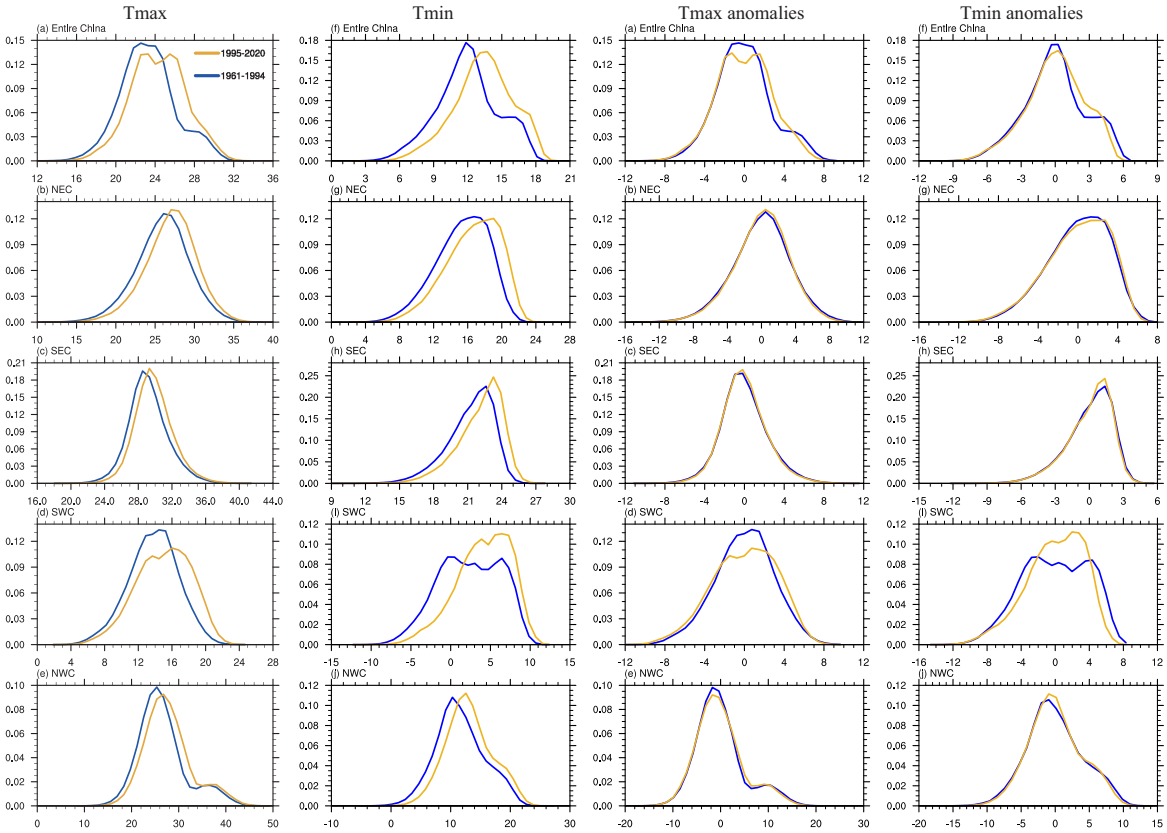

Figure 2.16 The Kernel probability density functions of daily Tmax (a-e), daily Tmin (f-j), daily Tmax anomalies (k-o) and daily Tmin anomalies (p-t) in summer relative to corresponding mean Tmax and Tmin in each period averaged over the entire China and the four subregions based on CMIP6 multimodel ensemble historical simulations.

To further assess and quantify the relative roles of seasonal mean temperature changes and temperature variability changes on the historical changes of HWs, two reconstructed temperature time series for 1961-1994 are made by adding the summer mean Tmax and Tmin differences between two periods (1995-2020 minus 1961-1994) to the original daily Tmax and Tmin time series of 1961-1994, respectively. In this way, the differences in HWs between the reconstructed series of 1961-1994 and original series of 1961-1994 are only due to the seasonal mean warming signal (blue bars in Fig. 2.17). Meanwhile, the differences in HWs between the original series of 1995-2020 and the reconstructed time series of 1961-1994 are only due to temperature variability (green bars in Fig. 2.17).

Fig. 2.17 illustrates the contributions of mean seasonal warming and temperature variability to the historical changes of HWs over different regions using the reconstructed timeseries. It can be seen that the seasonal mean warming plays the dominant role on the historical changes of HWs. The magnitudes of the historical changes due to seasonal mean warming are very close to the original historical changes. In contrast, the role of changes in temperature variability is small. Therefore, given the dominant role of seasonal mean changes in driving the historical changes of HWs, to better understand the physical processes shaping the changes in HWs, it is reasonable to analyze the changes of physical variables in climatological seasonal mean state between the two time periods.

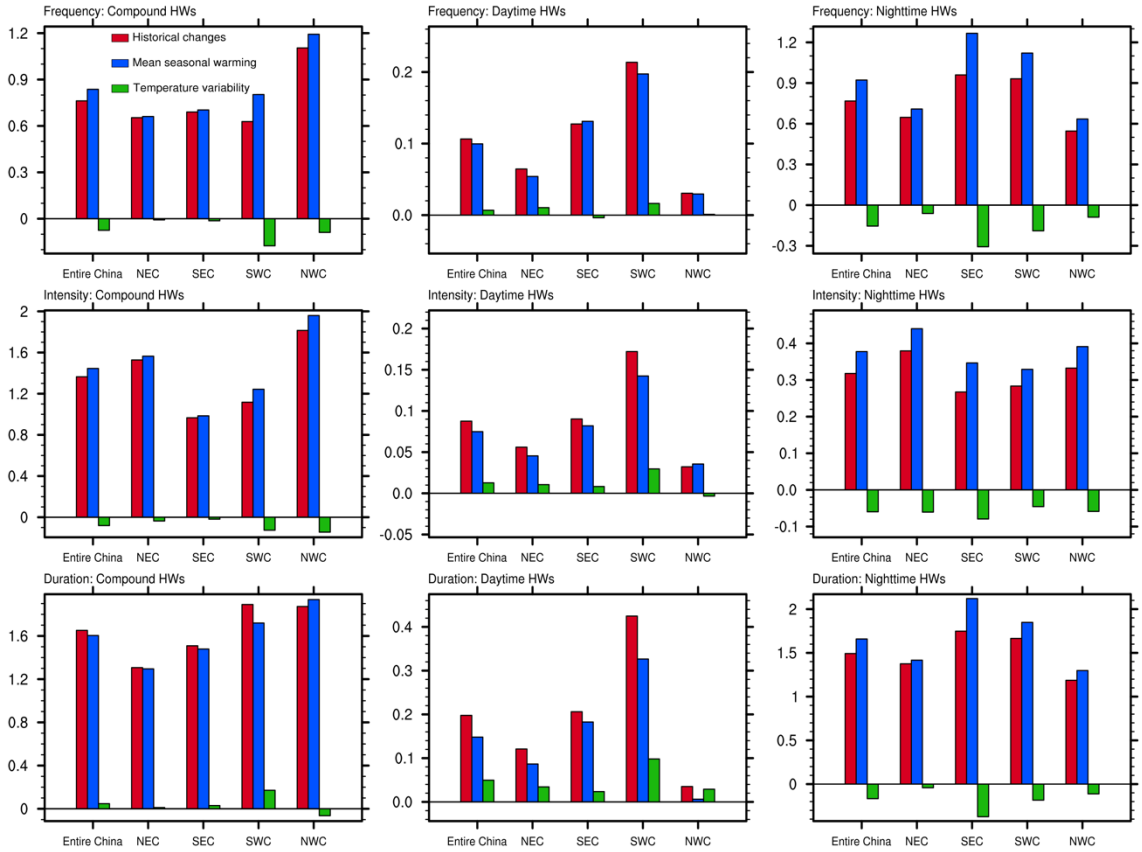

Figure 2.17 The simulated area-averaged historical changes (red bars), historical changes due to mean seasonal warming (blue bars) and historical changes due to temperature variability (green bars) in frequency (top row, units: events·a^{-1}), intensity (middle row, units: °C) and duration (bottom row, units: days) of Compound HWs (left column), Daytime HWs (middle column) and Nighttime HWs (right column) between the period 1995-2020 and 1961-1994 based on CMIP6 multi-model ensemble historical simulations.

Figure 2.18 shows the multi-model mean historical changes of some key physical variables between two periods of 1995-2020 and 1961-1994 in the hist-GHG simulations. The summer mean Tmax and Tmin increase significantly across China (Fig. 2.18e, f), which

contributes to the historical increases of Compound HWs and Nighttime HWs under GHG. The increases of surface air temperature are mostly associated with the significant increases of the surface clear-sky downward longwave radiation across China (Fig. 2.18b), which partly results from the increases of greenhouse gas concentrations and the GHG-forcing induced increase of water vapor in the atmosphere (Fig. 2.18a). The historical increases of the surface longwave radiation over the northern part of China are larger than the southern part of China, which is consistent with the larger changes in intensity of Compound HWs and Nighttime HWs over the NEC under GHG (Fig. 2.15). Influenced by the decreases of total could cover (Fig. 2.18c), the net surface shortwave radiation increases significantly over the central China and the Tibetan Plateau (Fig. 2.18d), leading to the warmer Tmax over these regions (Fig. 2.18e), which is consistent with the significant increases of Daytime HWs under GHG (Fig. 2.13).

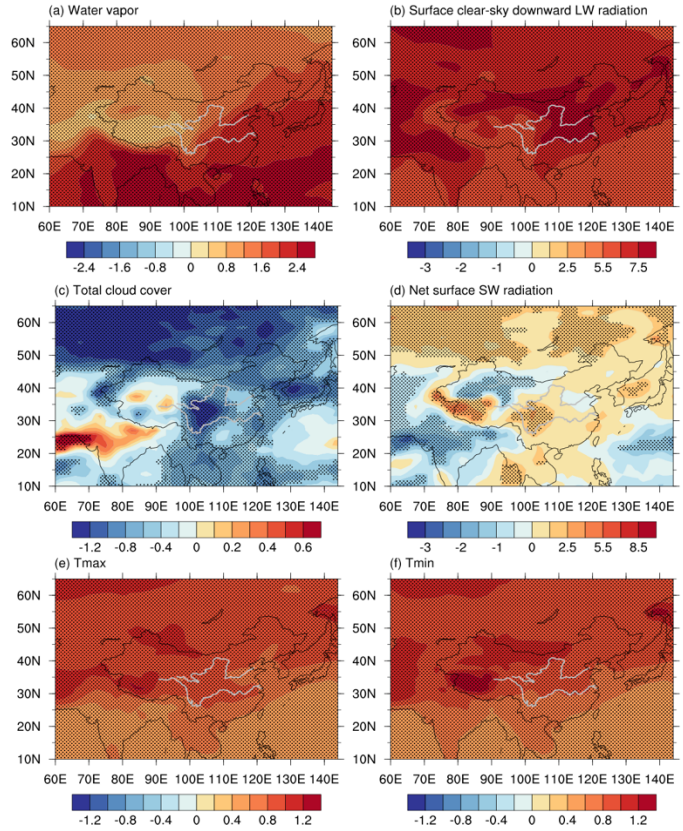

Figure 2.18 The spatial distributions of the multi-model mean historical changes of vertically integrated water vapor through the atmospheric column (a, units: kg·m^{-2}), surface clear-sky downward longwave radiation (b, units: W·m^{-2}), total cloud cover (c, units: %), net surface shortwave radiation (d, units: W·m^{-2}), daily maximum temperature (e, units: ℃) and daily minimum temperature (f, units: ℃) between the period 1995-2020 and 1961-1994 in summer (June, July, August) based on hist-GHG simulations. Shading regions denote regions where at least 8 out of the 11 models agree in the sign of changes.

In response to AA changes, the spatial distributions of the multi-model mean historical changes in some key variables between two periods of 1995-2020 and 1961-1994 are shown in Fig. 2.19. Over this period, anthropogenic aerosol emissions decreased over North America and Europe, and increased over East Asia and South Asia (Dong et al., 2022). The large-scale aerosol changes may have influenced the meridional temperature gradients, which could contribute to modifications in the thermal contrast between land and ocean and then influence the strength and position of East Asian summer monsoon (Wang et al., 2017). Associated with these contrasting changes in anthropogenic aerosol emissions are increased AOD at 550nm (Fig. 2,19c) and increased cloud cover (Fig. 2.19a) over large part of China through aerosol-radiation and aerosol cloud interactions (Hatzianastassiou et al., 2007, Boucher et al., 2013). The increases of AOD result in the decrease of net surface clear-sky shortwave radiation (Fig. 2.19d), which is partially offset by increased total cloud cover (Fig. 2.19a), leading to the significant decrease in net surface shortwave radiation over Southwest China and eastern China (Fig. 2.19b). The dipole pattern of the changes in water vapor under AA contributes to the increases of surface clear-sky downward longwave radiation over the northern part of China and the decreases over the southern part of China (Fig. 2.19e, f). These changes in surface radiations lead to cooling over the southern part of China (Fig. 2.19g, h). The influence of shortwave radiation on the historical changes of HWs is larger than the one of longwave radiation due to the larger magnitudes of historical changes in shortwave radiation. The warming in mid-latitudes and northern part of China may be related to decreases of aerosol emissions over Europe and aerosol change induced atmosphere and surface feedbacks (Sun et al., 2022; Gao et al., 2023). The Tmax changes with a weak warming in northern China and cooling in southern China explains the larger historical decreases in Compound HWs and Daytime HWs over North China and the southern part of China and weak increases over northern China under AA. The dipole pattern of Tmin changes is consistent with the historical changes of Nighttime HWs under AA shown in Fig. 2.14.

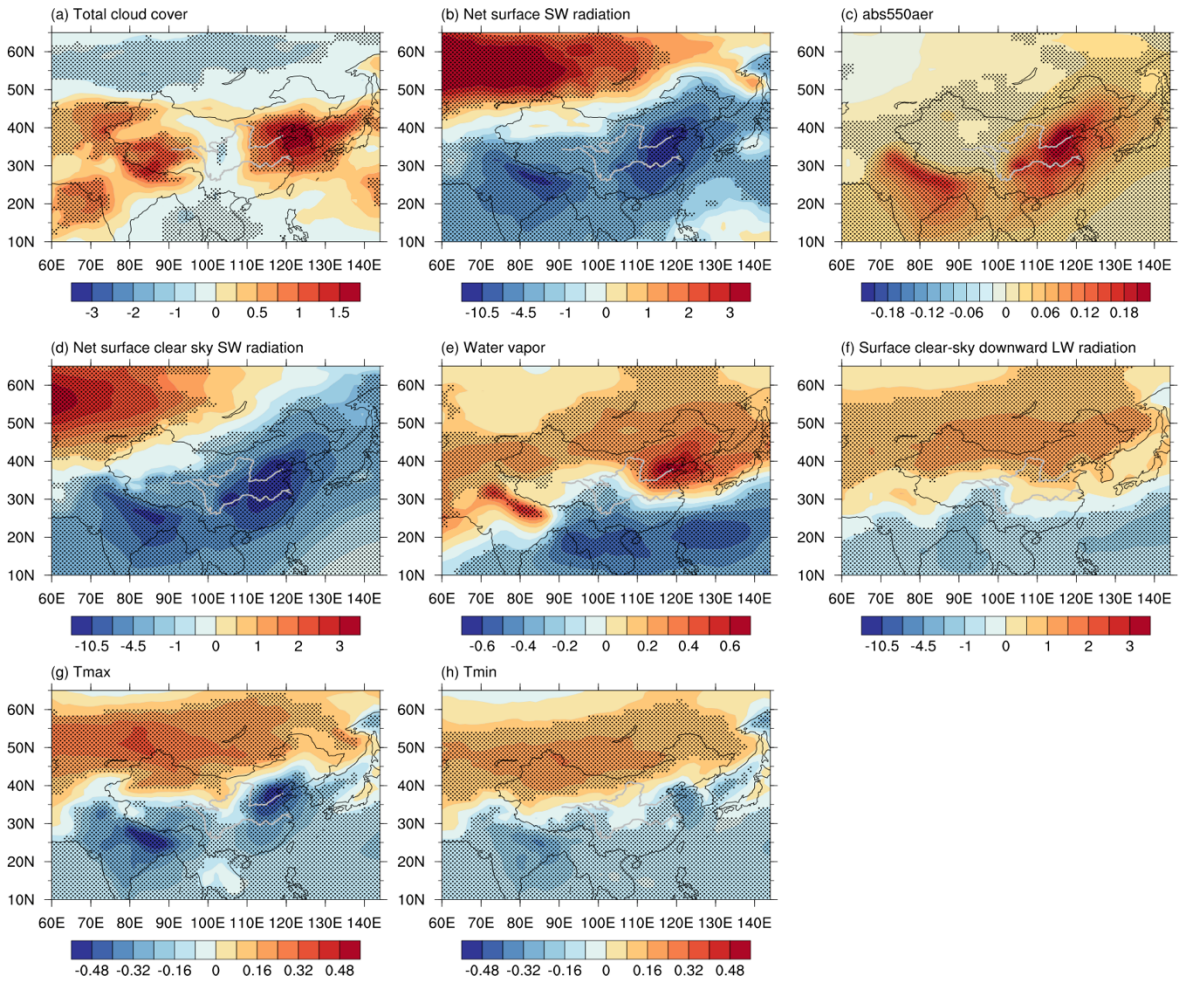

Figure 2.19 The spatial distributions of the multi-model mean historical changes in total cloud cover (a, units: %), net surface shortwave radiation (b, units: W·m^{-2}), AOD at 550nm (c, units: 10^{-3}), net clear-sky surface shortwave radiation (d, units: W·m^{-2}), vertically integrated water vapor through the atmospheric column (e, units: kg·m^{-2}), surface clear-sky downward longwave radiation (f, units: W·m^{-2}), daily maximum temperature (g, units: ℃) and daily minimum temperature (h, units: ℃) in summer between the period 1995-2020 and 1961-1994 based on hist-AER simulations. Shading regions denote regions where at least 8 out of the 11 models agree in the sign of changes.

2.7 Conclusions

In the recent decades, warm extreme events are becoming more frequent and severe over China. This chapter discusses the observed historical changes in frequency, intensity and duration of summer Compound Heat Waves (HWs), Daytime HWs and Nighttime HWs between the period 1995-2020 and 1961-1994. By using the multi-model ensemble mean of 11 CMIP6 models, the role of external forcing on the historical changes of HWs is assessed and the relative roles of greenhouse gas forcing (GHG) and aerosol forcing (AA) on the

historical changes of HWs and associated physical processes are also evaluated. The main results are summarized as follows.

During the 1961-2020, the three types of HWs show positive trends with an abrupt increase around the mid-1990s over China. The increasing rates of the frequency, intensity and duration of Compound HWs and Nighttime HWs are much larger than the ones of Daytime HWs. The insignificant increase in the frequency of Daytime HWs averaged over the entire China is caused by a decrease of low-intensity Daytime HWs.

By comparing the historical changes between the period 1995-2020 and 1961-1994, Compound HWs and Nighttime HWs become more frequent with events becoming hotter and durations becoming longer across China. The magnitudes of the historical changes of the three types of HWs show regional differences. For example, the historical changes in frequency and duration of Compound HWs and Nighttime HWs over SWC are larger than the other regions. The largest historical changes in frequency of Daytime HWs appear over NEC.

The historical changes of HWs over China are consistent with changes in external forcing, which is predominantly resulted from GHG changes. The significant increases in simulated Compound HWs and Nighttime HWs over the entire China and the significant increases in Daytime HWs over central China are mainly due to GHG changes. AA changes make significant positive contributions on the historical changes over NWC and NEC and tend to play a negative role on the historical changes over the southern part of China and North China.

The historical changes of the three types of HWs are mainly explained by the changes of seasonal mean warming. In terms of the physical processes due to GHG changes, the increases of greenhouse gas concentrations and subsequent increases of water vapor in the atmosphere lead to the increases of surface longwave radiation. The changes in longwave results in the warming across China, which is responsible for the increases of Compound HWs and Nighttime HWs properties. The increases of net surface shortwave radiation influenced by a decrease of total cloud cover contribute to the surface warming, which is associated with the significant increases of Daytime HWs over central China.

In response to AA changes, the historical changes of Tmax and Tmin are mostly related with the historical changes of HWs properties. The decreases of surface shortwave radiation related with the increases of aerosol and total cloud cover tend to cool the surface and then contribute to the decreases of Compound HWs and Daytime HWs over North China and the southern part of China. The dipole pattern of surface clear-sky longwave radiation is associated with a similar pattern of the historical changes in Tmin, which is responsible for the increases of Nighttime HWs over the northern part of China and decreases over the southern part of China.

Our results give a view of the historical changes of HWs over China and show the dominating role of GHG on the historical changes of HWs. Although this chapter explores the role of external forcing and the relative role of GHG and AA on the historical changes of the three types of HWs over China. However, natural climate variability could also influence the decadal warming over Asia around the mid-1990s, such as the Atlantic multidecadal variability and the Interdecadal Pacific Oscillation (Kwon et al., 2007; Hong et al., 2017; Zhang et al., 2024b). Further study is still needed to give a more comprehensive understanding of the contributions of these factors on the historical changes of the three types of HWs over China.

Chapter 3

The future projections of summer Compound heatwaves over China

Heatwaves (HWs) are weather events characterized by extreme hot surface air temperature anomalies that persist for several days, and thus leading to devastating impacts on society. There are three types of HWs and they are daytime HWs occurred only on daytime, nighttime HWs occurred only on nighttime and the Compound HWs occurred on both daytime and nighttime. In contrast with the influence of HWs which only occur on daytime or nighttime, the Compound HWs combining with disastrous effects from both daytime HWs and nighttime HWs have more severe impacts on human and society. Previous studies suggested that the Compound HWs will be the most frequent type that populations are exposed to after 2030 in the Northern Hemisphere. However, a limited number of studies have discussed the future changes of Compound HWs over China and they are mainly based on a fixed future time period. Considering the increasing importance of the future projections at the target global warming levels (GWLs), focusing on **the first part of the third scientific question**:

iii) How will summer Compound HWs over China change in the future at different global warming levels?

This chapter aims to assess the changes in frequency, intensity and duration of Compound HWs in summer over China at various GWLs under SSP3-7.0 and SSP5-8.5 based on the multi-model ensemble mean of CMIP6 simulations.

This chapter has been published in *Climate Dynamics* (Zhang et al. 2024c):

Zhang, M., Dong, B., Schiemann, R., Robson, J.,Summer compound heatwaves over China: projected changes at different global warming levels and related physical processes. *Clim Dyn* (2024c). https://doi.org/10.1007/s00382-023-07001-4

Abstract

Based on the multi-model ensemble mean of CMIP6 simulations, the future changes in frequency, intensity and duration of Compound (both daytime and nighttime) heatwaves (HWs) in summer over China at various global warming levels (GWLs) under the SSP3-7.0 and SSP5-8.5 are assessed. HWs over China become more frequent and hotter, and the duration of HWs becomes longer compared to those in the recent climate. The magnitudes of these changes are primarily dependent on GWLs, but they are not very sensitive to the scenarios. At 4°C GWL, the frequency of HWs increases by more than five-fold under both scenarios, and the intensity (duration) of HWs averaged under the two scenarios is 2.28°C hotter (3.59 days longer) than the one in the recent climate over the entire China. Meanwhile, the maximum duration of HW events can reach more than 25 days in summer in comparison with 8 days in the recent climate. The changes in HW properties are regionally dependent at the four GWLs. For example, the largest increase in HW frequency is over the Northwest China, the largest increase in intensity in HWs is seen over the Northeast and Northwest, and the largest increase in HW duration is over the Southwest China. The extreme rare events (50-year and 100-year events) in the recent climate would become the norm over China and four sub-regions at 4°C GWL. Overall, seasonal mean warming dominates the changes in HW properties over China at the different GWLs. The seasonal mean warming in summer across China is related to the increases of longwave radiation, partly due to increase in greenhouse gas forcing and partly resulted from increased water vapor and the increase of shortwave radiation (under the SSP5-8.5) over eastern China related to decreases in aerosols and total cloud cover. Furthermore, the regional variations in the water vapor over China are consistent with atmospheric circulation changes. The seasonal mean surface warming results in enhanced upward sensible and latent heat fluxes, leading to increased summer mean daily maximum and minimum of near-surface air temperature and the enhancement of HWs properties over the entire China. Changes of shortwave radiation tend to play a weaker role for surface warming under the SSP3-7.0 than those under the SSP5-8.5, which is related to increased aerosol changes under the SSP3-7.0.

3.1 Introduction

Heatwaves (HWs) are weather events characterized by extreme hot surface air temperature anomalies that persist for several days (Sun et al., 2014), which can lead to severe damage to society (e.g., Bras et al., 2021; Alizadeh et al., 2022). As the global mean surface temperature (GMST) increases under different future forcing scenarios, it is expected that there will be an increase of HWs over China (Zhou et al., 2014; Hu and Sun, 2020; Chen and Dong, 2021). In contrast with the influence of HWs which only occur on daytime or nighttime, Compound HWs combine with disastrous effects from both Daytime HWs and Nighttime HWs (An and Zuo, 2021). Wang et al. (2020) have figured out that the compound type will be the most frequent one that populations are exposed to after 2030 in the Northern Hemisphere. Hence, it is also worthwhile to focus on the future changes of Compound HWs over China. However, a very limited number of studies have discussed it and they mainly focused on future projections of Compound HWs during some fixed future time periods (Su and Dong, 2019b; Xie et al., 2022).

In the recent years, due to the goal set in the Paris Agreement (UNFCCC, 2015), future projections based on target global warming levels (GWLs) are becoming more frequent to be discussed. By the end of the 21st century, the likely range of GMST increase is 2.0-4.9°C with a median of 3.2°C (Raftery et al., 2017). However, the temperature related impacts of higher warming scenarios (e.g., of 3°C and above) are less emphasized in the IPCC AR6 (Jehn et al., 2021; 2022). Hence, it is necessary to focus on the future changes at the target GWLs of 1.5°C, 2°C, 3°C and 4°C to assist the government in making policy decisions and mitigating the risks associated with these hot extremes.

The Coupled Model Intercomparison Project Phase 6 (CMIP6) models provide the most up-to-date simulations of future climate and show a general improvement in simulating extreme climate in China compared with previous phases (Chen et al., 2020). Therefore, to better understand the future changes in Compound HWs over China under different GWLs, this chapter aims to quantify the magnitude of changes in Compound HWs and identify the related physical processes based on CMIP6 multi-model ensembles. The chapter is organized as follows: Section 3.2 describes the data and methods used in this chapter.

Section 3.3 shows the changes of Compound HWs at the 1.5°C, 2°C, 3°C and 4°C GWLs. The physical processes related to the changes of HW properties are elucidated in Section 3.4. The conclusions and discussions are summarized in Section 3.5.

3.2 Data and methods

3.2.1 Data

This chapter uses the historical simulations and future projections from CMIP6 (Eyring et al., 2016). The historical simulations cover the past period 1850-2014. The future projections cover the period 2015-2100 with different scenarios of external forcings. Here, we use two scenarios. The first is the SSP3-7.0, which has a medium to high radiative forcing of 7.0 $W \cdot m^{-2}$ by 2100. The SSP3-7.0 has a particularly high aerosol emissions and it fills a gap between the RCP6.0 and RCP8.5 in CMIP5 forcing pathways (IPCC, 2022). The second scenario used is the SSP5-8.5 which represents the highest forcing pathway with a radiative forcing of 8.5 $W \cdot m^{-2}$ in 2100 (O'Neill et al., 2016). The models and ensemble numbers used are listed in Table 3.1. These models can well represent the historical temperature distributions over China (Yang et al., 2021; You et al., 2021).

Table 3. 1 The list of models used in this study

	Model	Resolution (lon x lat)	Members
1	BCC-CSM2-MR	320x160	1
2	FGOALS-g3	180x80	1
3	CNRM-CM6-1	256x128	1
4	ACCESS-ESM1-5	192x144	3
5	ACCESS-CM2	192x144	3
6	MIROC6	256x128	3
7	IPSL-CM6A-LR	144x143	1
8	MRI-ESM2-0	320x160	5
9	NorESM2-LM	144x96	1

The model outputs of daily minimum temperature (Tmin), maximum temperature (Tmax), daily mean temperature, as well as monthly radiation and atmospheric circulation variables are analyzed in the following sections. In order to calculate the multi-model ensemble mean, the bilinear interpolation method is used to regrid the model outputs to a common 1.5° × 1.5° grid to facilitate the intercomparison. The ensemble members of historical simulations and future projections in each model are the same. The HWs properties of each ensemble member are calculated individually. To treat each model equally, the multi-member mean is calculated in each model first and then the multi-model ensemble mean is derived by all models.

Based on the topography and regional climate over China (Song et al., 2011), we focus on the changes over the entire China and its four subregions (Fig. 3.1), which are Northeast and North China (NEC; 35°-54°N, 105°-134.5°E), Southeast China (SEC; 21°-35°N, 105°-123°E), Southwest China (SWC; 21°-37°N, 73°-105°E) and Northwest China (NWC; 37°-50°N, 73°-105°E). This chapter focuses on the changes during summer (June-August).

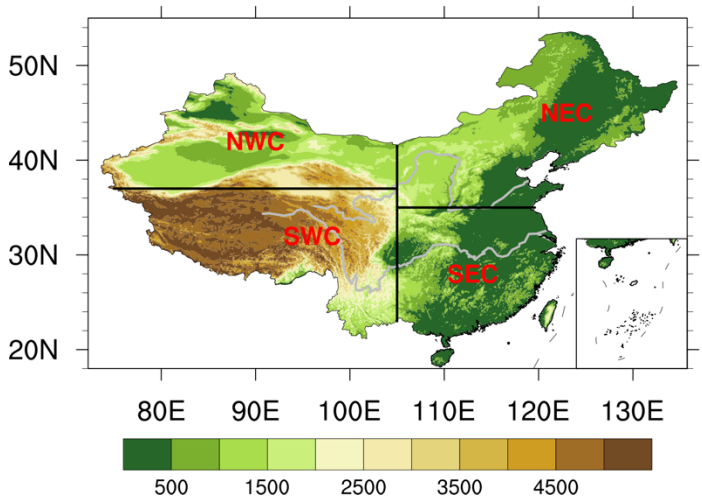

Figure 3.1 The topography (units: m) over the study regions. The subregions analyzed in the study are distinguished by black lines and they are Southeast China (SEC), Northeast and North China (NEC), Northwest China (NWC) and Southwest China (SWC).

3.2.2 Methods

a. Definition of HWs

In order to define Compound HWs, a relative threshold on each calendar day is calculated as the daily 90th percentile of Tmax or Tmin based on 15-day window centered on that day during the baseline period of 1961–1990 (Della-Marta et al., 2007). Compound

HWs are identified when the daily Tmax and Tmin exceed the baseline 90th percentile for at least three consecutive days.

Three features, that is frequency, intensity and duration, are used to characterize Compound HWs. The frequency is the accumulated number of Compound HW events within a year. The intensity of each event is calculated by the sum of the averaged the daily Tmax and Tmin temperature anomalies above the corresponding thresholds within the event. The duration is the number of days from the beginning to the end of an event. The intensity and duration of events for a year are computed by averaging the intensity and duration of events occurring in that year. In addition, the max-duration event, which is used to present extreme long-lasting Compound HWs in a given year, is also analyzed.

b. Time windows of the 1.5°C, 2°C, 3°C and 4°C global warming levels

According to the IPCC AR6 report (Lee et al., 2021), 1850-1900 and 1995-2014 are defined as the pre-industrial period and the recent climate period, respectively. The global warming levels refer to the GMST under the two scenarios which is 1.5°C, 2°C, 3°C and 4°C higher than the GMST during the pre-industrial period. To reduce the uncertainty in calculating the warming threshold-crossing times due to interannual variability, a 20-year running average is used to smooth the GMST time series (Liu et al., 2020). A 20-year window, which has 10 years before and 9 years after the year that exceeds the four global warming thresholds, is used to obtain relatively stabilized future climate states at different GWLs. Each member in CMIP6 model owns its individual time window of each GWLs. Figure 3.2 shows the GMST anomalies relative to the pre-industrial period. All members can reach 3°C GWL under the two scenarios. All members under the SSP5-8.5 can reach the 4°C GWL by the end of the 21st century, but only 14 members (6 models) can reach this target under the SSP3-7.0. The differences in HWs between various GWLs and the recent climate are regarded as the future changes in HWs (Domeisen et al., 2023). Consistency among models is checked by at least 7 out of 9 models agreeing on the sign of multi-model ensemble mean changes.

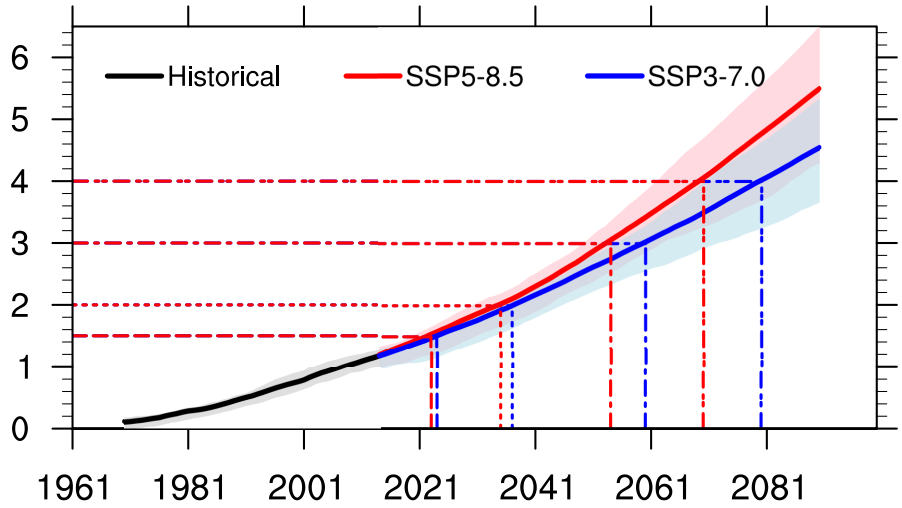

Figure 3.2 Time series of 20-year moving global mean surface temperature anomalies (relative to 1850-1900 pre-industrial period) from CMIP6 models. Black line is historical simulations and blue (red) line represent SSP3-7.0 (SSP5-8.5) scenario. Solid lines indicate the multi-model ensemble mean, and shading the interquartile ranges. Vertical dashed lines indicate the calendar year for the ensemble mean to reach 1.5°C, 2°C, 3°C and 4°C GWLs.

c. Probability ratios of Compound HWs

The probability ratio (PR) is defined as the ratio of the probability of Compound HWs at different GWLs to the probability in the recent climate (Sun et al., 2018) and this ratio quantifies the changing probability of an event in future relative to present climate. The extreme Compound HWs are events with a 50-year or 100-year return periods in the recent climate. The thresholds of these two relatively rare extreme events are obtained by Gumbel extreme value distribution function which is helpful to identify the temporal distribution of meteorological extreme values with various return periods (Gumbel, 1942; Zhou et al., 2009; Yao et al., 2018). Therefore, PR for these extreme rare events is calculated by P_1/P_0, in which P_1 is the probability of 50-year (100-year) events at different GWLs and P_0 is 2% (1%) for 50-year (100-year) events in the recent climate.

3.3 Projected changes of Compound HWs properties

3.3.1 The changes of Compound HWs at different global warming levels

The models chosen for this study represent some main characteristics and spatial variations of Compound HWs in terms of frequency, intensity and duration during the historical period (Fig. 3.15). The multi-model ensemble mean captures the locations of high value centers of the three properties across China, especially over the eastern part of China.

The pattern correlation coefficient of intensity between model simulations and observations can reach 0.90. However, the correlation coefficient of frequency and duration is only about 0.21 and 0.06, respectively. These low correlations suggest that model have some biases in simulating climatological spatial distributions of frequency and duration. To show if model can capture observed changes during the historical period, the linear trends of Compound HW properties during the period 1961-2020 in observations and model simulations over various regions are analyzed and results are given in Fig. 3.16. Although there are biases over the western China with HW properties underestimated by 20-25% in model simulations, the model can well reproduce the observed trends over the other regions. Furthermore, the multi-model mean of CMIP6 can well represent the historical temperature distributions over China with pattern correlation coefficients over 0.95 (Fig. 3.17). The differences between model simulations and observations show relatively large biases over the western China than the other regions, with cold biases being associated with underestimated trends of HW properties. Although the biases might affect the model simulated HWs over the western China, the models can capture the main features of observed trends of HWs during the historical period, giving the fidelity using such models to assess future changes.

The spatial patterns of frequency, intensity and duration of the Compound HWs in the recent climate and at different GWLs are shown in Fig. 3.3 and the future changes in these properties are given in Fig. 3.4, respectively. The largest frequency of Compound HWs appears over Northwest China with a value of 1.76 events per year (hereafter as events·a^{-1}) in the recent climate. With the increasing of GMST, the largest frequency of Compound HWs is much larger, with a value of 3.57 (4.37; 6.13; 7.11) events·a^{-1} at the 1.5°C (2°C; 3°C; 4°C) GWL. In terms of future changes, the frequency of Compound HWs increases significantly over the entire China, especially over Northwest China and Southeast China with a maximum increase of 1.71 (2.74; 4.45; 5.81) events·a^{-1} at the 1.5°C (2°C; 3°C; 4°C) GWL (Fig. 3.4a-h).

The magnitude of intensity of Compound HWs increases from south to north with a range of 1.17-6.50°C in the recent climate. However, the intensity increases with increasing GWL. Specifically, the range of Compound HWs intensity is 1.50-6.36 (1.79-6.61; 2.66-

7.17; 3.61-8.31) °C over China at the 1.5°C (2°C; 3°C; 4°C) GWL. The largest future changes of intensity occur over the Northwest China, with an increase by 0.72 (1.06; 2.11; 3.46) ℃ at the 1.5℃ (2℃; 3℃; 4℃) GWL (Fig. 3.4i-p). Particularly, the enhancements of intensity among models become more consistent over the entire China above the GWL of 3℃.

For duration, the Compound HWs last longer over western China and Southeast China with a maximum duration of 5.87 days in the recent climate. However, the duration is prolonged with increasing GWLs, with the maximum duration of 7.85 (9.75; 15.71 and 26.79) days at the 1.5°C (2°C; 3°C; 4°C) GWL. The regional differences of the future changes at the 1.5℃ and 2℃ GWLs are relatively small compared with the 3℃ and 4℃ GWLs (Fig. 3.4q-x). At the 3℃ (4℃) GWL, the duration increases significantly over the entire China and the largest changes appear over Southeast China with a value of 10.27 (21.28) days.

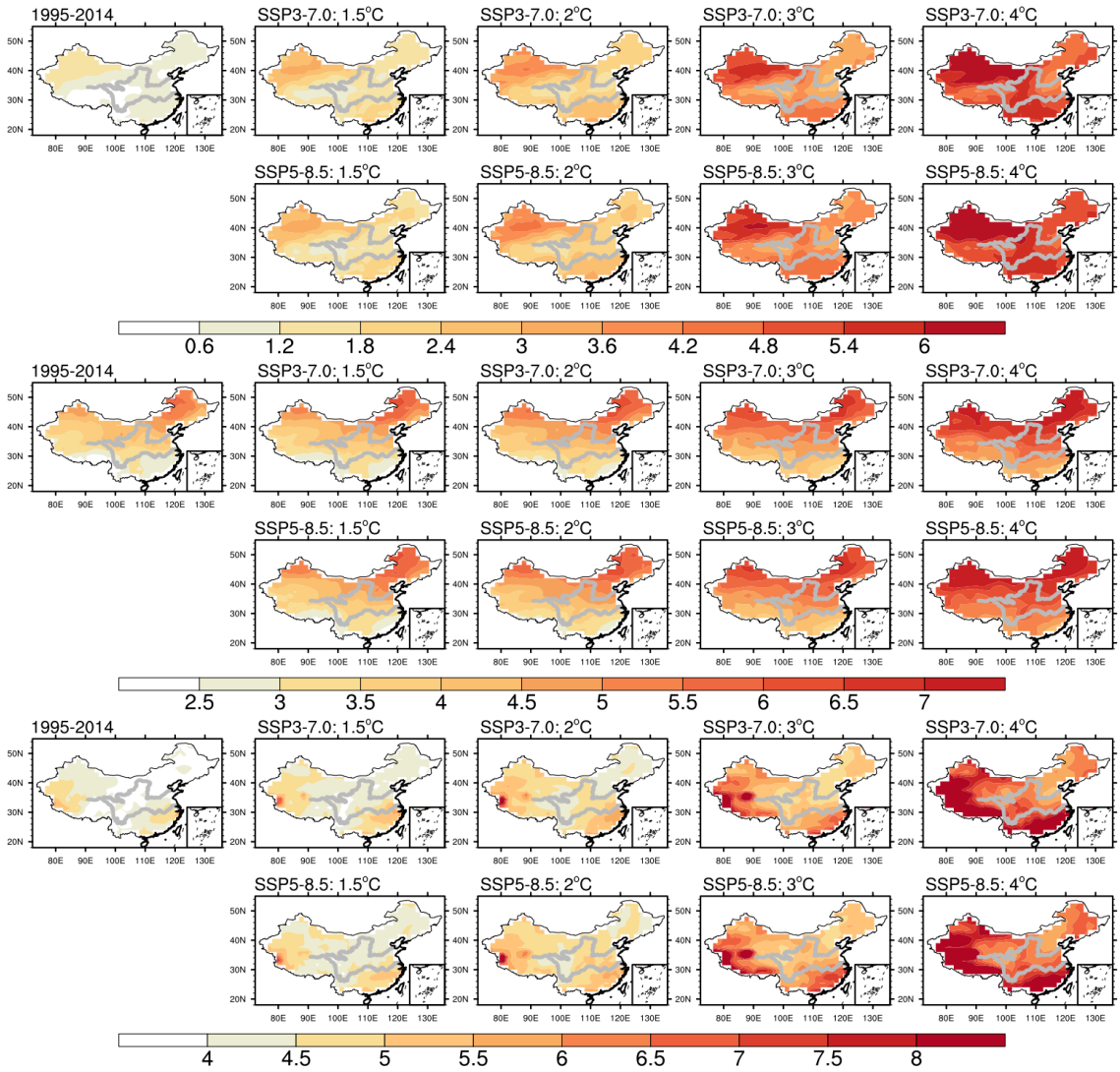

Figure 3.3 The simulated spatial patterns of the frequency (top two rows, units: events·a^{-1}), intensity (middle two rows, units: °C) and duration (bottom two rows, units: days) of Compound HWs in the recent climate (1995-2014), and at the 1.5°C, 2°C, 3°C and 4°C GWLs under the SSP3-7.0 and SSP5-8.5.

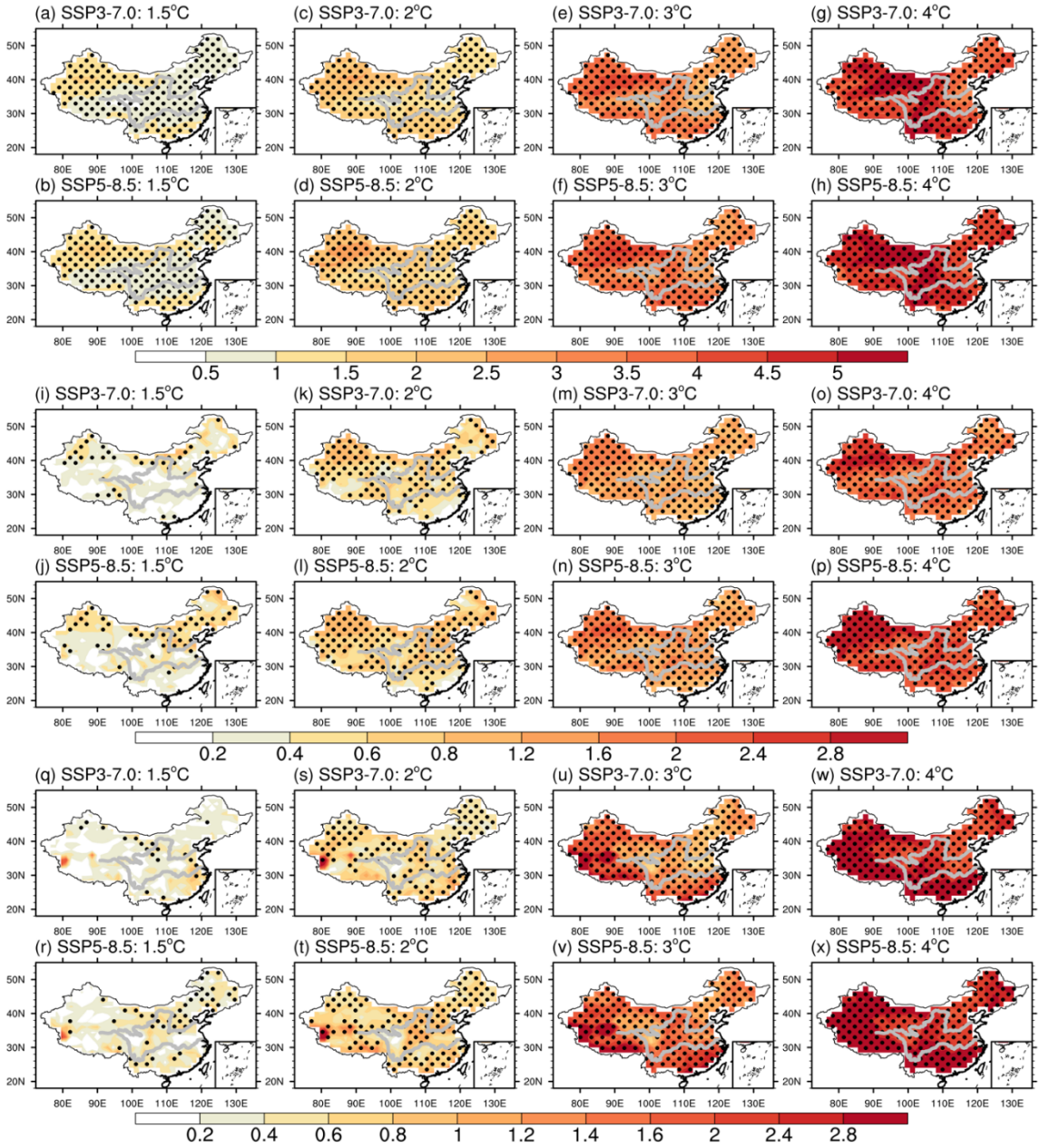

Figure 3.4 The spatial patterns of changes in the frequency (a-h, units: events·a^{-1}), intensity (i-p, units: ℃) and duration (q-x, units: days) of Compound HWs at 1.5°C (2°C; 3°C; 4°C) GWL relative to the recent climate (1995-2014) under the two scenarios. Dots denote regions where at least 7 out of the 9 models agree on the sign of changes.

The regionally averaged changes of Compound HWs properties over the entire China and subregions are shown in Fig. 3.5. The frequency over the entire China increases by about 0.99 (1.75; 3.37; 4.53) events·a^{-1} at the 1.5℃ (2℃; 3℃; 4℃) GWL compared with the recent climate (Fig. 3.5a). The largest change of regional averaged frequency appears over NWC with a range of 1.31-4.95 events · a^{-1}. The intensity of Compound HWs intensifies significantly over the entire China (0.34; 0.63; 1.39; 2.28℃). However, the intensification over NEC and NWC is larger than the other subregions. SEC shows the smallest

intensification of 0.23-2.12℃ (Fig. 3.5b). In terms of duration, Compound HWs last longer over the entire China by 0.35 (0.73; 1.82; 3.65) days at the 1.5℃ (2℃; 3℃; 4℃) GWL relative to the recent climate, especially over SWC with a value of 4.92 days at the 4℃ GWL (Fig. 3.5c). The increase of duration over NWC is the weakest among all subregions. It can be seen that the amplifications in these three properties increase with the GWLs over the entire China and subregions. However, the future changes in Compound HWs vary nonlinearly with the GWLs (Fig. 3.18). For example, the increase in the frequency of HWs is smaller when moving from the 3℃ to 4℃ GWL compared to the 1.5℃ to 3℃ GWL, which is related with the increased changing rate of duration. More short duration HWs change to long duration HWs, leading to the decreased changing rate of frequency. The changing rate of intensity is almost linear which is related to the linear variation of surface air temperature with GWLs. Furthermore, in some boxes of Fig. 3.5, there is a large spread among the models. For frequency, this spread is the smallest at the 4℃ GWL compared with the other GWLs. However, for duration, the model spread increases with increasing GWL.

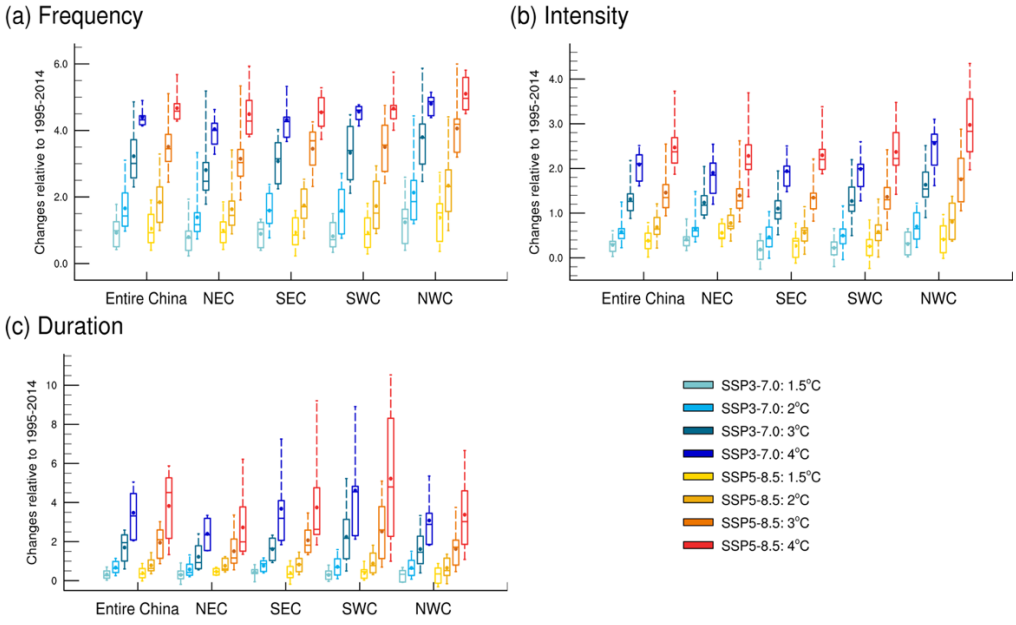

Figure 3.5 Box plots of the regionally averaged changes in the frequency (a, units: events·a^{-1}), intensity (b, units: °C) and duration (c, units: days) of Compound HWs at 1.5°C (2°C, 3°C, 4°C) GWL relative to the recent climate (1995-2014) under the two scenarios over the entire China and subregions. With each box, the horizontal lines from top to bottom denote the maximum value, the 75th percentile, the median value, the 25th percentile and the minimum value of the 9 models. The dot represents the multi-model ensemble mean whose sign agrees with at least 7 out of the 9 models.

Although there is considerable sensitivity in the properties of Compound HWs to the

GWLs, we do not find a large sensitivity to the emissions scenario. That is, the spatial patterns of changes in the frequency, intensity and duration of Compound HWs at different GWLs are similar under the SSP3-7.0 and SSP5-8.5. Table 3.2 provides the spatial pattern correlations between SSP3-7.0 and SSP5-8.5 of the future changes and they show high correlations of about 0.67-0.96. These high spatial pattern correlations, together with similar magnitudes of HW properties changes (Fig. 3.4 and Fig. 3.5) indicate that the future changes of Compound HWs are primarily determined by the GWLs and are not very sensitive to the scenarios.

Table 3.2 The spatial pattern correlation coefficients of the future changes in frequency, intensity and duration of Compound HWs at different GWLs between the SSP3-7.0 and SSP5-8.5.

	1.5 °C	**2 °C**	**3 °C**	**4 °C**
Frequency	0.91	0.96	0.95	0.87
Intensity	0.74	0.84	0.90	0.89
Duration	0.67	0.89	0.94	0.91

Figure 3.6 further illustrates the changes in properties of Compound HWs by showing the ratios of future changes relative to the recent climate at different GWLs. The ratios of frequency are much larger than the other two properties, which can reach 2.26 (3.26; 5.47; 7.07) times of the frequency during the recent climate at the 1.5℃ (2℃; 3℃; 4℃) GWL over the entire China under the SSP5-8.5. From 1.5℃ to 4℃ GWL, the frequency increases by about 3.5 times. For intensity and duration, the ratios at the four GWLs over the entire China are around 1.08-1.90 times of those during the recent climate. SWC exhibits the largest ratios with a range of 2.38-9.51 (1.08-1.80; 1.07-2.20) in frequency (intensity; duration). These ratios mean that the frequency can reach 1.50-6.00 events a^{-1} at different GWLs in comparison with 0.63 events a^{-1} in the recent climate. The intensity will be 3.35-5.58℃ hotter and duration will be 4.46-9.17 days longer at different GWLs in the future climate in comparison with those in the recent climate.

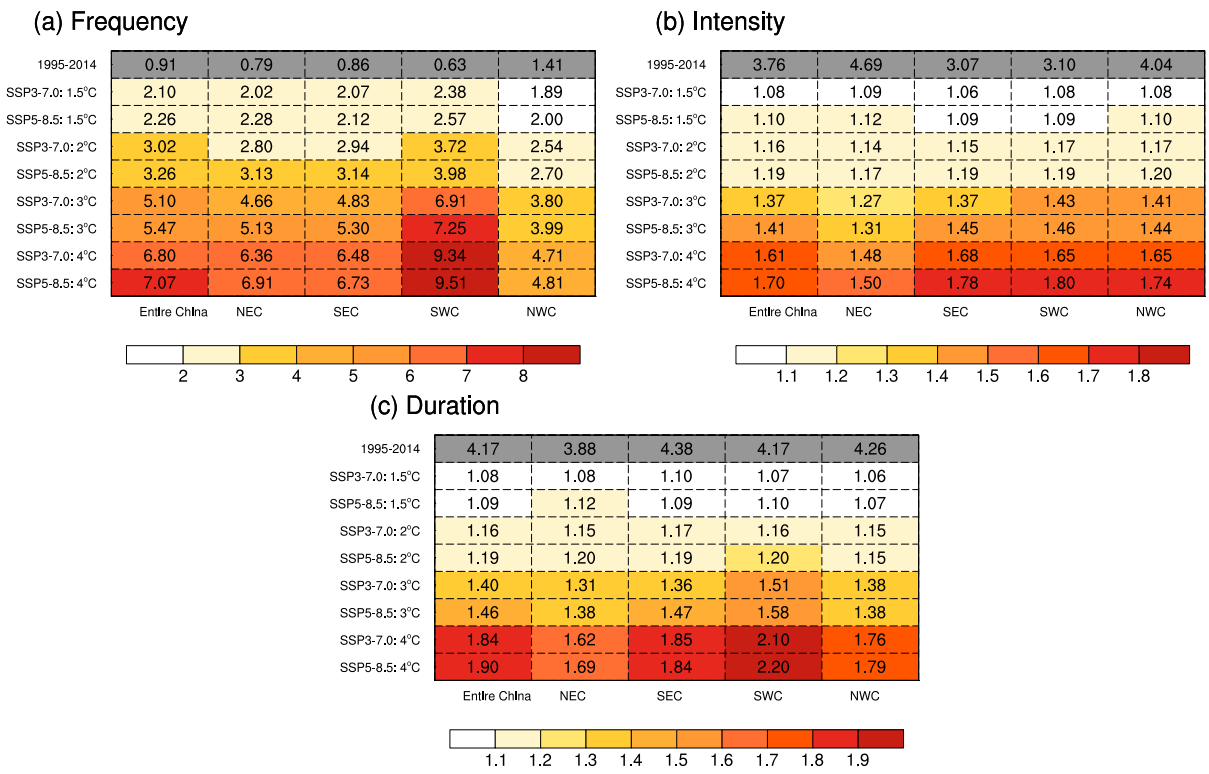

Figure 3.6 The ratios relative to the recent climate (1995-2014) of frequency (a), intensity (b) and duration (c) of Compound HWs at the 1.5°C; 2°C; 3°C and 4°C GWLs under the two scenarios over the entire China and subregions. The first row in each panel is the regional averaged properties over the entire China and subregions in the recent climate (units are events·a^{-1}, °C and days, respectively).

3.3.2 The probability ratios of extreme Compound HWs

Figure 3.7 shows the probability density functions (PDFs) of Compound HWs over the entire China in the recent climate and different GWLs. The PDFs of the four HW properties at different GWLs shift rightward from the recent climate with the largest shift seen at the 4℃ GWL. These shifts indicate both means of HW properties and extreme rare HW events increase with increasing GWL. Heatwave events become more frequent and the temperatures of each event become hotter at different GWLs than those in the recent climate (Fig. 3.7a and b). For duration (Fig. 3.7c and d), the shapes of PDFs at different GWLs become more flattened and right-skewed than the shape in the recent climate, which indicate large increases in extreme long duration events at the four GWLs. Compared with the other three GWLs, the duration becomes much longer at the 4℃ GWL (Fig. 3.7c). The longer duration can constrain the increase of frequency, leading to the weak frequency variance at the 4℃ GWL (Fig. 3.7a). The shapes of the PDFs for max-duration are similar to PDFs shapes of mean duration. In particular, Fig. 3.7d shows that the duration of extreme long-

lasting Compound HWs at the 4°C GWL can reach more than 25 days in summer in comparison with 8 days in the recent climate. In contrast to the PDFs of frequency and duration, the PDFs of intensity show that changes are dominated by a rightward shift with little change in shape for increasing GWLs in comparison with the one in recent climate (Fig. 3.7b). For the most intense events which occur at the 4°C GWL, the variance of intensity increases compared with the recent climate. Figure 3.19 shows the regional averaged PDFs over the four subregions. The main features in changes of PDFs for intensity, duration and max-duration over subregions are similar to the features of changes over the entire China.

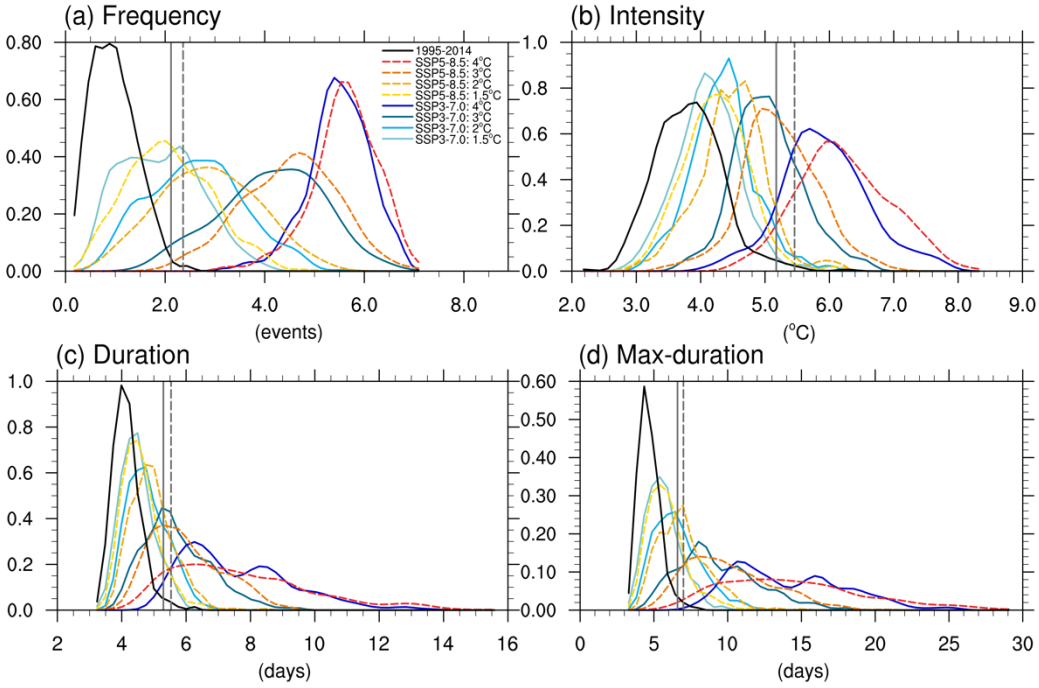

Figure 3. 7 The Kernel smoothing probability density functions (PDFs) of frequency (a), intensity (b), duration (c) and max-duration (d) of Compound HWs over the entire China in the recent climate (black), 1.5°C, 2°C, 3°C and 4°C GWLs. Solid (Dashed) lines represent SSP 3-7.0 (SSP5-8.5). Grey solid (dashed) line represents the threshold of 50-year (100-year) event based on the recent climate of 1995-2014.

To illustrate how the extremely rare HW events will change at different GWLs, the grey lines in Fig. 3.7 show the thresholds of 50-year and 100-year events based on the recent climate. The probabilities of these two kinds of extremely rare events increase significantly with increasing GWLs and they will become much more frequent in the future. Furthermore, the quantitative analysis about probability ratios of these two extreme Compound HWs over different regions is summarized in Fig. 3.8. In particular, the PRs for frequency (Fig. 3.8a,

d) are much larger than the PRs of intensity and duration. However, the regional differences in the PRs are not obvious among the subregions. The PRs of the two extreme rare events increase gradually with the increasing of GWLs. Especially, the PRs are close to 50 (100) for the 50-year (100-year) event at the 4℃ GWL, which indicates these two kinds of extreme rare events will become 1-year events. For intensity (Fig. 3.8b, e), the probabilities of the two extreme rare events show weak changes at the 1.5℃ and 2℃ GWLs relative to the recent climate. At the 3℃ and 4℃ GWLs, NWC exhibits the largest PRs with a value of 29.08 and 44.87 (37.11 and 81.58) for the 50-year (100-year) event, so that the 50-year (100-year) event in the recent climate will become a 1.7-year and 1.1-year (2.7-year and 1.2-year) event in the future. From the 1.5℃ to 4℃ GWL, the PRs of duration of 50-year (100-year) event over the entire China increase from 4.57 (3.54) to 48.57 (93.21) (Fig. 3.8c, f). The PRs of duration over SWC are the largest among the subregions. At the 4℃ GWL, the 50-year and 100-year events over SWC will become 1-year and 1.2-year events, respectively.

In summary, the analyses about HW properties change at different GWLs suggest that HWs over China become more frequent, event temperature becomes hotter, and event duration becomes longer at different GWLs than those in the recent climate. The magnitudes of these changes depend on GWLs but they are not very sensitive to scenarios. Specifically, at the 4℃ GWL, the frequency of HWs increases by more than five-fold under both scenarios, and the intensity (duration) of HWs averaged under the two scenarios is 2.28°C hotter (3.59 days longer) than the one in the recent climate over the entire China. Furthermore, the maximum duration of HW events can reach more than 25 days in summer at 4℃ GWL in comparison with 8 days in the recent climate. The extreme rare events (50-year and 100-year events) in the recent climate would become the norm over China and four sub-regions at 4℃ GWL.

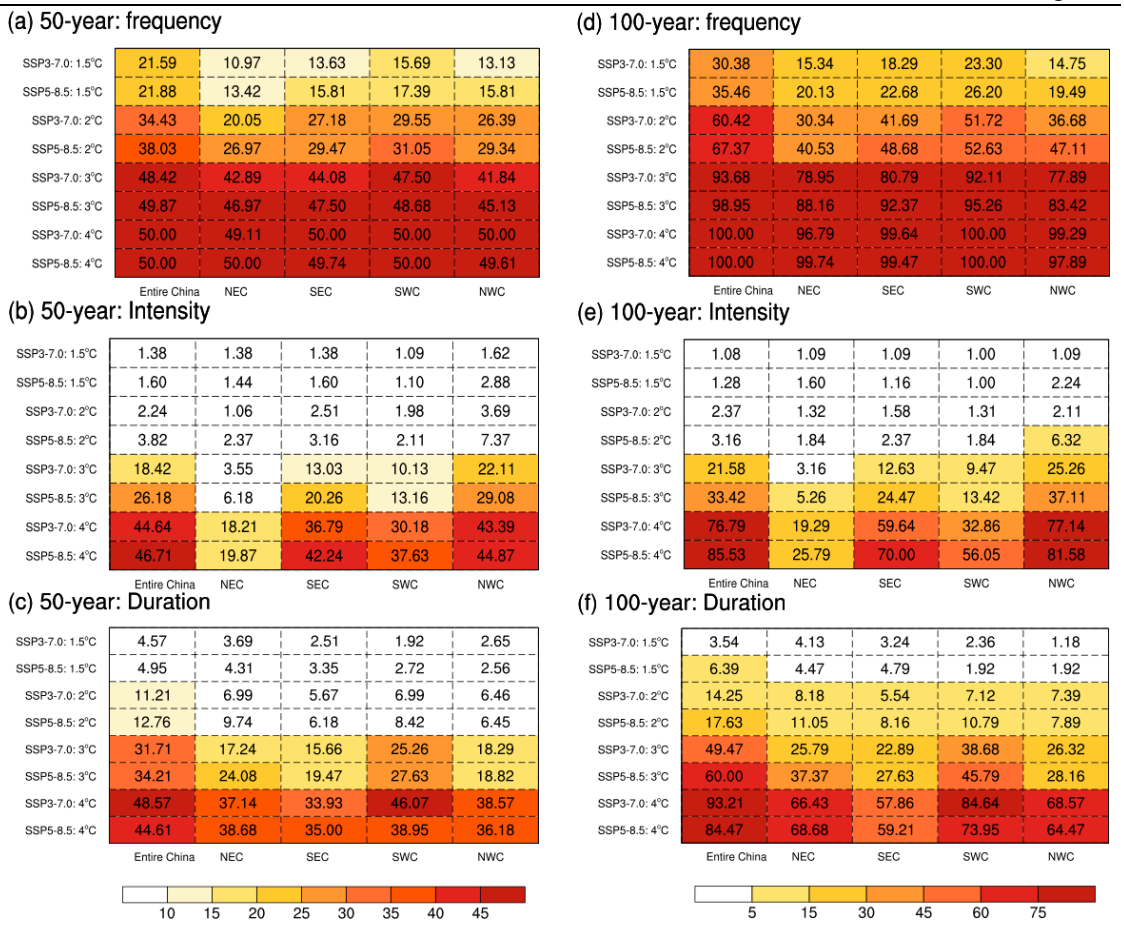

Figure 3.8 The probability ratios of frequency, intensity and duration of a 50-year (a-c) and 100-year (d-f) Compound HWs at the 1.5°C; 2°C; 3°C and 4°C GWLs relative to the recent climate (1995-2014) under the two scenarios over the entire China and subregions.

3.4 The responsible physical processes related to the changes of Compound HWs properties

3.4.1 The roles of seasonal mean temperature and temperature variability changes on HW property changes

Future changes in the properties of HWs in global warming worlds can be contributed by the changes in the climatological seasonal mean temperature and the changes in temperature variability (Argueso et al., 2016; Su and Dong, 2019a). Figure 3.9 shows the future changes of summer mean Tmax and Tmin at different GWLs relative to the recent climate. Overall, the spatial patterns of the temperature change are similar at the four GWLs. However, the future changes of seasonal mean temperature do show significant regional differences. In particular, the magnitude of temperature change increases from south to north and the largest increase at each GWL appears over Northwest China, which is consistent

with the larger increase of future changes in frequency and intensity of HWs over the northern part of China.

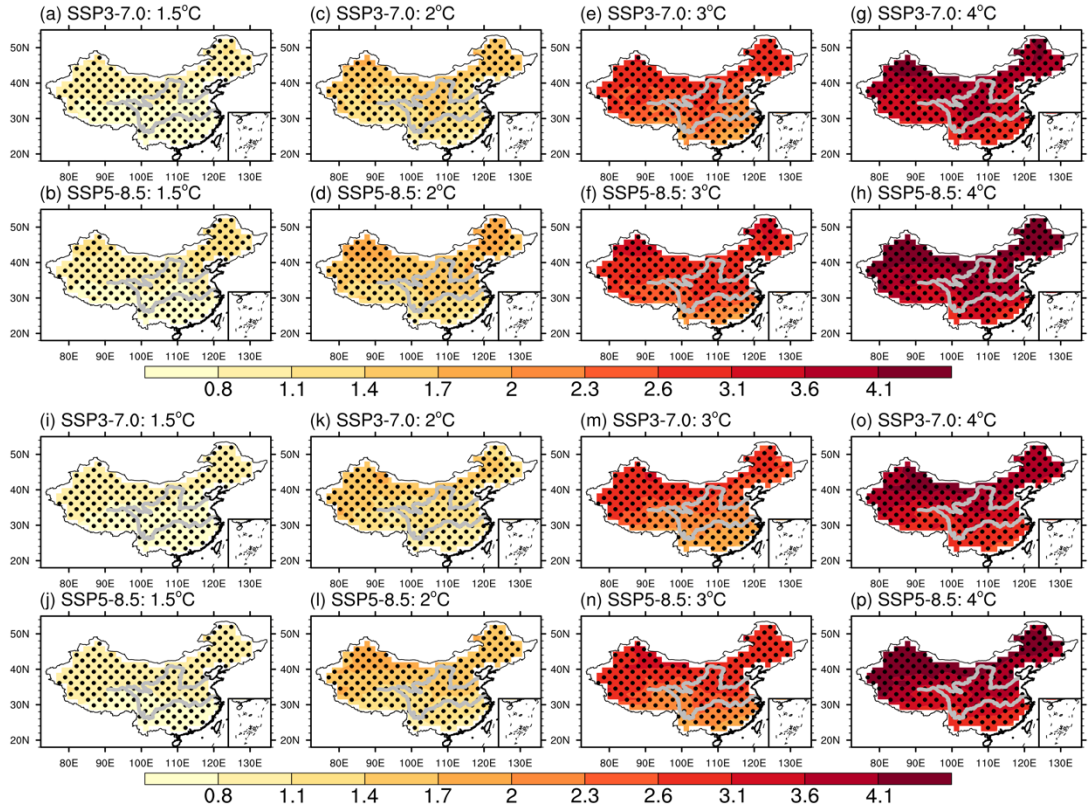

Figure 3.9 The spatial patterns of changes in summer mean Tmax (a-h, units: °C) and Tmin (i-p, units: °C) at 1.5°C (2°C; 3°C; 4°C) GWL relative to the recent climate (1995-2014) under the two scenarios. Dots denote regions where at least 7 out of the 9 models agree on the sign of changes.

Figure 3.10 shows the PDFs of daily Tmax and Tmin averaged over the entire China and the four subregions. The PDF shapes of Tmax and Tmin at different GWLs and recent climate have similar distribution patterns except a shift to increasing temperatures with increasing GWL. After removing the corresponding local mean temperature at the different GWLs, the distributions of daily temperature anomalies at different GWLs are very similar. Therefore, the Tmax and Tmin at different GWLs have similar daily to sub-seasonal time scale variability. However, the PDFs of Tmax anomalies at the 4°C GWL under the SSP3-7.0 do show some differences from other PDFs (Fig. 3.10k-o), but this may be due to the fact that only 6 models can reach the 4°C GWL under this scenario compared with 9 models at other GWLs. Figure 3.20 illustrates the PDFs of Tmax anomalies with the same model members at the four GWLs and they show very similar distributions, suggesting that slightly

different PDF distributions at the 4°C GWL under the SSP3-7.0 in comparisons with those in other GWLs shown in Fig. 3.10 are mainly due to less model members reaching 4°C GWL under this scenario.

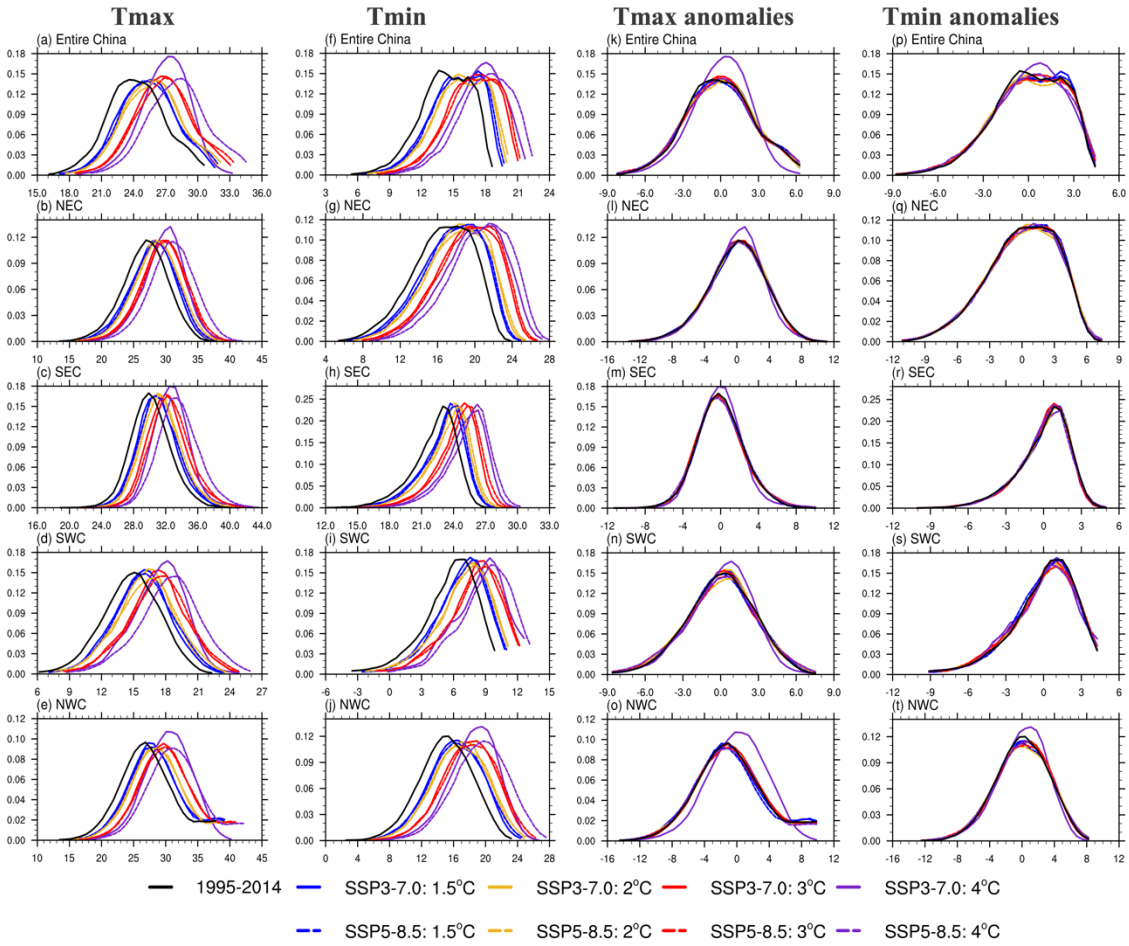

Figure 3.10 The Kernel smoothing probability density functions of daily Tmax (a-e), daily Tmin (f-j), daily Tmax anomalies (k-o) and daily Tmin anomalies (p-t) relative to corresponding mean Tmax and Tmin in each GWLs averaged over the entire China and the four subregions.

To further assess the roles of seasonal mean temperature changes and temperature variability changes on HW property changes, reconstructed Tmax and Tmin time series for each GWL are made by adding the summer climatological mean Tmax and Tmin differences between two periods (GWL minus the recent climate) to the original daily Tmax and Tmin time series during the recent climate. In this way, the reconstructed time series at each GWL have the same temperature variability as the original time series during the recent climate but with the seasonal mean warming added. Therefore, any difference in Compound HW properties between the reconstructed time series at each GWL and the time series during the recent climate are due to the seasonal mean warming signal. In contrast, the differences in

Compound HW properties between the original time series for future climate and reconstructed time series are due to temperature variability. Figure 3.11 shows that the role of the seasonal mean warming dominates the changes in the HW properties at the different GWLs over the entire China, especially for increases in frequency. For each subregion, the seasonal mean warming also plays a dominant role on the changes in the HW properties (Fig. 3.21). The importance of seasonal mean warming is consistent with the previous studies that the seasonal mean temperature changes control future HWs across the world and in different regions (Argueso et al., 2016; Su and Dong, 2019a; Zhao et al., 2019). Therefore, it's reasonable to analyze the changes of physical variables in climatological seasonal mean state between different GWLs and the recent climate to discuss the responsible physical processes. Although the future changes of HWs are not very sensitive to scenarios, there are still a few differences between these two scenarios. Meanwhile, considering the difference in radiative forcing between the SSP5-8.5 and SSP3-7.0, the physical processes of these two scenarios will be analyzed separately.

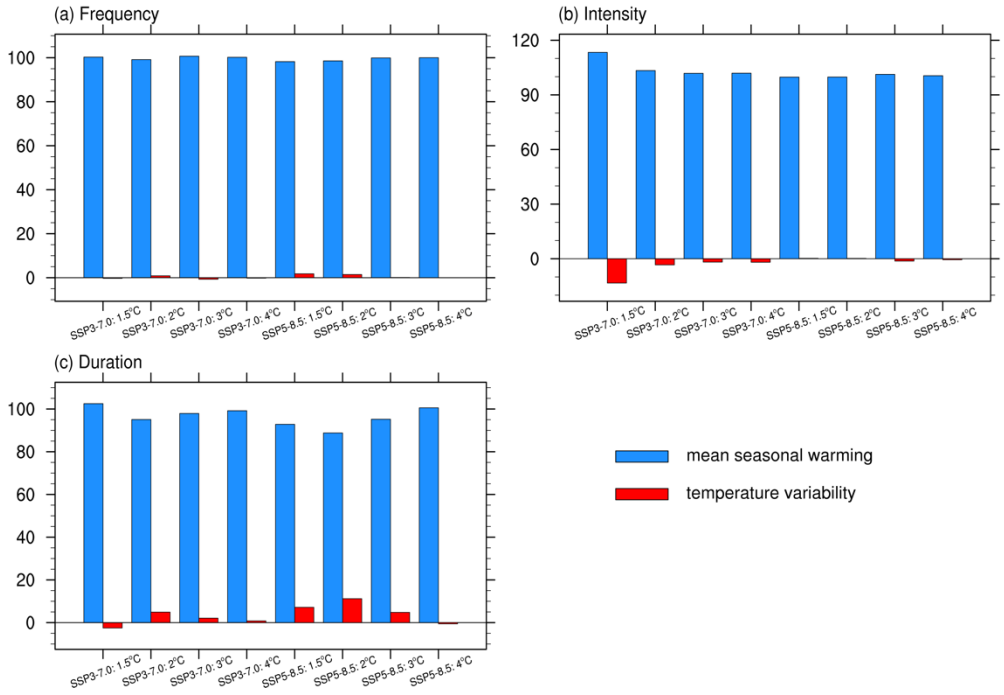

Figure 3.11 The contributions of seasonal mean warming (blue bar) and changes in temperature variability (red bar) to the future changes of frequency (a), intensity (b) and duration (c) of Compound HWs averaged over the entire China at different GWLs (units: %).

3.4.2 The physical processes under the SSP5-8.5

Figure 3.12 shows seasonal mean changes in some key variables at different GWLs

relative to the recent climate. The surface clear-sky downward longwave radiation increases significantly over China, with large increases over NWC and eastern China (Fig. 3.12a-d). The magnitudes of changes increase with increasing GWLs. These increases are likely to be partly due to the increase in greenhouse gas forcing and partly due to the increase of water vapor in the atmosphere related to warming (Fig. 3.12m-p). The southwesterly wind anomalies over SEC and the anomalous moist air flow from the Pacific Ocean (Fig. 3.12e-h) lead to increased moisture transport over eastern China, and is likely responsible for large increases in water vapor and increase in relative humidity there (Fig. 3.12i-l). The anomalous wind along the east periphery of the Tibetan Plateau will also transport water vapor to NWC (Fig. 3.12m-p). The increases in clear sky downward longwave radiation tend to warm the surface temperature, which is beneficial for the increases of Compound HWs over China. As the temperature differences between the surface and atmosphere increase, upward sensible heat fluxes from the surface to the atmosphere will also increase. The increased water vapor is also associated with increasing precipitation across China (Fig. 3.12q-t). The increased precipitation is beneficial for the increases of soil moisture through a positive feedback, since the water added to the land surface during rainfall leads to increased evaporation and this can lead to further precipitation in return (Douville et al., 2001; Sehler et al., 2019). Influenced by the strong controlling of soil moisture on evapotranspiration, the increased soil moisture contributes to the increase of water vapor in the atmosphere, which absorbs both shortwave and longwave radiation. (Fig. 3.12u-x, Xu et al., 2019). Due to the condensation during a precipitation event, the latent heat is released from water vapor and therefore transfers from the surface to the atmosphere. The increased upward sensible heat fluxes and the release of positive latent heat are beneficial for the warming of air temperature (Song et al., 2022), and then contributes to intensification of HWs over China. Hence, the increased heat fluxes are responsible for the stronger, longer and more frequent Compound HWs over China in the future climate.

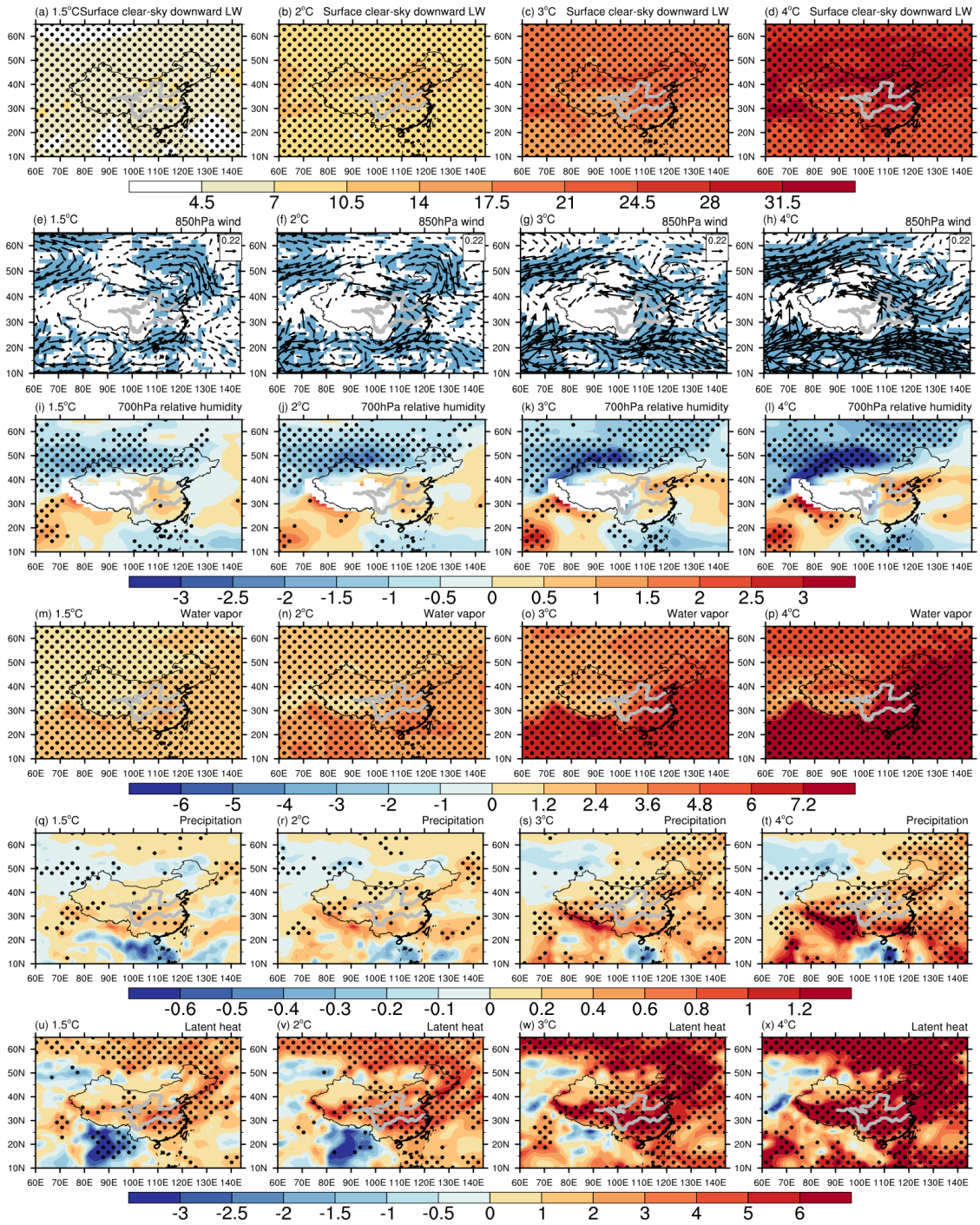

Figure 3.12 Spatial distributions of the changes in surface clear-sky downward longwave radiation (a-d, units: $W \cdot m^{-2}$), 850hPa wind (e-h, vector, units: $m \cdot s^{-1}$), 700hPa relative humidity (i-l, units: %), vertically integrated water vapor through the atmospheric column (m-p, units: $kg \cdot m^{-2}$), precipitation (q-t, units: $mm \cdot day^{-1}$), and latent heat (u-x, units: $W \cdot m^{-2}$, positive values mean upward) at 1.5℃ (2°C; 3°C; 4°C) GWL under the SSP5-8.5 relative to the recent climate. Shading in e-h and dots in a-d; i-x denote regions where at least 7 out of the 9 models agree in the sign of changes.

The spatial patterns of some variables related to changes of aerosol forcing are illustrated in Fig. 3.13. At the 2°C; 3°C and 4°C GWLs, the aerosol optical depth (AOD) at

550nm decreases significantly over eastern China (Fig. 3.13c-d). However, due to the relatively weak changes of aerosol emission at the 1.5℃ GWL compared with the recent climate, there is a large spread in AOD at 550nm across models and there are even positive changes over the NEC (Fig. 3.13a). A detailed analysis related to the spread in future projections will be discussed in the later chapter. Influenced by aerosol-radiation interactions (Hatzianastassiou et al., 2007, Boucher et al., 2013), the decrease of AOD at 550nm results in the increase of net surface clear-sky shortwave radiation (Fig. 3.13e-h), which will also tend to warm the surface over eastern China. Larger changes in net surface shortwave radiation than clear sky shortwave radiation over eastern China indicate that part of surface shortwave radiation changes is related to an increased shortwave cloud radiative effect (Fig. 3.13i-l), induced by decreases in total cloud cover (Fig. 3.13m-p), related to aerosol-cloud interactions (Boucher et al., 2013). These increases in net surface shortwave radiation also make contributions to the surface warming. Therefore, the warming of surface temperature leads to the increasing of HWs over eastern China.

Considering the regional differences in HWs properties changes, the large increases in frequency and intensity of Compound HWs over the NWC are consistent with large increases in Tmin in the region (Fig. 3.9), which is likely related to the large increases in longwave radiation. Therefore, increases in both shortwave and longwave radiation appear responsible for increases in Tmax and Tmin over eastern China, leading to larger increases in frequency over the SEC and intensity over the NEC. Duration changes show large increases in SWC and SEC where model climatology also show long duration of Compound HWs, suggesting that duration changes might depend on the model climatology.

In summary, the surface warming across China seen in summer in the future climate is related to an increase in longwave radiation, partly resulted from the increase in greenhouse gas forcing and partly resulted from increased water vapor, and an increase in shortwave radiation over eastern China related to decreases in aerosols. The regional variations in the water vapor over China are consistent with atmospheric circulation changes. These seasonal mean surface warming results in enhanced upward sensible and latent heat fluxes, consistent with increased summer mean Tmax and Tmin and the enhancement of Compound HWs

properties over China. Moreover, with the increasing of GWL, the magnitudes of the changes increase, which indicates that the influence of these processes on Compound HWs intensifies.

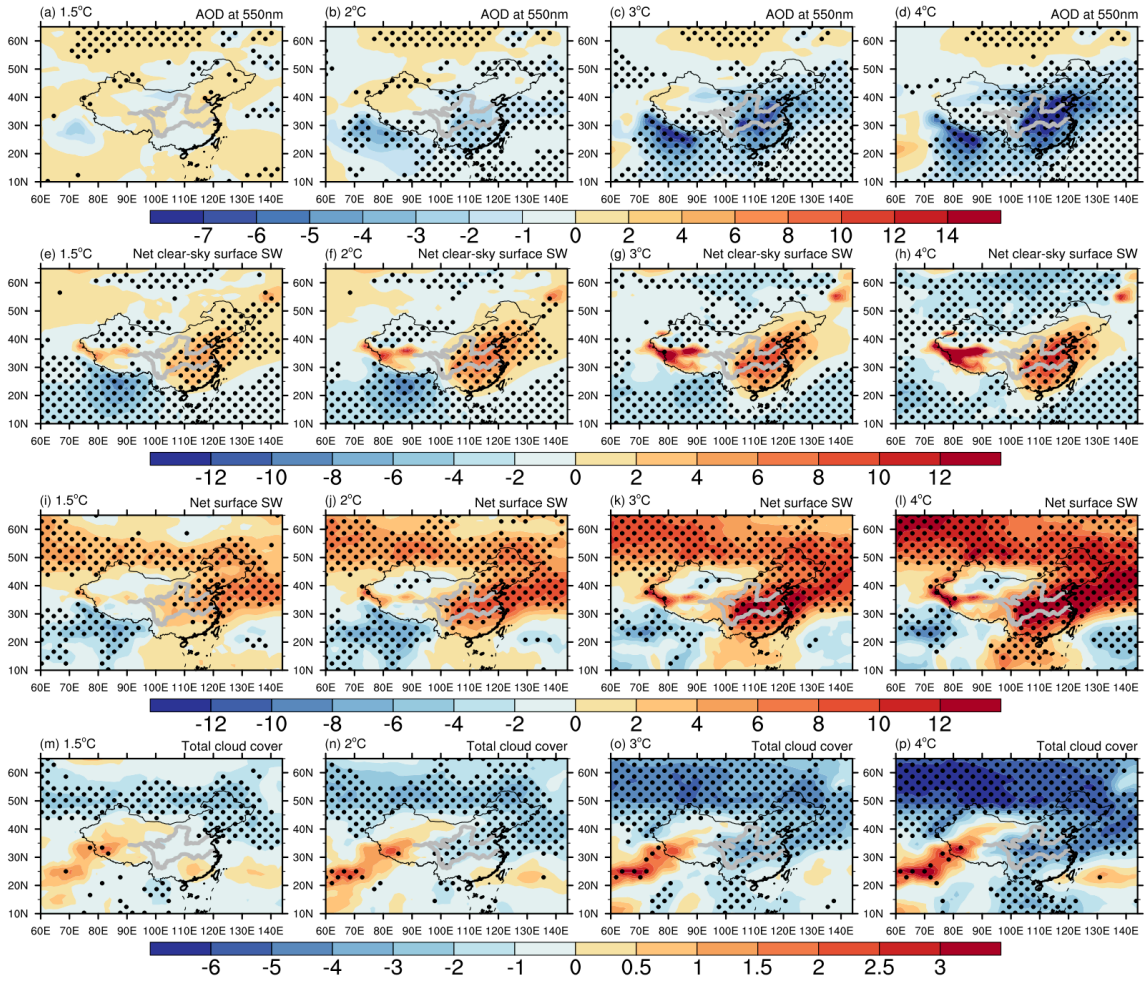

Figure 3.13 Spatial distributions of the changes in aerosol optical depth (AOD) at 550nm (a-d, units: 10^{-3}, results are based on 5 models in which AOD is available), net clear-sky surface shortwave radiation (e-h, units: $W \cdot m^{-2}$), net surface shortwave radiation (i-l, units: $W \cdot m^{-2}$), and total cloud cover (m-p, units: %) at 1.5℃ (2°C; 3°C; 4°C) GWL under the SSP5-8.5 relative to the recent climate. Dots denote regions where at least 7 out of the 9 models agree in the sign of changes, but only 3 out 5 models in AOD.

3.4.3 The physical processes under the SSP3-7.0

The physical processes for the longwave radiation changes at different GWLs under the SSP3-7.0 are shown in Fig. 3.22. Many characteristics of changes are similar to the processes under the SSP5-8.5 and so are not discussed in detail here. The low-level wind anomalies lead to increased water vapor in the atmosphere over eastern China. The moistening

atmosphere is contributing to significant increase of surface clear-sky downward longwave radiation across China.

Considering the role of shortwave radiation under the SSP3-7.0, Fig. 3.14 shows the future changes of the related variables. There is a distinct difference in the changes of AOD at 550nm compared with the ones under the SSP5-8.5. The AOD at 550nm increases significantly over eastern China (Fig. 3.14a-d), which leads to the reduction of net clear-sky surface shortwave radiation (Fig. 3.14e-h). Therefore, the net clear-sky surface shortwave radiation plays an opposite role under the SSP3-7.0, which leads to surface cooling. It is consistent with the assumptions regarding aerosol emissions in these two scenarios. In SSP5-8.5, strong air pollution control measures are assumed globally, leading to a significant reduction in aerosol emissions, which is conducive to the intensification of HWs. While, SSP3-7.0 assumes weaker air quality regulations, resulting in regional increases of aerosol emissions, which potentially reduces the extent of HWs intensification (O'Neill et al., 2017). As a result of the decreases in total cloud cover (Fig. 3.14m-p), the net surface shortwave radiation only increases over the NEC at the 1.5℃ and 2℃ GWLs (Fig. 3.14i-j) and the changes of the net surface shortwave radiation over eastern China at the 3℃ and 4℃ GWLs (Fig. 3.14k-l) are much weaker and therefore they play a weaker role for surface warming than the ones under the SSP5-8.5. The increased shortwave and longwave radiation over eastern China contribute to increases in both Tmax and Tmin and are responsible for large increases in HW frequency and intensity.

To sum up, the surface warming in summer over China under the SSP3-7.0 is mainly contributed by the increased longwave radiation with weak contribution from changes in net surface shortwave radiation. The seasonal mean surface warming results in enhanced upward sensible and latent heat fluxes, leading to increases in Tmax and Tmin and resulting in the increase of Compound HWs across China.

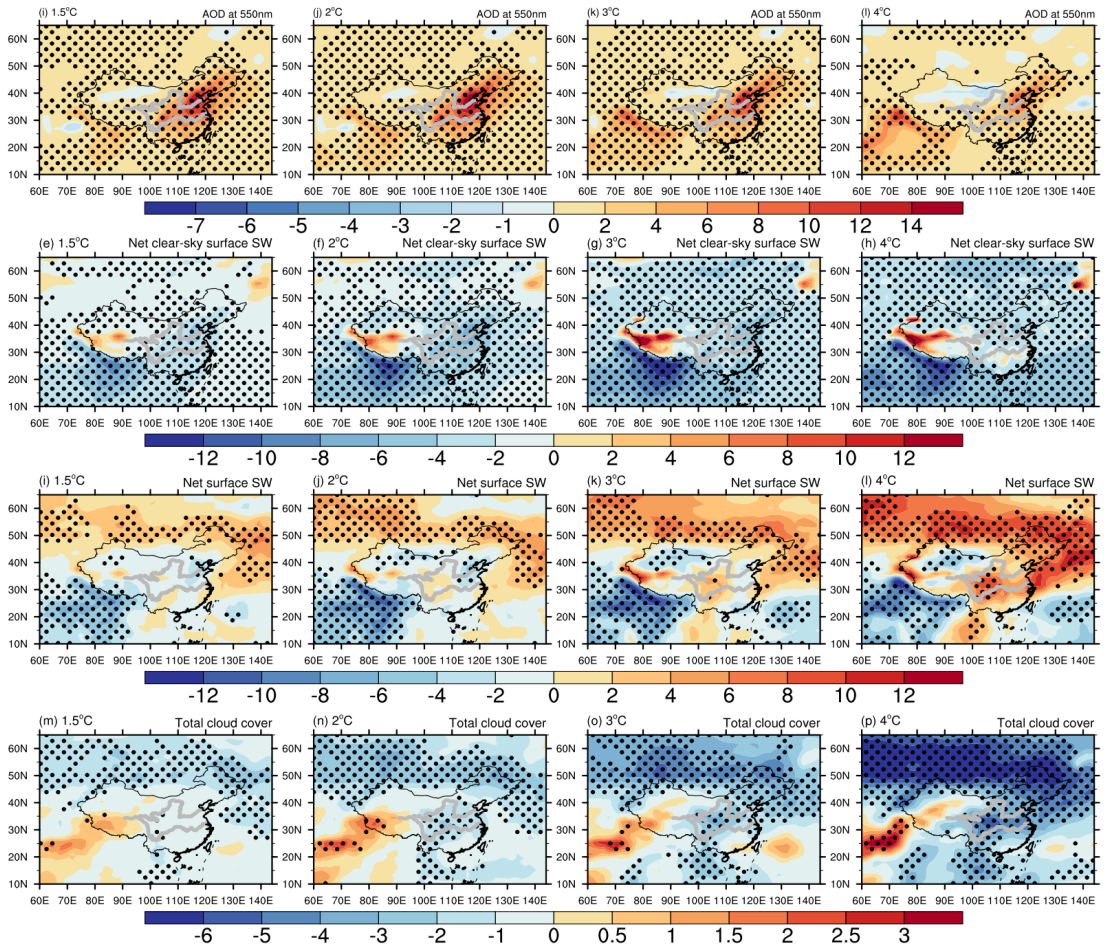

Figure 3.14 Spatial distributions of the changes in AOD at 550nm (a-d, units: 10^{-3}, results are based on 5 models in which AOD is available), net clear-sky surface shortwave radiation (e-h, units: W·m^{-2}), net surface shortwave radiation (i-l, units: W·m^{-2}), and total cloud cover (m-p, units: %) at 1.5℃ (2°C; 3°C; 4°C) GWL under the SSP3-7.0 relative to the recent climate. Dots denote regions where at least 7 out of the 9 models agree in the sign of changes, but only 3 out 5 models in AOD.

3.5 Conclusions

Under the influence of global warming, there will be an increase of warm extremes over China. This chapter quantified the expected changes in the frequency, intensity, and duration of summer Compound Heat Waves (HWs) over China using CMIP6 simulations and explored the associated physical processes. In particular, the future changes of summer Compound HWs over China is explored at global warming levels (GWLs) representative of changes in global mean surface temperature at the 1.5°C, 2°C, 3°C and 4°C based on the multi-model ensembles of CMIP6 under the SSP3-7.0 and SSP5-8.5. The main conclusions can be summarized as follows.

The spatial climatological distributions of the properties of Compound HWs have

similar patterns in the recent climate and in the future four GWLs under two scenarios. Therefore, one important conclusion is that the magnitudes and spatial distributions of future changes of Compound HWs are primarily dependent on GWLs and they are not very sensitive to scenarios. The heatwave events over China become more frequent, event temperature becomes hotter, and event duration becomes longer at different GWLs than those in the recent climate. However, the magnitudes of changes increase with increasing GWL. For example, at a 4℃ GWL, the frequency of HWs increases by more than five-fold under both scenarios, and the intensity (duration) of HWs averaged under the two scenarios is 2.28°C hotter (3.59 days longer) than those in the recent climate over the entire China. Furthermore, the maximum duration of HW events can reach more than 25 days in summer at 4℃ GWL in comparison with 8 days in the recent climate.

Although the changes in frequency, intensity and duration of Compound HW scale broadly across China with GWL, these properties show some regional differences. For example, the increases of the occurrence of Compound HWs over NWC are the largest among the subregions. Furthermore, NEC and NWC show the greatest intensification in intensity and the increases in duration over SWC are much longer than the other regions.

The probability ratios (PRs) of the extreme rare Compound HWs over China increase with increasing GWLs. The 50-year and 100-year rare events are projected to become 1-year event at the 4℃ GWL across China. NWC shows the largest PRs of intensity at the 3℃ and 4℃ GWLs, so that the 50-year (100-year) high-intensity event is projected to become a 1.7-year and 1.1-year (2.7-year and 1.2-year) event in the future. The PRs of duration over SWC are the largest among the subregions and the 50-year and 100-year long-duration events over SWC are projected to become 1-year and 1.2-year events, respectively.

The summer seasonal mean changes in Tmax and Tmin dominates the changes in Compound HW properties over China at the different GWLs. However, the processes leading to the changes in Tmax and Tmin are scenario dependent. Under the SSP5-8.5, the surface warming across China is related to the increases of longwave radiation, partly resulted from increase in greenhouse gas forcing and partly resulted from increased water vapor and the increases of shortwave radiation over eastern China related to decreases in

aerosols. The regional variations in the water vapor over China are consistent with atmospheric circulation changes. This seasonal mean surface warming results in enhanced upward sensible and latent heat fluxes, leading to increased summer mean daily maximum and minimum of near-surface air temperature (Tmax and Tmin) and the enhancement of Compound HWs properties over the entire China. Under the SSP3-7.0, the surface warming in summer over China is mainly contributed by the increased longwave radiation with weak contribution from changes in net surface shortwave radiation related to increased aerosol changes under this scenario. The seasonal mean surface warming results in enhanced upward sensible and latent heat fluxes, leading to increases in Tmax and Tmin and resulting in the increase of Compound HWs across China. In terms of the regional differences of changes in HWs properties, the large increases in frequency and intensity are mainly contributed by the longwave and shortwave radiation.

Our results suggest that China would face a future with projected frequency increase, intensity enhancement and duration extension of HWs. Considering the severe impacts of HWs on human well-being and ecosystem (Yin et al., 2023a), our results provide important context for the development of mitigation and adaption decisions to reduce the adverse impacts of HWs on society.

This study provides a view on the future changes of summer Compound HWs and the related physical processes at different GWLs. The results are based on multi-model ensembles of CMIP6 and, thus, more robust than results from a single model. Nevertheless, as demonstrated in Fig. 3.5, there is a large spread of future projections in Compound HWs properties among the models. Unfortunately, the reasons for this model uncertainty are still unclear. Understanding this spread is an important question and needs further study in order to improve predictions of future changes in HWs over China.

Acknowledgements

We acknowledge the international modeling groups for providing their data for analysis, the Program for Climate Model Diagnosis and Inter-comparison (PCMDI) for collecting and achieving the model data, the World Climate Research Programme's (WCRP's) Coupled

Model Inter-comparison Project (CMIP) for organizing the model data analysis activity. We would like to thank Prof. Andrew Turner and Dr. Laura Wilcox for providing suggestions which help to improve this paper. The authors greatly appreciate two anonymous reviewers for their constructive comments and suggestions on the early version of this paper.

Data Availability

The CMIP6 datasets were obtained from CEDA (https://data.ceda.ac.uk/badc/cmip6/data/CMIP6). The observation data CN05 used in Supplementary file was download from CMA (http://www.nmic.cn).

3.6 Supporting information

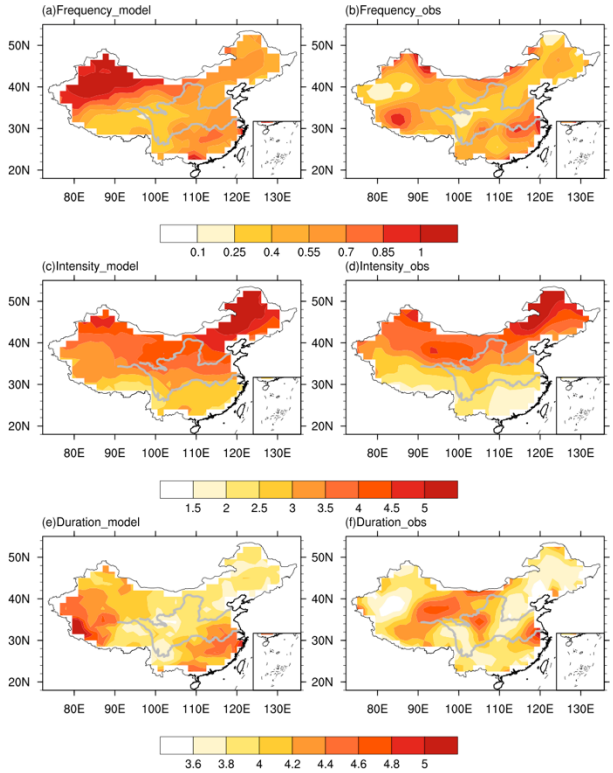

Figure 3.15 The spatial patterns of climatology in frequency (a-b, units: events·a^{-1}), intensity (c-d, units: °C) and duration (e-f, units: days) of Compound HWs during the historical period (1961-2020) based on model simulations and observations. The observation data is derived from the gridded CN05.2 dataset.

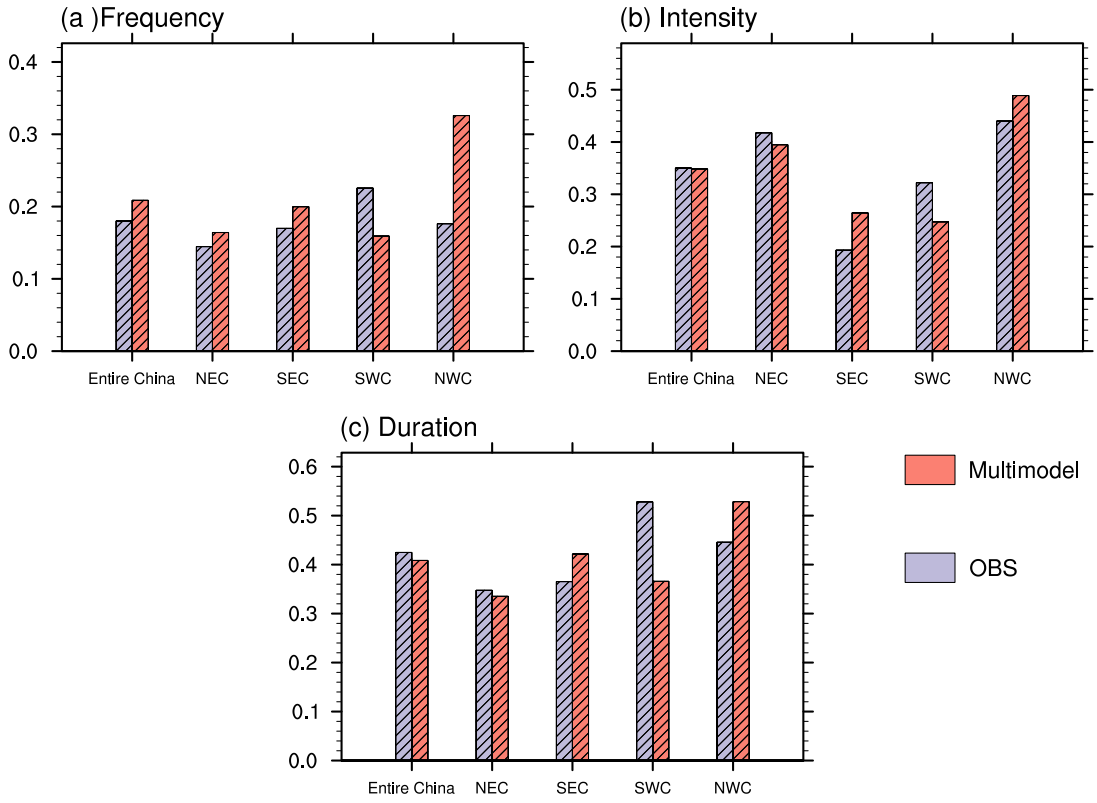

Figure 3.16 The linear trends of HWs frequency (a, units: events·10yr^{-1}), intensity (b, units: °C·10yr^{-1}) and duration (c, units: days·10yr^{-1}) based on observation and model simulations during the period 1961-2020 over the entire and the four subregions. The shadow represents the trend is statistically significant at the 0.05 level.

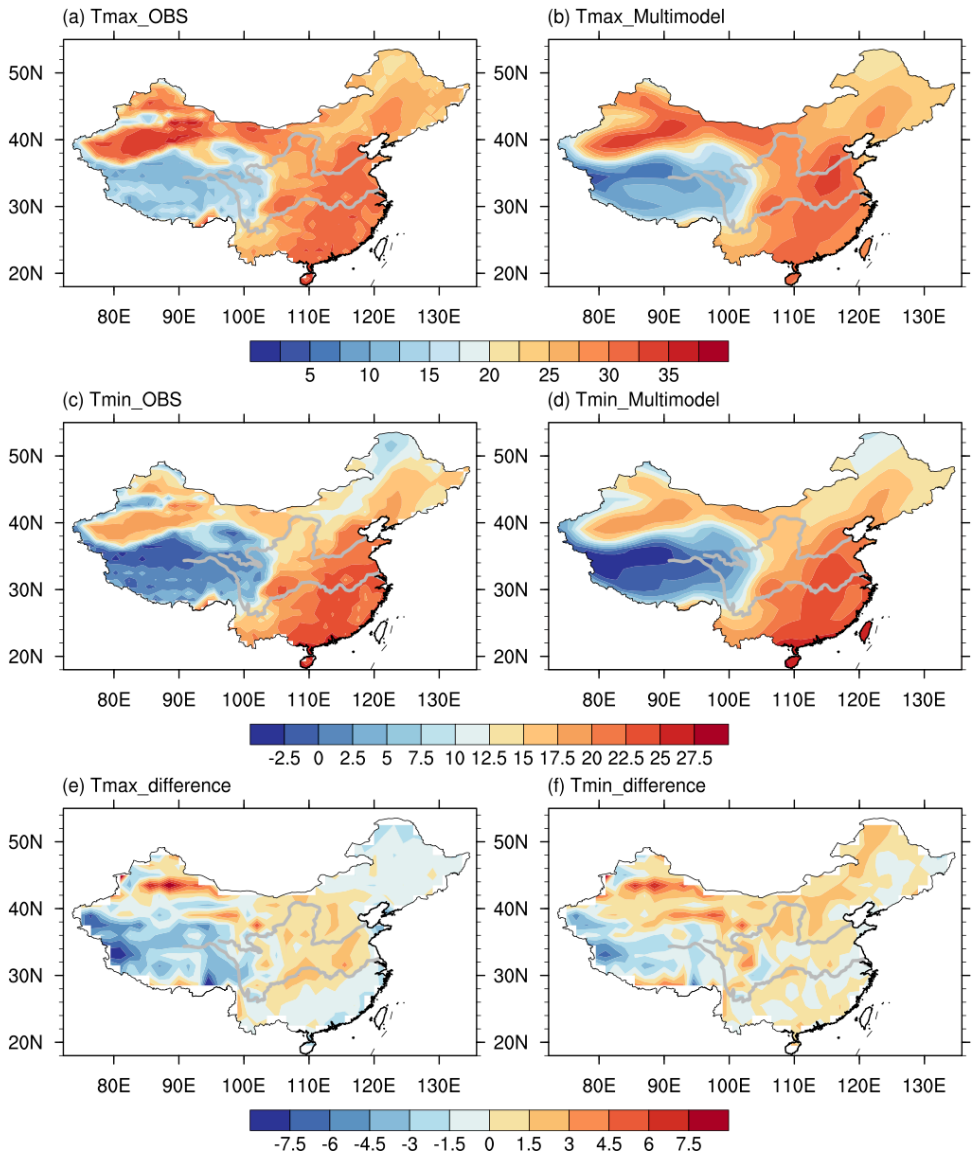

Figure 3.17 The spatial patterns of climatology in Tmax and Tmin (a-d, units: °C) during the historical climate (1961-2020) based on observations and model simulations, and the differences of Tmax and Tmin (e-f, units: °C) between model simulations and observations.

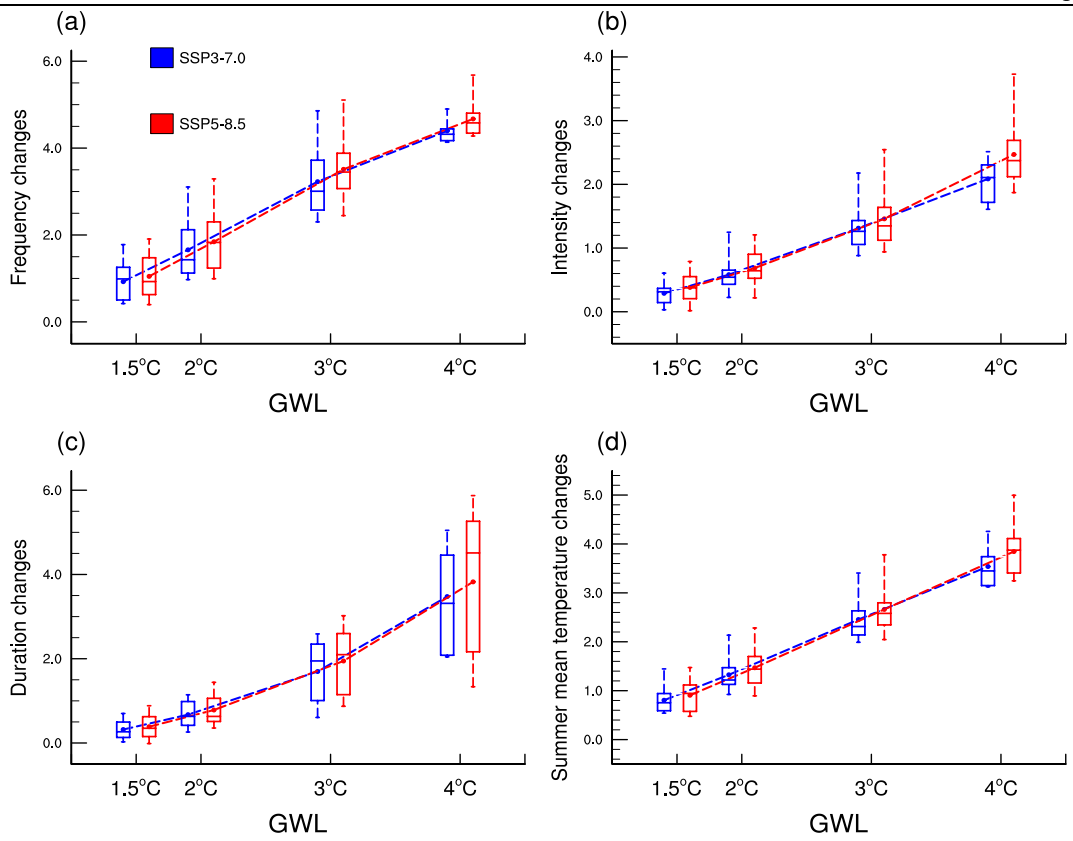

Figure 3.18 Box plots of the regionally averaged changes in the frequency (a, units: events·a^{-1}), intensity (b, units: °C), duration (c, units: days) of Compound HWs and summer mean temperature (d, units: °C) at 1.5°C (2°C, 3°C, 4°C) GWL relative to the recent climate (1995-2014) under the two scenarios over the entire China. With each box, the horizontal lines from top to bottom denote the maximum value, the 75th percentile, the median value, the 25th percentile and the minimum value of the 9 models. The dot represents the multi-model ensemble mean. The dashed lines are the line-plot of multi-model ensemble mean.

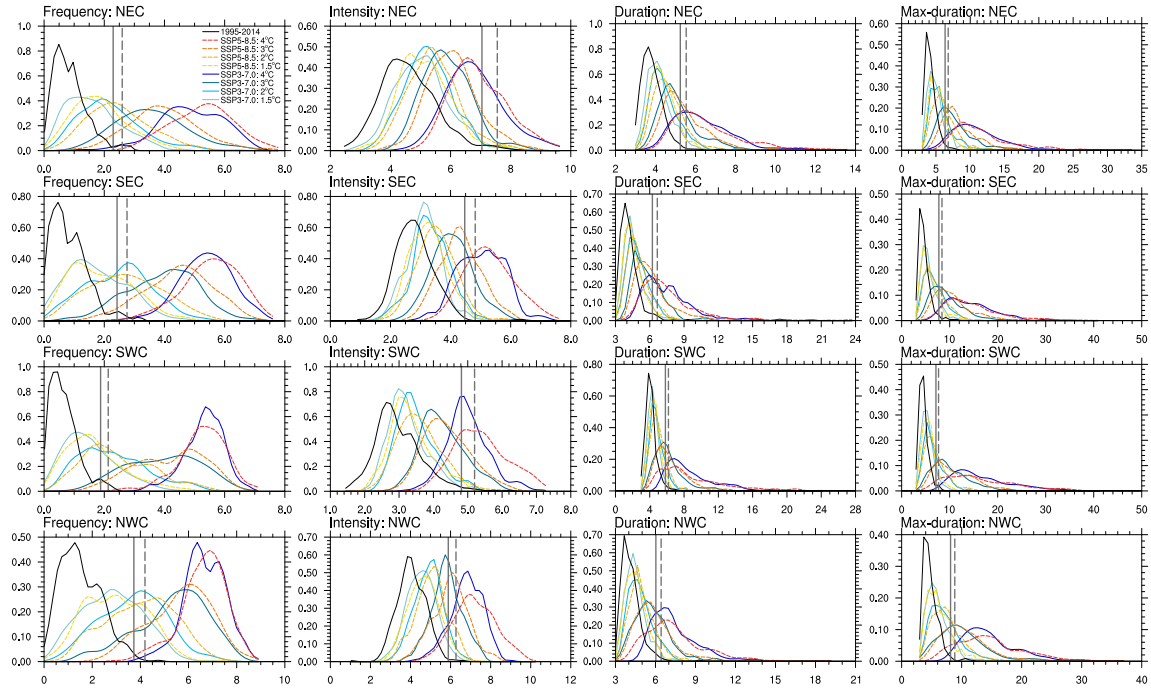

Figure 3.19 The Kernel smoothing probability density functions (PDFs) of frequency (events a^{-1}), intensity (°C), duration and max-duration (days) of Compound HWs over the four subregions in the recent climate (black), 1.5 °C, 2 °C, 3°C and 4°C GWLs. Solid (Dashed) lines represent the SSP 3-7.0 (SSP5-8.5). Grey solid (dashed) line represents the threshold of a 50-year (100-year) event based on the recent climate of 1995-2014.

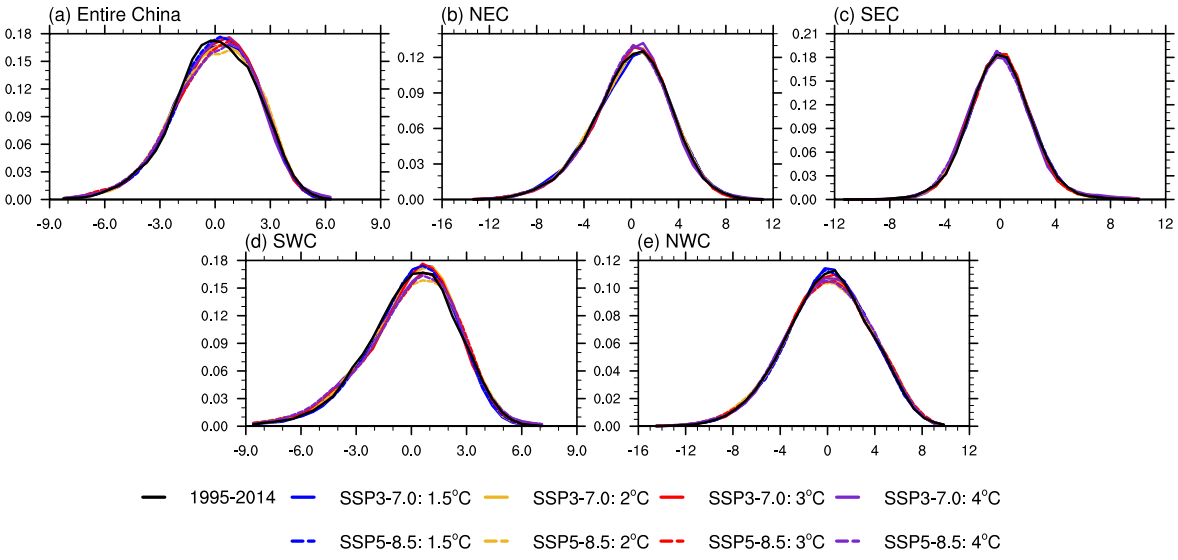

Figure 3.20 The Kernel probability density functions of daily Tmax anomalies at different GWLs over the entire China and the four subregions with the same number of model members at the four GWLs under the two scenarios. Anomalies are calculated with corresponding mean Tmax removed in each GWL.

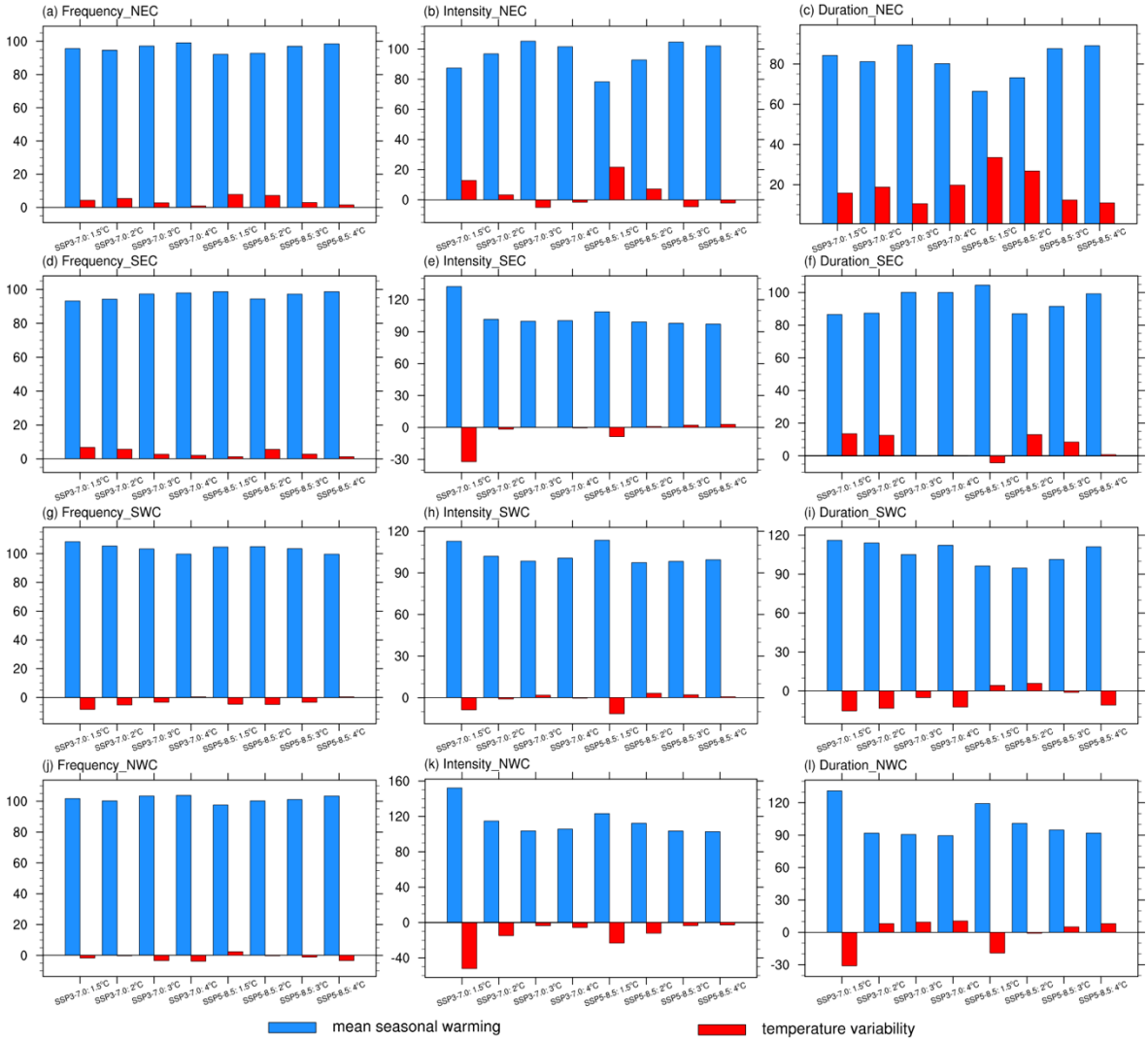

Figure 3.21 The contributions of seasonal mean warming (blue bar) and changes in temperature variability (red bar) to the future changes of frequency, intensity and duration of Compound HWs averaged over the four subregions at different GWLs (units: %).

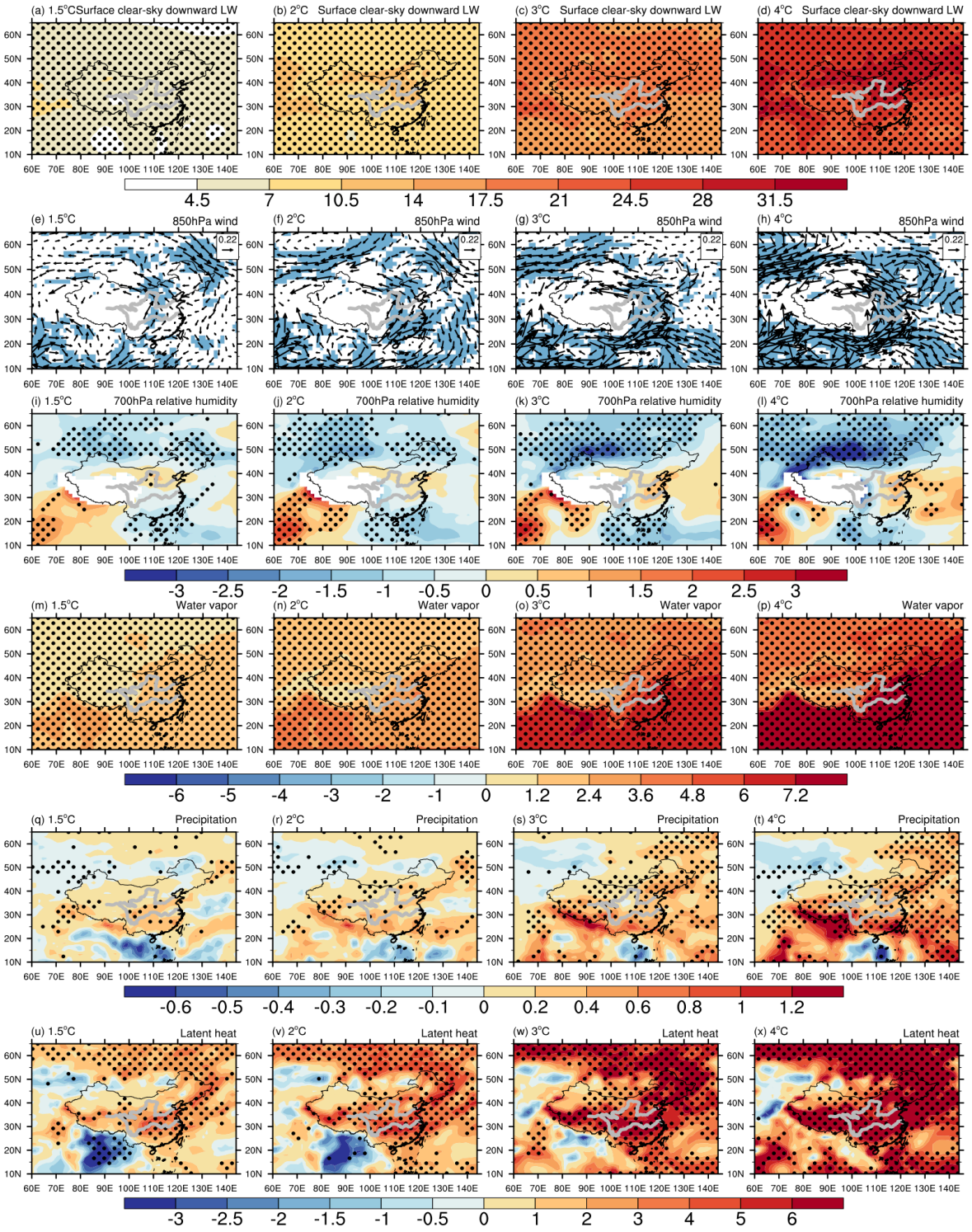

Figure 3.22 Spatial distributions of the changes in surface clear-sky downward longwave radiation (a-d, units: $W \cdot m^{-2}$), 850hPa wind (e-h, vector, units: $m \cdot s^{-1}$), 700hPa relative humidity (i-l, units: %), vertically integrated water vapor through the atmospheric column (m-p, units: $kg \cdot m^{-2}$), precipitation (q-t, units: $mm \cdot day^{-1}$), and latent heat (u-x, units: $W \cdot m^{-2}$, positive values mean upward) at 1.5℃ (2°C; 3°C; 4°C) GWL under the SSP3-7.0 relative to the recent climate. Shading in e-h and dots in a-d; i-x denote regions where at least 7 out of the 9 models agree in the sign of changes.

Chapter 4

The model uncertainty of Compound heatwave projections over China

4.1 Introduction

As the global mean surface temperature (GMST) increases under different future forcing scenarios, it is expected that there will be an increase of warm extremes over China (Zhou et al., 2014; Hu and Sun, 2020; Chen and Dong, 2021). Wang et al. (2020) show that Compound HWs, with both high day and night temperatures, will be the most frequent type of heatwave that populations are exposed to after 2030 in the Northern Hemisphere. However, a very limited number of studies have discussed the future changes of Compound HWs over China and they mainly focused on future projections of Compound HWs during some fixed future time periods (Su and Dong, 2019b; Xie et al., 2022).

In the recent years, due to the goal set in the Paris Agreement (UNFCCC, 2015), future projections based on target global warming levels (GWLs) are becoming being more frequent to be discussed more frequently. By the end of the 21st century, the likely range of GMST increase is 2.0-4.9°C with a median of 3.2°C (Raftery et al., 2017). However, the temperature related impacts of higher warming scenarios GWLs (e.g., of 3°C and above) are less emphasized in the IPCC AR6 (Jehn et al., 2021; 2022). Hence, it is necessary to focus on the future changes at the target GWLs of 1.5°C, 2°C, 3°C and 4°C to assist the government in making policy decisions and mitigating the risks associated with these hot extremes.

Projections of future climate change are uncertain, and model uncertainty is one of the key sources of this projection uncertainty (Hawkins and Sutton, 2009; Lehner et al., 2020). Even where there is a general agreement among the models on the projected sign of climate changes due to global warming, the magnitude of the change can vary widely (John et al., 2022). For future projections of summer HWs over China, most studies show multi-model mean results and have not assessed the model uncertainty in the climate projections (e.g.

Zhou et al., 2014; Hu and Sun, 2020). Therefore, the model uncertainty in the projected summer Compound HWs over China at different GWLs is worthy to be investigated. In Chapter 3, it can be seen that there is a large spread of future projections in Compound HWs properties over China among the nine models (Fig. 3.5). Hence, this chapter will focus on **the second part of the third scientific question**:

iii) What is the model uncertainty in the future projections of summer HWs over China and what are the associated physical processes?

This chapter will determine two groups of models with high and low future change, and discuss the differences in future changes of summer Compound HWs properties between the two groups. To increase the number of model sample, 24 models are included in the analysis in this chapter. Section 4.2 introduces the data and methods used. Section 4.3 shows the differences in future changes of Compound HWs properties between the high-model group and low-model group and the related physical processes are shown in Section 4.4. The conclusions and discussions are summarized in Section 4.5.

4.2 Data and Methods

4.2.1 Data

This chapter uses the historical simulations and future projections from CMIP6 (Eyring et al., 2016). The historical simulations cover the period 1850-2014 and the future projections cover the period 2015-2100. The models used are listed in Table 4.1. In the third chapter, we focused on the future projections of Compound HWs under the SSP3-7.0 and SSP5-8.5. However, only 6 models (14 members) reach the 4°C GWL by the end of the 21st century under the SSP3-7.0. Therefore, this chapter will just analyze the model uncertainty under the SSP5-8.5 which represents the highest forcing pathway with a radiative forcing of 8.5 $W \cdot m^{-2}$ in 2100 (O'Neill et al., 2016).

Table 4. 1 The list of models used in chapter 4

	Model	Resolution (lon x lat)	Members
1	BCC-CSM2-MR	320x160	1
2	FGOALS-g3	180x80	1
3	CNRM-CM6-1	256x128	1
4	ACCESS-ESM1-5	192x144	3
5	ACCESS-CM2	192x144	3
6	MIROC6	256x128	3
7	IPSL-CM6A-LR	144x143	1
8	MRI-ESM2-0	320x160	5
9	NorESM2-LM	144x96	1
10	AWI-CM-1-1-MR	384x192	1
11	CNRM-ESM2-1	256x128	1
12	MPI-ESM1-2-HR	384x192	2
13	INM-CM5-0	180x120	1
14	KIOST-ESM	192x96	1
15	MIROC-ES2L	128x64	1
16	GFDL-ESM4	288x180	1
17	EC-Earth3	256x512	2
18	UKESM1-0-LL	192x144	4
19	KACE-1-0-G	192x144	3
20	TaiESM1	288x192	1
21	CMCC-ESM2	288x192	1
22	EC-Earth3-Veg	512x256	2
23	GFDL-CM4	288x180	1
24	INM-CM4-8	180x120	1

In order to calculate the spatial multi-model ensemble mean, bilinear interpolation method is used to regrid the model outputs to a common 1.5° × 1.5° grid. The ensemble members of historical simulations and future projections in each model are the same. The HW properties of each ensemble member are calculated individually. To treat each model equally, the multi-member mean is calculated in each model first and then the multi-model ensemble mean is derived from all models.

As in previous chapters, the analysis of models is focused on the changes over the entire China and four subregions (Fig. 3.1) based on the topography and regional climate over China (Song et al., 2011). The four subregions are Northeast and North China (NEC; 35°-54°N, 105°-134.5°E), Southeast China (SEC; 21°-35°N, 105°-123°E), Southwest China (SWC; 21°-37°N, 73°-105°E) and Northwest China (NWC; 37°-50°N, 73°-105°E). Figure 4.1 exhibits the probability density functions (PDFs) of the future changes of HWs properties

over China between the different GWLs and the recent climate. The future projections of the three HWs properties still show large model spread with these 24 models, similar to the previous results in Chapter 3 by using 9 models.

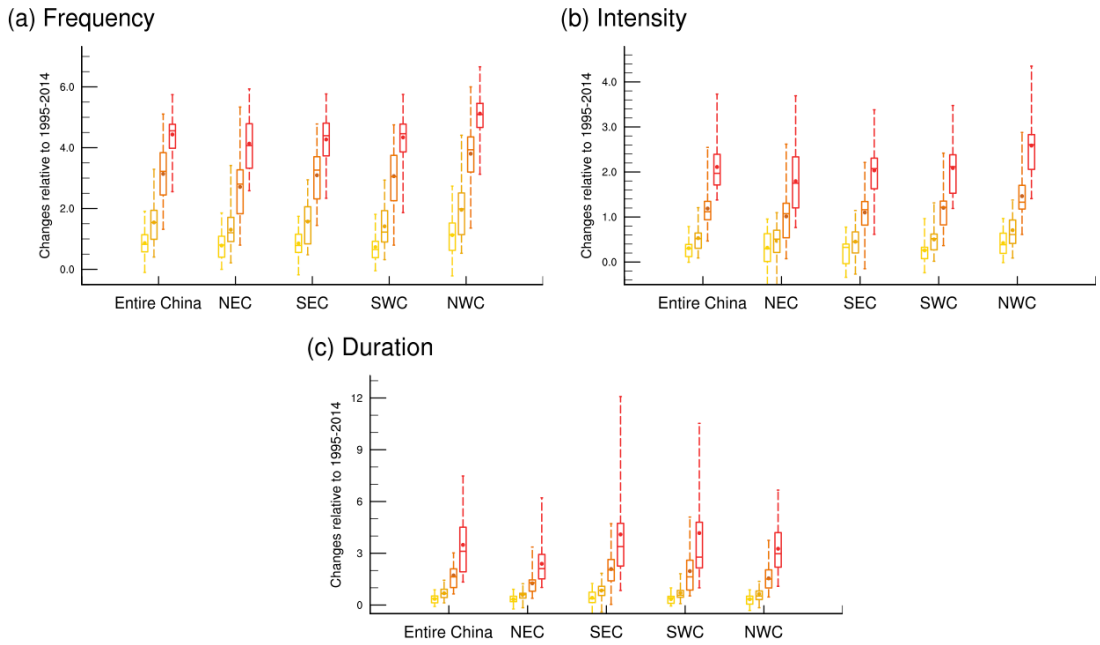

Figure 4.1 Box plots of the regionally averaged changes in the frequency (a, units: events·a-1), intensity (b, units: °C) and duration (c, units: days) of Compound HWs at 1.5°C, 2°C, 3°C, 4°C GWL (yellow-to-red colours) relative to the recent climate (1995-2014) under SSP5-8.5 scenario over the entire China and subregions. The box-and-whiskers show the spread of the model results with the horizontal lines from top to bottom denote the maximum value, the 75th percentile, the median value, the 25th percentile and the minimum value of the 24 models. The dot represents the multi-model ensemble mean whose sign agrees with at least 18 out of the 24 models.

4.2.2 Methods

a. Definition of HWs

In order to define Compound HWs, a relative threshold on each calendar day is calculated as the daily 90th percentile of Tmax or Tmin based on 15-day window centered on that day during the baseline period of 1961–1990 (Della-Marta et al., 2007). Compound HWs are identified when the daily Tmax and Tmin exceed the baseline 90th percentile for at least three consecutive days. Three features, that is frequency, intensity and duration, are used to characterize Compound HWs. The definitions of these three properties are the same as the ones in Chapter 3 (not shown here).

b. Time windows of the 1.5℃, 2℃, 3℃ and 4℃ global warming levels

According to the IPCC AR6 report (Lee et al., 2021), 1850-1900 and 1995-2014 are defined as the pre-industrial period and the recent climate period, respectively. The global warming levels refer to the GMST under the SSP5-8.5 which is 1.5°C, 2°C, 3°C and 4°C higher than the GMST during the pre-industrial period. To reduce the uncertainty in calculating the warming threshold-crossing times due to interannual internal variability, a 20-year running average is used to smooth the GMST time series (Liu et al., 2020). A 20-year window, which has 10 years before and 9 years after the year that exceeds the four global warming thresholds, is used to obtain relatively stable estimates of future climate states at different GWLs. The time window of each GWLs is determined separately for each member and each CMIP6 model. Figure 4.2 shows the GMST anomalies relative to the pre-industrial period. All members can reach 4°C GWL under SSP5-8.5 by the end of the 21st century. The differences of HW properties between different GWLs and the recent climate are regarded as the future changes of HWs (Domeisen et al., 2023).

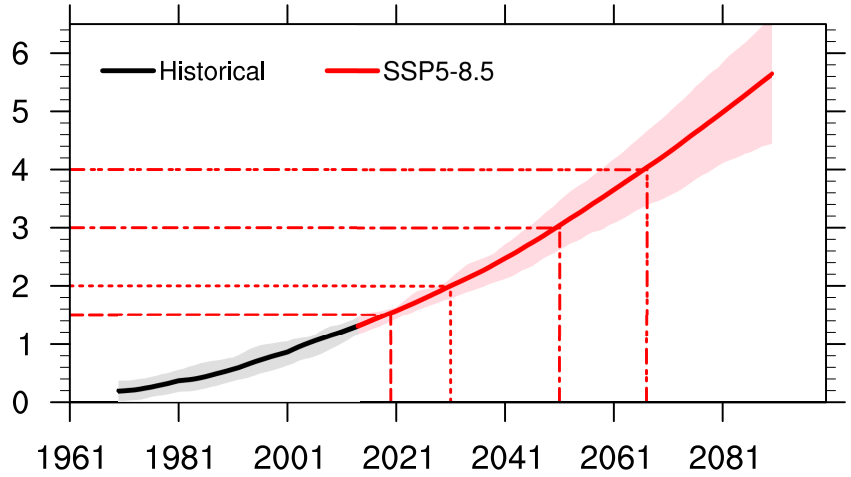

Figure 4.2 Time series of 20-year moving global mean surface temperature anomalies (relative to 1850-1900 pre-industrial period) from CMIP6 models. Black line is historical simulations and red line represent SSP5-8.5 scenario. Solid lines indicate the multi-model ensemble mean, and shading the interquartile ranges from the sample of 24 models. Vertical dashed lines indicate the calendar year for the multi-model ensemble mean to reach 1.5°C, 2°C, 3°C and 4°C GWLs.

c. Grouping of models

In Chapter 3, it is shown that the seasonal mean warming dominates the changes in HW properties at the different GWLs over China (Zhang et al., 2024c). Therefore, to discuss the differences in projected changes of HWs, this chapter considers not only the HW properties

changes, but also the summer mean temperature changes. Figure 4.3 shows the relationship of these two changes averaged over China at different GWLs in each model. There is an obvious spread among the 24 models. The median values (black dashed lines) for the changes in different HWs properties and summer mean temperature among the 24 models are used to characterize models into whether the simulated regional changes are relatively large or small. Additionally, models that have values within the median value ± 0.1 times standard deviation are rejected to avoid the models where the changes are close to the median values. Therefore, the models located within the red and blue shaded regions are defined as having regional changes in both HWs properties and summer mean temperature that are considered to be large or small among all 24 models respectively.

The models are selected to ensure that a consistent set is used across all HW properties by picking those that fall into either category often. In other words, models can appear in either the red and blue shaded regions up to 12 times, i.e. in each of the panels of Fig. 4.3, and the final subselection for each group will focus on those that do so the most often. Figure 4.4 shows the frequency of each model appearing over these two shaded regions in the three HW properties at the four GWLs. When this frequency is greater than three models are defined as either a regional high-change models or regional low-change models, respectively (hereafter as ‘high-model’ or ‘low-model’). Table 4.2 shows the 9 high-model and 11 low-model groups. Four models remain unclassified.

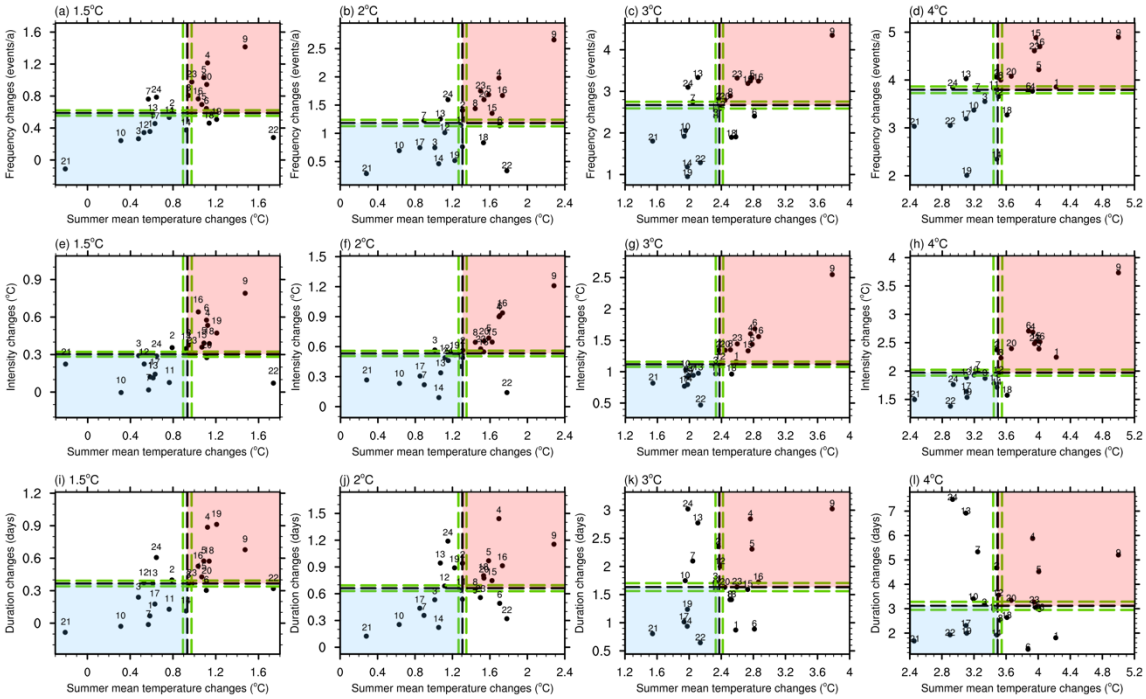

Figure 4.3 Scatter plots of summer mean temperature changes and HW properties changes averaged over the entire China of the 24 models at the 1.5°C, 2°C, 3°C and 4°C GWLs. X-axis is summer mean temperature changes (units: °C). Y-axis is frequency changes (a-d, units: events·a^{-1}), intensity changes (e-h, units: °C) and duration changes (i-l, units: days). The summer mean changes are relative to the recent climate period 1995-2014. The numbers represent the names of model shown in Table 4.1. The red (blue) shaded regions are the area where the high-model (low-model) group is largely located. The black dashed lines are the median values of the frequency changes and summer mean temperature changes among the 24 models. The green dashed lines are the median values plus or minus the 0.1 times standard deviation.

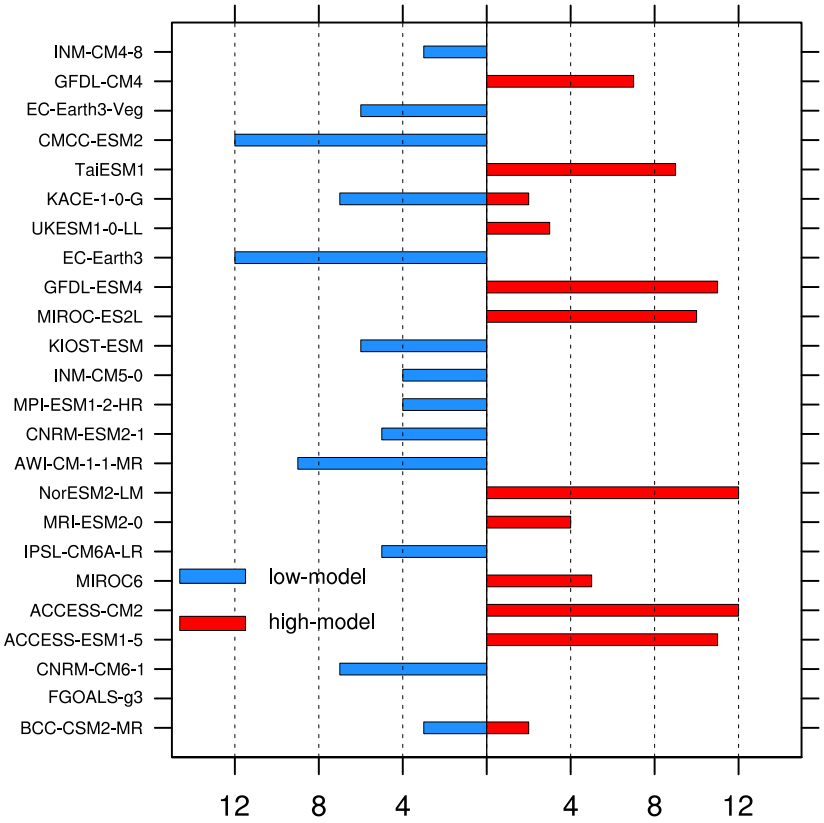

Figure 4.4 The frequency of each model in the red and blue shaded regions in Fig. 4.3.

Table 4.2 The list of models in the high-model groups, low-model groups and unclassified models.

High-model (9)	Low-model (11)	Unclassified models (4)
ACCESS-ESM1-5; ACCESS-CM2; NorESM2-LM; MIROC6; MIROC-ES2L; GFDL-ESM4; MRI-ESM2-0; TaiESM1; GFDL-CM4	CNRM-CM6-1; IPSL-CM6A-LR; AWI-CM-1-1-MR; CNRM-ESM2-1; MPI-ESM1-2-HR; INM-CM5-0; KIOST-ESM; EC-Earth3; KACE-1-0-G; CMCC-ESM2; EC-Earth3-Veg	INM-CM4-8; UKESM1-0-LL; FGOALS-g3; BCC-CSM2-MR

4.3 The differences in the change of HW properties between high-model and low-model groups

The performance of the multi-model ensemble mean in simulating the historical Compound HWs properties is shown in Section 4.5 (Appendix). The performance in simulating temperature and HWs is consistent with that obtained using fewer models in Chapter 3. Although the biases might affect the model simulated HWs over the western

China, the models can capture the main features of observed trends of HWs during the historical period, giving the fidelity using such models to assess future changes.

Figure 4.5 shows the future changes of frequency, intensity and duration of the Compound HWs at different GWLs in both the high-model and low-model groups. The differences between the two groups is shown in Fig. 4.6. The spatial patterns of the future changes of the three properties are similar between the two groups of models with high pattern correlation coefficients. For frequency, the future changes in both groups are significant across China at the four GWLs with the largest changes appearing over the Northwest China (Fig. 4.5). The differences between the two model groups are significant over most regions of China (Fig. 4.6a-d) although the magnitudes of the future changes of high-model group are larger than the ones of low-model group across China. The maximum difference occurs over the Northeast China with a value of 1.34 (1.80; 2.27) events·a^{-1} at the 1.5℃ (2℃; 3℃) GWL. At the 4℃ GWL, the differences over the eastern China are larger than the western China and the largest difference appears over the Southeast China with a value of 2.21events·a^{-1}.

The future changes in intensity of high-model group show significant increase all around China at the four GWLs, while the changes of low-model group are only significant over the Northwest China and the regions along the Yangtze River at the 1.5℃ and 2℃ GWLs (Fig. 4.5). Except the western part of the Tibetan Plateau, the future changes of high-model group are larger than low-model group at the four GWLs (Fig .4.6e-h). The significant regions expand with the increasing GWLs. At the 1.5℃ and 2℃ GWLs, the largest difference appears over the Southeast China with a value of 1.41°C and 1.20°C. The Northeast China exhibits the maximum difference with a value of 1.54°C and 1.87°C at the 3℃ and 4℃ GWLs, respectively.

At the 1.5℃ and 2℃ GWLs, the future changes in duration of low-model group are not as obvious as the ones of the high-model group (Fig. 4.5). The differences in the changes of duration between high-model and low-model groups are small with a value of less than 1 day (Fig. 4.i-j). At the 3℃ and 4℃ GWLs, both model groups show significant increase of duration across China (Fig. 4.5), while the differences between the high-model and low-

model groups are only significant over the Northeast China with a maximum value of 17.1 days and 22.6 days (Fig. 4.6k-l).

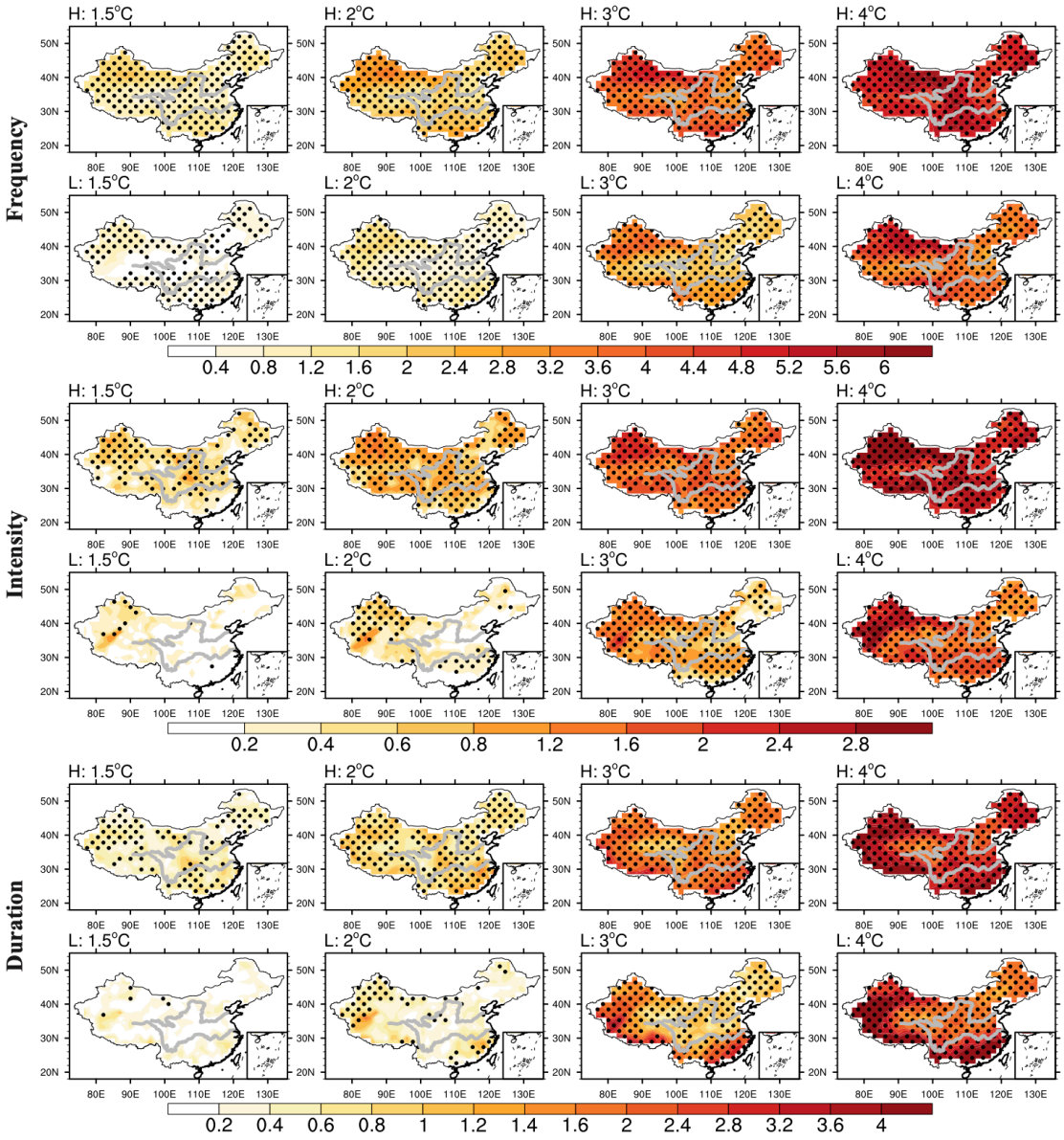

Figure 4.5 The spatial distributions of Compound HWs frequency changes (units: events·a^{-1}), intensity changes (units: °C) and duration changes (units: days) in high-model and low-model groups at the 1.5°C, 2°C, 3°C and 4°C GWLs. The changes are relative to the recent climate period 1995-2014. Dots denote regions where at least 75% of the models agree on the sign of changes.

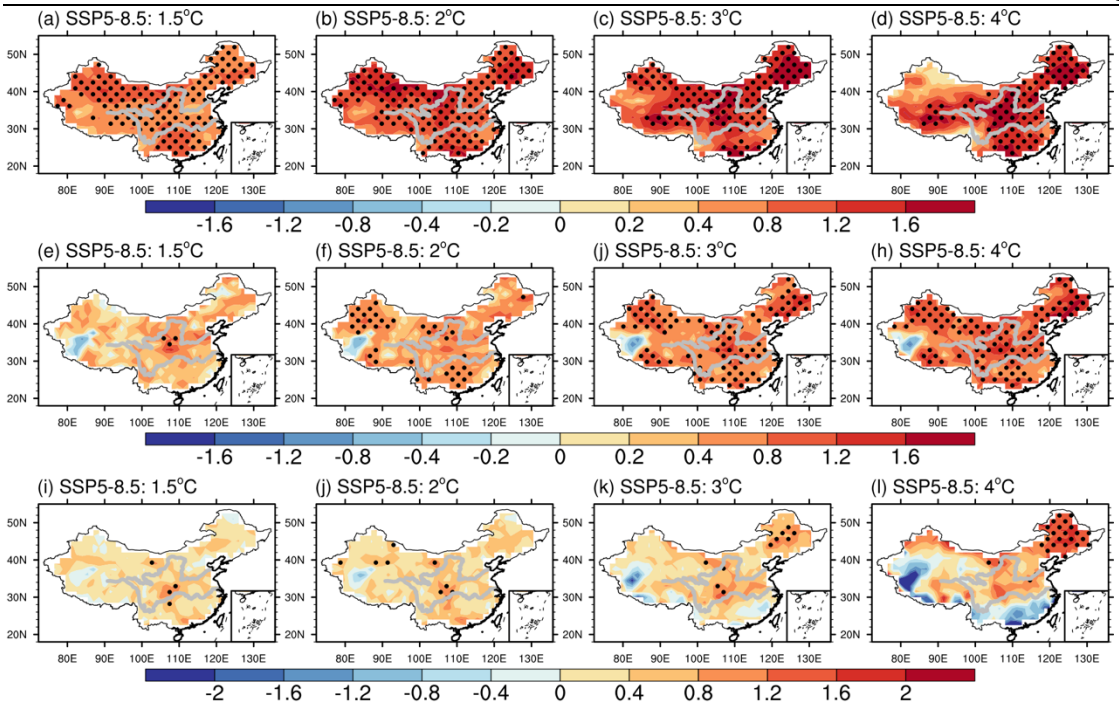

Figure 4.6 The spatial distributions of differences in Compound HWs frequency changes (a-d, units: events·a^{-1}), intensity changes (e-h, units: °C) and duration changes (i-l, units: days) in summer between high-model and low-model groups at the 1.5°C, 2°C, 3°C and 4°C GWLs. The changes are relative to the recent climate period 1995-2014. The dotted regions are the areas where passed the t-test at 0.1 level.

The regionally averaged differences in the future changes of HW properties between the high-model and low-model group over the entire China and the four subregions are shown in Fig. 4.7. The regional averaged differences in frequency over the entire China of high-model group are 0.74 (1.14; 1.26; 1.12) events·a^{-1} larger than low-model group at the 1.5℃ (2℃; 3℃; 4℃) GWL (Fig. 4.7a). The largest regional averaged differences in frequency at the 1.5℃ and 2℃ GWLs appear over NWC with a value of 0.94 events·a^{-1} and 1.37 events·a^{-1}, respectively. At the 3℃ and 4℃ GWLs, the differences over NEC are larger than the other subregions. In terms of intensity, the regional averaged differences increase with the increasing GWLs over the entire China and the four subregions (Fig. 4.7b). NEC shows the largest regional averaged differences at the four GWLs (0.41℃; 0.58℃; 0.87℃; 1.15℃). The smallest regional averaged differences appear over SWC. The magnitudes of the regional averaged differences in duration over the entire China are similar at the four GWLs (Fig. 4.7c). Only NEC shows significant regional differences at the four GWLs. Over NEC, the future changes in duration of high-model group last longer than low-model group,

and differences increase with GWL with values of 0.27 days, 0.43 days, 0.75 days and 1.37 days at the 1.5℃, 2℃, 3℃ and 4℃ GWL.

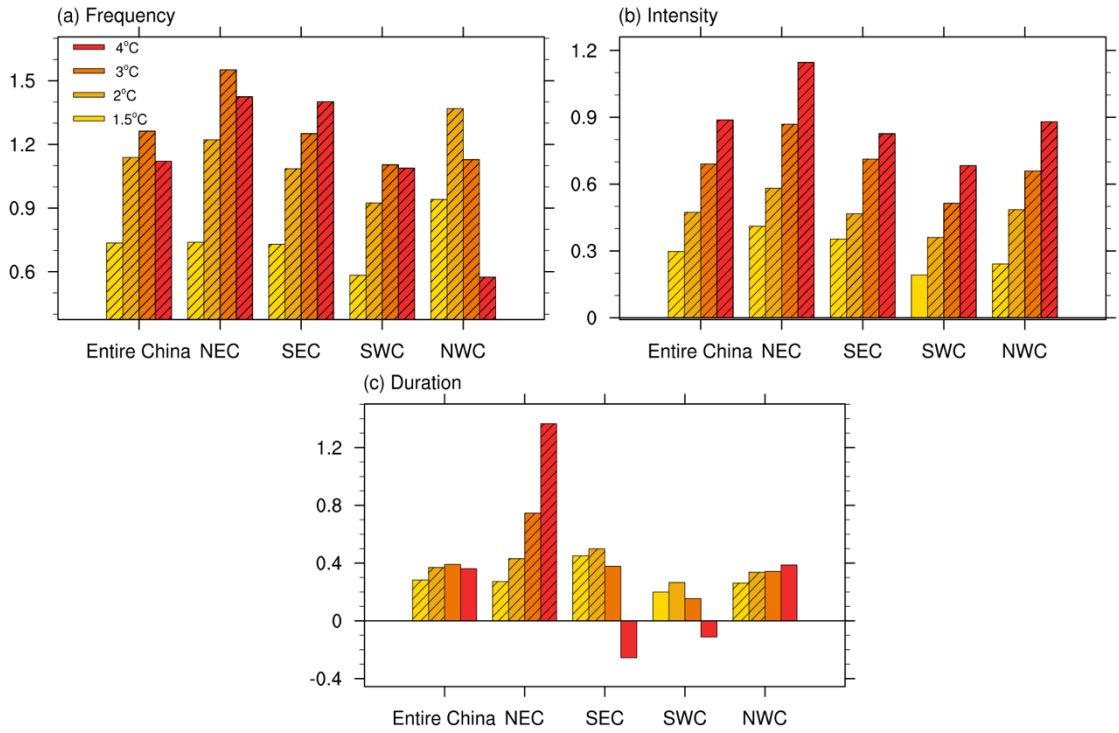

Figure 4.7 Bar plot of the regional averaged differences of the future changes in Compound HW frequency (a, units: events·a^{-1}), intensity (b, units: °C) and duration (c, units: days) between high-model and low-model groups over the entire China and the subregions. The shaded regions are the areas where passed the t-test at 0.1 level.

To analyze the sensitivity of the future changes in HWs properties on the model groups, Fig. 4.8 illustrates the percentage changes of high-model group relative to the low-model group. The percentage changes in these three properties decrease with the increasing GWLs at the entire China and the four subregions, suggesting a slow increasing pace of HW property with GWLs in the high-model group than that in the low model group, which means the model uncertainty becomes relatively less important at higher GWLs. The percentage changes over the eastern China are larger than the western China and NEC shows the largest percentage changes among the subregions.

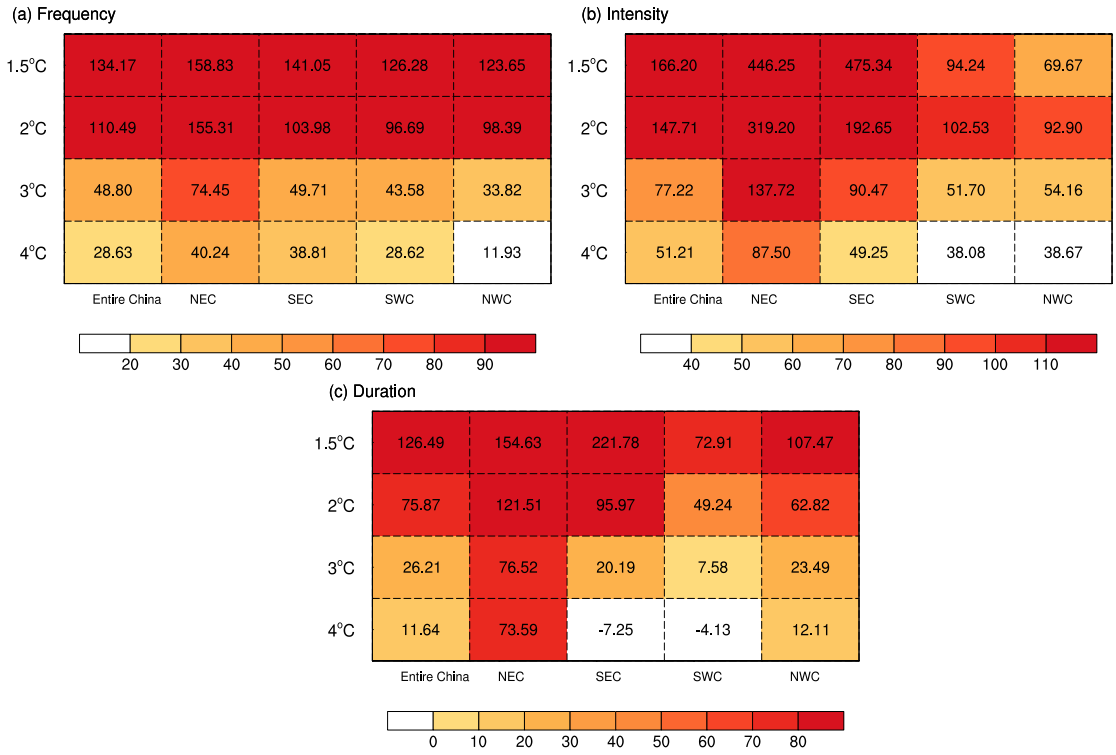

Figure 4.8 The percentage changes in Compound HWs frequency (a), intensity (b) and duration (c) between high-model and low-model groups relative to the low-model group over the entire China and the subregions (units: %). The percentage change is calculated as $\frac{(H-L)}{L} \times 100\%$.

In summary, although the spatial patterns of the changes in HW properties are generally similar, there are significant differences between warm and cool models. In terms of the regional averaged differences for future changes, there are obvious regional variations among the subregions. The sensitivity of the future changes in HWs properties on the model groups becomes weaker with the increasing GWLs.

4.4 The physical processes responsible for the differences between the high-model and low-model groups

According to Chapter 3, the future changes of HWs are mainly controlled by the seasonal mean warming and the responsible physical processes can be investigated by analyzing the changes of physical variables in climatological seasonal mean state. Figure 4.9 and Figure 4.10 shows seasonal mean changes in some key variables of low-model group at different GWLs relative to the recent climate.

Figure 4.9 shows that the surface clear-sky downward longwave radiation increases significantly over China (Fig. 4.9a-d), which contributes to the increases of temperature (Fig.

4.9e-h). The warmer temperature across China is associated with the future increases of Compound HWs properties, especially over the Northwest China where the intensity increases much more than the other regions (Fig. 4.5). The increases of surface clear-sky downward longwave radiation are likely to be partly due to the increase in greenhouse gas forcing and partly due to the increase of water vapor in the atmosphere related to warming (Fig. 4.9i-l). Considering the processes related to changes of aerosol forcing, the aerosol optical depth (AOD) at 550nm decreases significantly over the eastern China (Fig. 4.10a-d). Influenced by aerosol-radiation interactions (Hatzianastassiou et al., 2007, Boucher et al., 2013), the decrease of AOD at 550nm results in the increase of net surface clear-sky shortwave radiation (Fig. 4.10e-h), which will tend to warm the surface over the eastern China. Cloud cover changes show decreases in mid-latitudes over Asia and eastern China (Fig. 4.10i-l). The decreases in mid-latitudes over Asia are presumably induced by decreases in relative humidity (not shown), which under the global warming scenario is attributed to that water vapor in the atmosphere over land is controlled mainly by transport from the ocean and constrained by ocean warming and increases less than saturation specific humidity following the Clausius-Clapeyron relationship because of stronger warming over land than over the ocean (e.g., Dong et al., 2009; Boé and Terray, 2014) since aerosol emission changes are weak. The decreases in total cloud cover over eastern China are presumably induced by aerosol-cloud interactions (Boucher et al. 2013). Associated with the decreases in total cloud cover (Fig. 4.10i-l), the net surface shortwave radiation shows significant increases over the eastern China (Fig. 4.10m-p). The increases of net surface shortwave radiation also contribute to the surface warming. Thus, the physical processes are similar to the ones with less models in Chapter 3. High-model group also has similar physical mechanism related with the future changes of Compound HWs, therefore, the processes of high-model are not shown here.

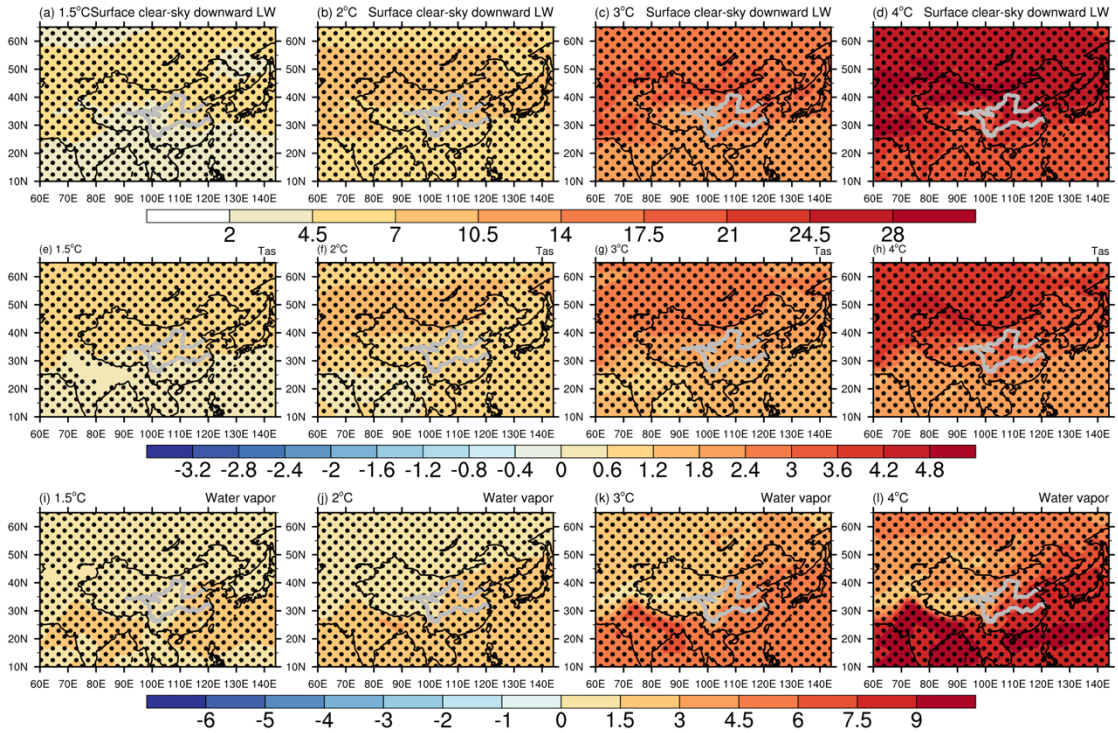

Figure 4.9 Spatial distributions of the summer mean changes for the low-model group in surface clear-sky downward longwave radiation (a-d, units: $W \cdot m^{-2}$) surface air temperature (e-h, units: ℃) and vertically integrated water vapor through the atmospheric column (i-l, units: $kg \cdot m^{-2}$), at 1.5℃ (2°C; 3°C; 4°C) GWL under the SSP5-8.5 relative to the recent climate (1995-2014). Stippling denotes regions where at least 8 out of the 11 models agree in the sign of changes.

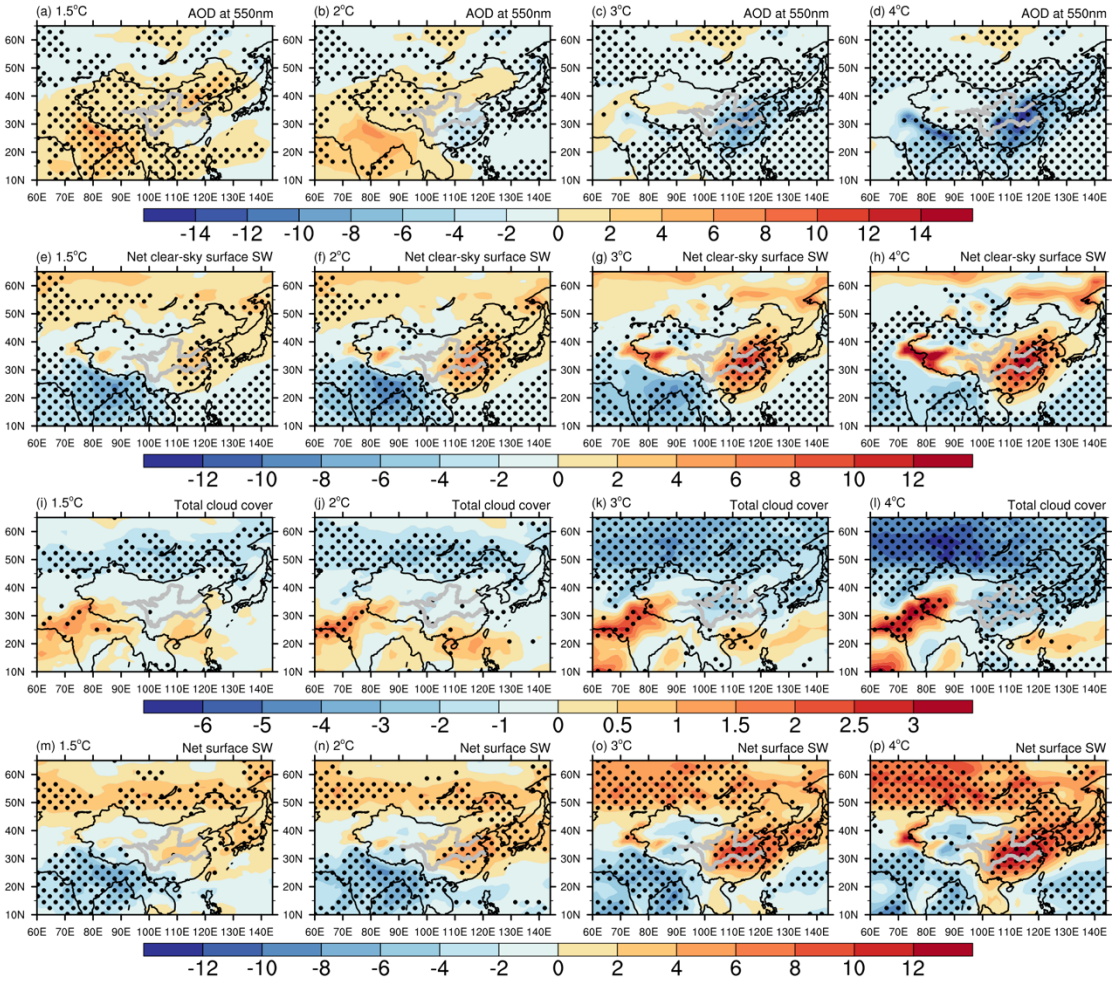

Figure 4.10 Spatial distributions of the summer mean changes for the low-model group in aerosol optical depth (AOD) at 550nm (a-d, units: 10^{-3}, results are based on 7 models in which AOD is available), net clear-sky surface shortwave radiation (e-h, units: $W \cdot m^{-2}$), total cloud cover (i-l, units: %) and net surface shortwave radiation (m-p, units: $W \cdot m^{-2}$) at 1.5℃ (2°C; 3°C; 4°C) GWL under the SSP5-8.5 relative to the recent climate. Dots denote regions where at least 8 out of the 11 models agree in the sign of changes, but only 5 out of 7 models in AOD.

Figure 4.11 shows the differences in some physical variables for future changes between the high-model and low-model groups. The differences in surface temperature changes between the two model groups show that future summer mean warmings are larger in the high-model group compared with those in the low-model group (Figure 4.11e-h). These differences in surface air temperature changes are closely related to positive differences in the surface clear-sky downward longwave radiation and water vapor in the atmosphere (Fig. 4.11a-d, Fig. 4.11i-l). The large future summer mean warming in the high-model group contributes to the large changes of HW properties, especially over the Northeast

China. It's consistent with Fig. 4.7 that the largest differences in changes of properties are mainly appear over NEC at the four GWLs.

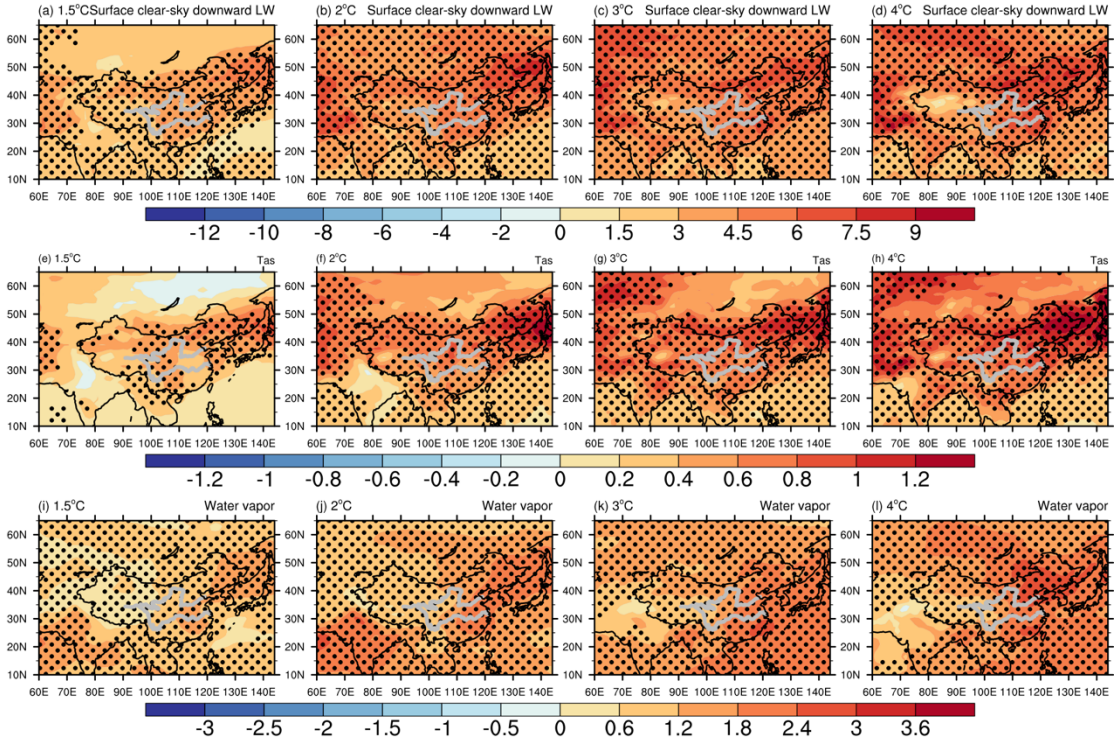

Figure 4.11 Spatial distributions of the differences in future changes in surface clear-sky downward longwave radiation (a-d, units: W·m^{-2}) surface air temperature (e-h, units: °C) and vertically integrated water vapor through the atmospheric column (i-l, units: kg·m^{-2}), at 1.5°C (2°C; 3°C; 4°C) GWL under the SSP5-8.5 between high-model and low-model groups in summer. The future changes are relative to the recent climate. Shading denotes regions where passed a Student's t-test at the 0.1 level.

The differences in variables related to shortwave radiation between high-model and low-model groups are shown in Fig. 4.12. The future changes in AOD at 550nm of high-model group decrease more than those of low-model group (Fig. 4.12a-d), which contributes to the larger increases in net clear-sky surface shortwave radiation (Fig. 4.12e-h). However, the magnitudes of the differences in net clear-sky surface shortwave radiation are small and not significant over most regions of China, especially at higher GWLs. The differences in net surface shortwave radiation of high-model group are larger over the eastern and central China (Fig. 4.12i-l), which is partly due to the larger decreases of total cloud cover (Fig. 4.12m-q). The larger differences in net surface shortwave radiation than net clear sky shortwave radiation indicate that the difference in shortwave cloud radiative effect between

high-model and low-model groups plays a role for the summer mean warming differences seen in Fig. 4.11 (e-h).

As shown in Fig. 4.8, the degree of model uncertainty diminishes at higher GWLs. This reduction may be associated with the decreasing differences in the future changes of AOD between high-model and low-model groups (Fig. 4.12 a-d), relating with the assumption that the all RCPs have a declining trend of aerosol emissions in the 21st century and the contribution of aerosol emissions to radiative forcing becomes weaken at high GWLs (Smith and Bond, 2014).

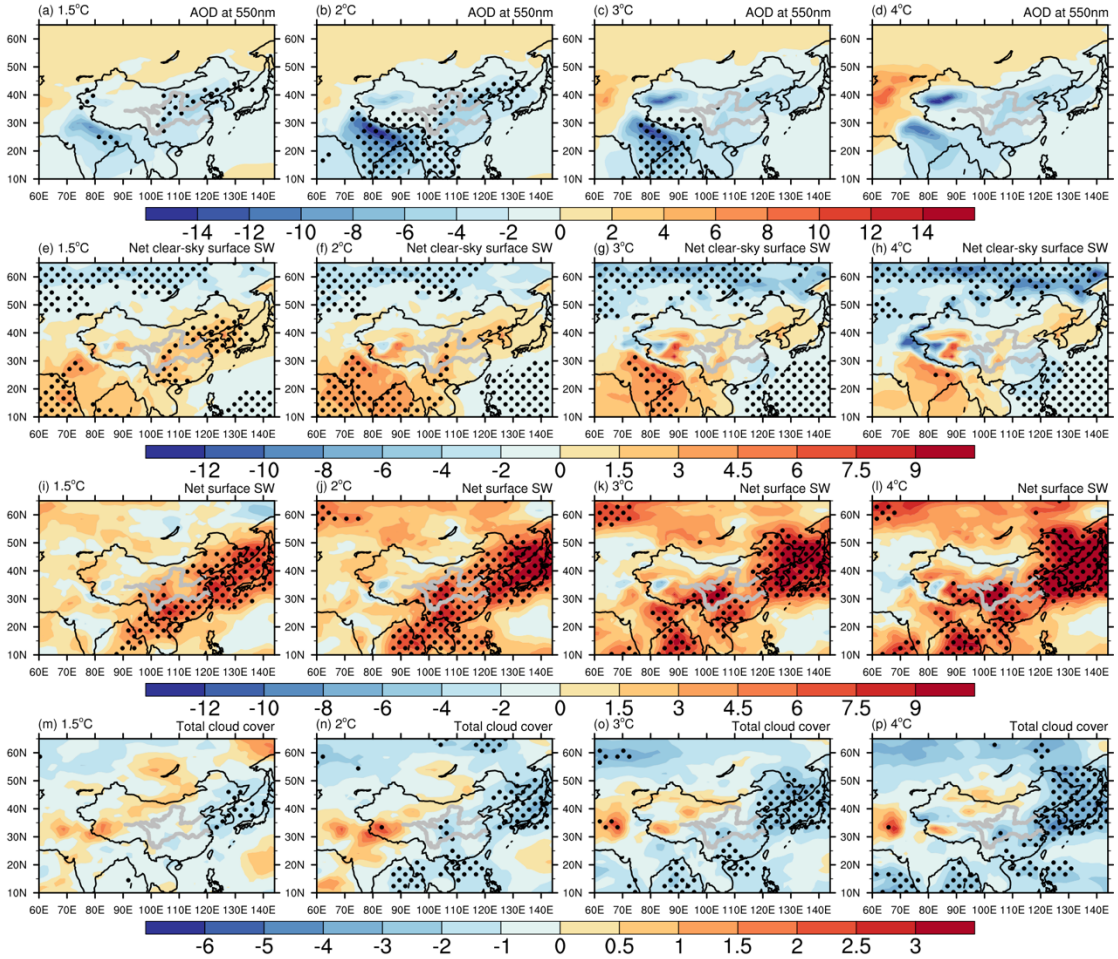

Figure 4.12 Spatial distributions of the differences in future changes in aerosol optical depth (AOD) at 550nm (a-d, units: 10^{-3}, results are based on 6 high-model and 7 low-model in which AOD is available), net clear-sky surface shortwave radiation (e-h, units: $W \cdot m^{-2}$), total cloud cover (i-l, units: %) and net surface shortwave radiation (m-p, units: $W \cdot m^{-2}$) at 1.5℃ (2°C; 3°C; 4°C) GWL under the SSP5-8.5 between high-model and low-model groups in summer. The future changes are relative to the recent climate. Shading denotes regions where passed a Student's t-test at 0.1 level.

4.5 Conclusions

As shown in Chapter 3, Compound HWs over China become more frequent, hotter, and longer at the 1.5°C, 2°C, 3°C and 4°C GWLs than those in the recent climate (1995-2014). However, there is a large spread of future projections in Compound HWs properties among the models signifying large uncertainty. By classifying the 24 CMIP6 models into high-model and low-model groups, this chapter discusses the model uncertainties of the projected changes in Compound HWs. The main conclusions can be summarized as follows.

The properties of Compound HWs in both groups increase over China relative to the recent climate. However, the magnitudes of the future changes in frequency of high-model group are larger than low-model group all over the China at the four GWLs. The differences in future changes of intensity between high-model and low-model show positive values over most regions of China. At the 4°C GWL, the differences in the projected changes of frequency, intensity and duration between the two groups can reach 2.12 events·a^{-1}, 1.87°C and 22.6 days, respectively. The influence of the model groups on the projections of HWs properties become weaker with the increasing GWLs.

There are also clear regional differences in the future changes of HWs properties between the two model groups. The largest regional averaged differences in frequency appears over NWC at the 1.5°C and 2°C GWLs and NEC at the 3°C and 4°C GWLs. NEC shows the largest regional averaged differences in the future changes of frequency at the four GWLs, while SWC exhibits the smallest regional averaged differences. In terms of duration, only NEC shows significant regional positive differences at the four GWLs.

Both model groups have similar physical processes related to the future changes of Compound HWs. Induced by increases of longwave radiation, partly resulted from increase in greenhouse gas forcing and partly resulted from increased water vapor and the increases of shortwave radiation over eastern China related to decreases in aerosols and total cloud cover, the surface air temperature becomes much warmer in the future climate. The surface warming then contributes to the increases of HWs properties.

Larger changes of HW properties in future projections at different GWLs in high model group compared with those in low model group are related to larger summer mean warming in high model group. Larger summer mean warming in high model group is associated with

larger increases of surface clear-sky downward longwave radiation over China, resulting from the larger increase of water vapor in the atmosphere in the high-model group in comparison with those in low model group. It's suggested that the water vapor in the atmosphere is an important factor for the spread of projected summer mean warming and HW property changes over China. In addition, the differences of the net surface shortwave radiation between the two model groups with large positive values over China, especially over the eastern China, related to the larger decreases of total cloud cover in high-model, also contributes to larger summer warming. It's suggested that the shortwave cloud radiative effect is also factor for difference between the two model groups leading to more severe simulated HWs in the high-model group.

This chapter points out that the differences in the projected changes of shortwave radiation are one of the factors which related with the model uncertainty of the future changes of Compound HWs. It is consistent with the previous studies that clouds and their effects have an important impact on net surface shortwave radiation (Schneider, 1972; Aumann et al., 2012; Chen et al., 2012), which is also identified as a key uncertainty in climate model (Solomon et al., 2007). Therefore, the processes for the spreads of shortwave cloud radiative effect among models in projected changes of HWs over China are still needed to be discussed in the further study.

4.6 Appendix

Figure 4.13 shows the simulated and observed summer mean Compound HWs during 1961-2014. The multi-model ensemble mean can well represent the intensity of Compound HWs well with a high pattern correlation coefficient of 0.90. However, the models still have some biases in simulating climatological spatial distributions of frequency and duration, especially over Western China. The correlation coefficient of the simulated frequency and duration is only about 0.32 and 0.10, respectively.

The observed and simulated linear trends of the properties of Compound HW during the period 1961-2014 are shown in Fig. 4.14. The multi-model ensemble mean can generally reproduce the observed trend over the entire China. The simulated trends of the three HW properties over SWC are much smaller than the observed ones, while the simulated trends

over NWC are larger than the observed ones. The large biases in simulating the spatial patterns and linear trends of the Compound HWs over the western China are related with the biases in simulating the Tmax and Tmin (Fig. 4.15). The model tends to underestimate the temperature over SWC and overestimate the temperature over NWC.

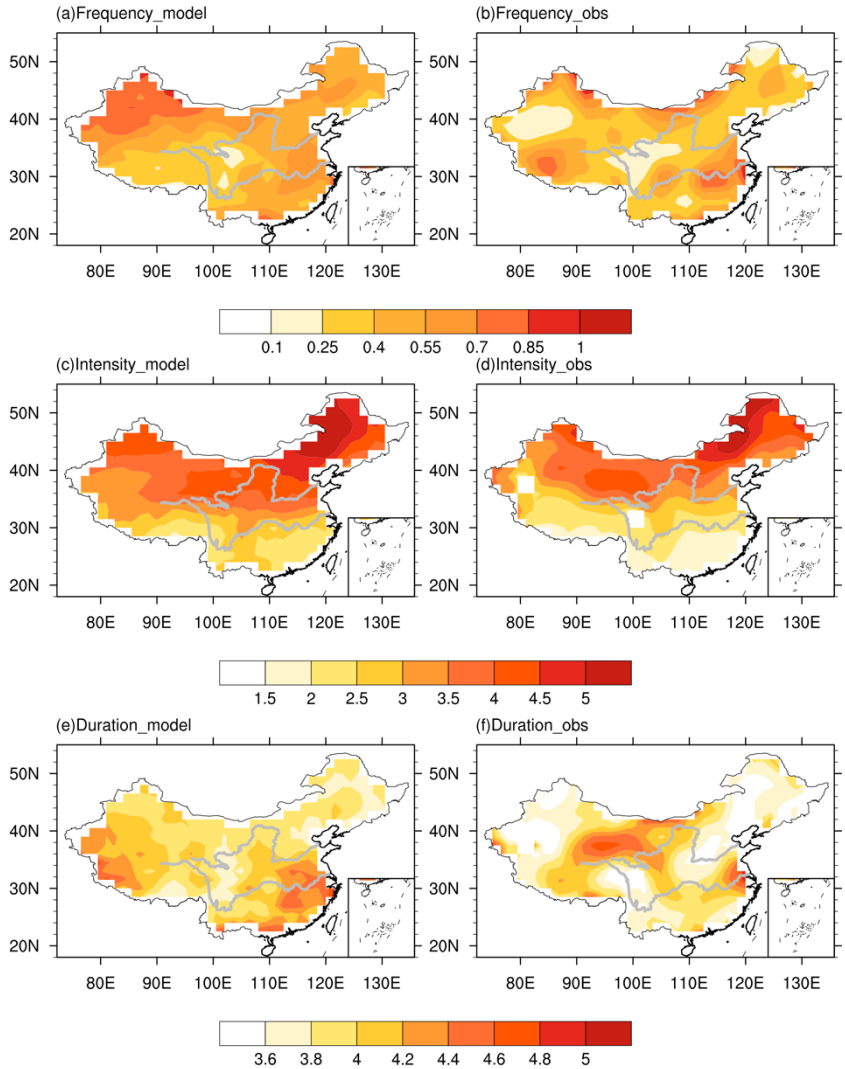

Figure 4.13 The climatological spatial patterns of Compound HW frequency (a-b, units: events·a^{-1}), intensity (c-d, units: °C) and duration (e-f, units: days) during the historical period (1961-2014) based on model simulations and observations. The observation data is derived from the gridded CN05.2 dataset.

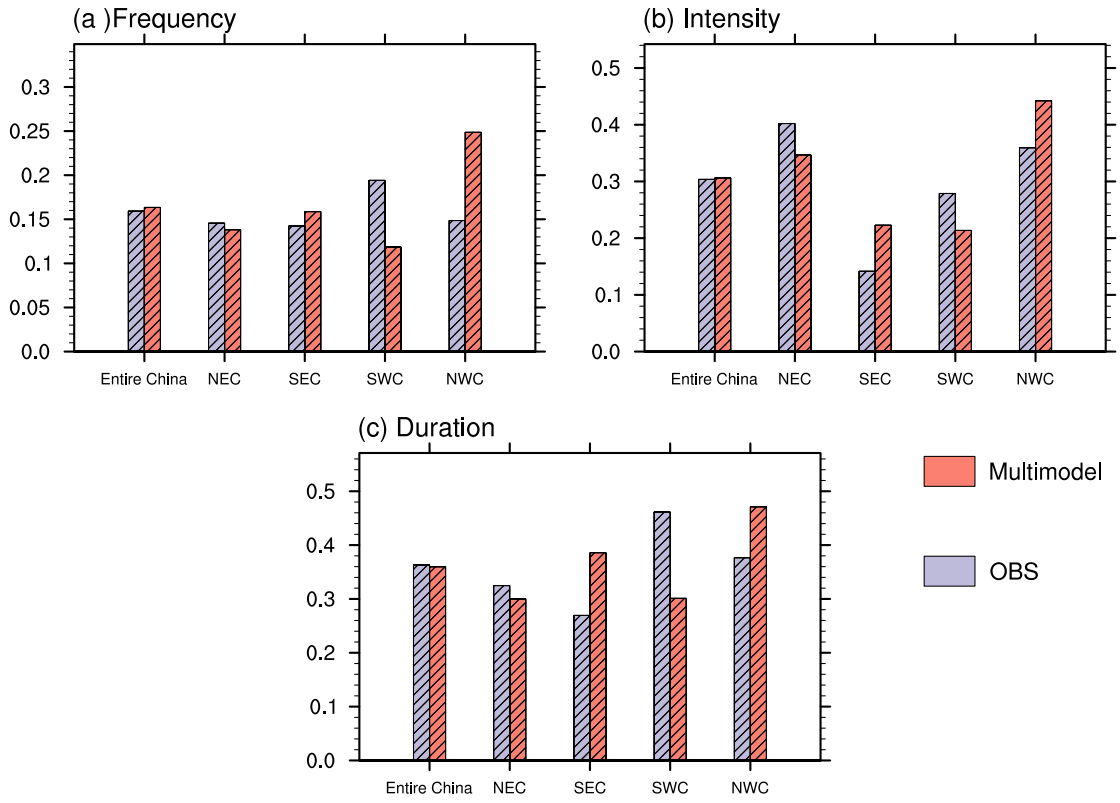

Figure 4.14 The linear trends of HWs frequency (a, units: events·10yr^{-1}), intensity (b, units: °C·10yr^{-1}) and duration (c, units: days·10yr-1) based on observation and model simulations during the period 1961-2014 over the entire and the four subregions. The hatch represents the trend is statistically significant at the 0.05 level.

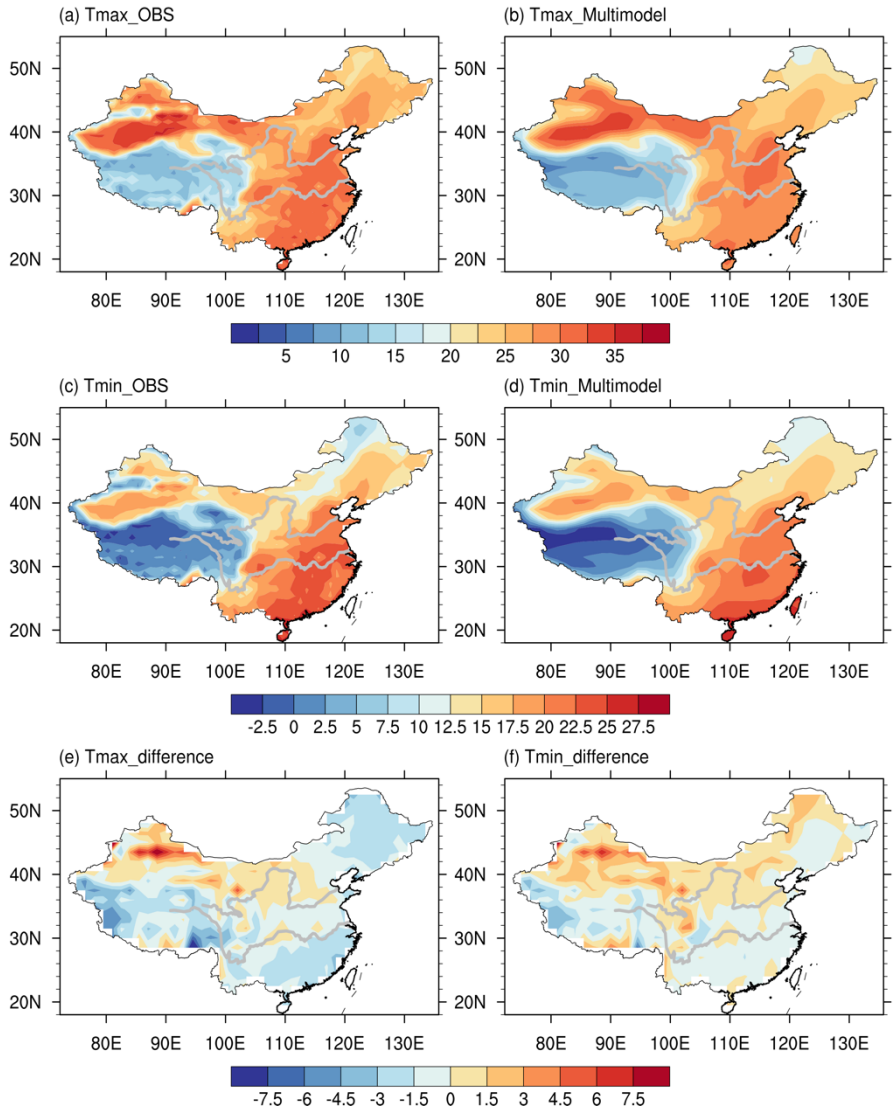

Figure 4.15 The spatial patterns of climatology in Tmax and Tmin (a-d, units: °C) during the historical climate (1961-2014) based on observations and model simulations, and the differences of Tmax and Tmin (e-f, units: °C) between model simulations and observations.

Chapter 5

Case study: the extreme heatwaves in 2022 summer over eastern China

During summer 2022, eastern China was affected by an unprecedentedly long and intense heatwave. This heatwave was especially intense over the regions from the Sichuan Basin to the middle and lower reaches of the Yangtze River valley and is the strongest regional heatwave event over China since 1961. After removing the climatological daily mean of daily Tmax, the highest 10-day running mean of Tmax anomalies in each summer is used as an index to represent this purely Daytime heatwave event.

The previous studies demonstrate that anthropogenic forcings have increased the frequency of the most extreme heatwaves around the world (Horton et al., 2015; Ma et al., 2020; Ren et al., 2020). Due to the influence of global warming, warm extremes are also expected to become more frequent over China in the future (Sun et al., 2014, Sun et al., 2018). Considering the goal set in the Paris Agreement, future projections based on target GWLs are becoming more important. Therefore, focusing on **the fourth scientific question**:

iv) How does the anthropogenic forcing influence the likelihood of the 2022 extreme HWs over the Yangtze River region? How will the likelihood of this kind of event change in the future at different global warming levels?

This chapter aims to analyze the observed characteristics of the 2022 summer heatwave event and the influence of anthropogenic forcings on the probability of the 2022-like heatwave event. The future projections of the 2022-like summer heatwave events over China at different GWLs are also discussed.

This chapter has been submitted in *Environmental Research Communications* (Zhang et al. 2025):

Zhang, M., Dong, B., Robson, J., Schiemann, R., Anthropogenic influences on 2022-like summer heatwaves over the Yangtze River valley and projected changes in the likelihood of the event. *Environ Res Commun* (2025), under review.

Abstract

During summer 2022, a record-breaking heatwave occurred over the Sichuan Basin to the middle and lower reaches of the Yangtze River valley. After removing the climatological daily mean of daily Tmax, the highest 10-day running mean of Tmax anomalies in each summer is used as an index (TXa10day) to represent this event. Observational analysis shows that the largest regional averaged TXa10day in summer 2022 appears around 17th August with an anomaly of 4.15°C relative to the baseline period (1961-1990) climatology, which is 4 times the interannual standard deviation. This event is too rare in both observations and model simulations during the historical period 1961-2022 to make robust attribution statements. Therefore, we assess anthropogenic influences and future changes of a 2022-like summer heatwave event by using the threshold of a 1-in-100-year event in observations with a TXa10day anomaly of 3.19℃. Based on the multi-model ensembles of the sixth Coupled Model Intercomparison Project (CMIP6), we find that the impacts from greenhouse gas changes overwhelm the impacts from aerosol changes, leading to an increased likelihood of the 2022-like summer heatwave event by about 3 times, which is corresponding to a change of return period from 1-in-53-year event under natural forcing to 1-in-17-year event under all forcing in the present climate (2018-2027). Climate model projections show that the 2022-like summer heatwave event will become more frequent under both SSP5-8.5 and SSP3-7.0 scenarios. The likelihood of such event increases exponentially with increasing global warming level (GWL). Such extreme event will become a 1-in-8.4-year, 1-in-5-year, 1-in-2-year and 1-in-1.3-year event under the SSP5-8.5 at the 1.5℃, 2℃, 3℃ and 4℃ GWLs compared with the present climate. These results suggest that China would face a challenge to take adaptation measures to cope with the projected frequency increase of the 2022-like summer heatwave.

5.1 Introduction

During summer 2022, China was affected by an unprecedentedly long and intense heatwave (Hua et al., 2023; Ma and Yuan, 2023; Tang et al., 2023; Yin et al., 2023b). By the end of August, 23 provinces had experienced temperature over 40℃ and the daily maximum temperature (Tmax) equaled or exceeded their historical record at 366 national meteorological stations. Relative to the climatological baseline period (1961-1990), the summer (June to August) mean Tmax in 2022 shows positive anomalies over most of eastern China (Figure 5.1a). However, the heatwave was especially intense over the regions from the Sichuan Basin to the middle and lower reaches of the Yangtze River valley, with anomalies peaking above 6℃ around the mid-August (Figure 1a and 1b). The intensity of this regional heatwave is the strongest since 1961 (National Climate Center. 2022), with 4.49 million people in need of subsistence assistance due to the associated drought and 4,284 million hectares of crops affected (Ministry of Emergency Management. 2022).

Previous studies have demonstrated that anthropogenic forcings have increased the frequency of the most extreme heatwaves around the world (e.g. Horton et al., 2015; Otto et al., 2012; Sun et al., 2016; Chen and Dong, 2019; Ren et al., 2020; Ma et al., 2020). By comparing the simulations under all external forcing with the simulations under natural-only forcing based on the Grid-point Atmospheric Model of the IAP LASG version 3 (GAMIL3), Zhang et al. (2023b) found that the anthropogenic forcings increased the probability of Yangtze River heatwave in 2022 by ~11.1 times. Wang et al. (2024) used the multi-model mean of CMIP6 to investigate the 2022-like heatwave and found that the occurrence probability of heatwave has increased by ~62.0 times due to human influences. Anthropogenic forcings include greenhouse gas, aerosols and land cover produced by human activities. While these previous studies implicated a role for changes to anthropogenic forcing on the 2022 Yangtze River heatwave, they mainly relied only on the comparisons of simulations with either all external forcing and natural-only forcing. In this study, we investigate how the anthropogenic forcings, including anthropogenic aerosols and greenhouse gas, have influenced the 2022-like summer heat wave over the Yangtze River valley.

Due to the continuing influence of global warming, warm extremes are also expected to become more frequent over China in the future (Sun et al., 2014; Sun et al., 2018; Hu and Sun, 2020; Chen and Dong, 2021; Wang and Yan, 2021). Wang et al. (2024) found that the 2022-like extreme heatwave event over the middle and lower reaches of the Yangtze River is projected to occur almost every 2 years by the 2050s under the SSP5-8.5 or by the 2070s under the SSP2-4.5. The 2022 summer heatwave in the middle reaches of the Yangtze River could occur every 8.5 years by 2070-2100 under the SSP3-7.0 (Hua et al., 2023). In the recent years, due to the goal set in the Paris Agreement (UNFCCC, 2015), future projections based on target global warming levels (GWLs) are more frequently used to communicate the impact of climate change. For example, Sun et al. (2018) projected that the heatwave events with Tmax above 35°C (with return periods of 5, 10 and 50 years in the current climate (1995-2004)) will increase by 2.5, 3.5 and 5.5 times at the 1.5°C GWL. Nevertheless, by the end of the 21st century, the likely range of global mean surface temperature (GMST) increase is 2.0-4.9 °C with a median of 3.2°C (Raftery et al., 2017). However, the temperature related impacts of higher warming scenarios (e.g., of 3°C and above) are less emphasized in the IPCC AR6 (Jehn et al., 2021; 2022). An assessment of how the probabilities of the 2022-like summer heatwave at different GWLs changes is also still lacking. Therefore, in order to provide comprehensive risk information in better decision-making and strategic planning for the region, it is essential to quantify the changing risks associated with the 2022-like summer heatwave at 1.5°C, 2°C, 3°C and 4°C GWLs.

The CMIP6 models demonstrate overall improvements in simulating extreme climate in China compared with previous phase (Chen et al., 2020). This chapter is based on observations and the multi-model ensemble mean of CMIP6, and is structured as follows: Section 5.2 describes the data and methods used in this study. Section 5.3.1 shows the observed characteristics of the unprecedented 2022 summer heatwave in China and the associated physical processes. Section 5.3.2 illustrates the roles of anthropogenic forcings on the probability of the 2022-like summer heatwave event and discusses the role of individual anthropogenic forcings. The future changes of the 2022-like summer heat event

at different GWLs are discussed in Section 5.3.3 and the conclusions are summarized in Section 5.4.

5.2 Data and Methods

5.2.1 Data

The ERA5 reanalysis dataset is used for summers of 1961-2022 with a resolution of 0.5° x 0.5° (Copernicus Climate Change Service [C3S], 2017). Xu et al. (2022) demonstrated that the observed daily temperatures over China (mean temperature, maximum temperature and minimum temperature) can be well reproduced by ERA5 reanalysis, especially during summer. Here we examine the performance of ERA5 by comparing it to the daily gridded CN05.2 temperature dataset during 1961-2020 which is derived from the National Meteorological Information Center of China through in-situ observations at 2,416 stations over China, with a half degree horizontal resolution. We find that ERA5 can represent the summer climatology and extreme value (90th percentile) distribution patterns of temperature during 1961-2020 with a high pattern correlation coefficient of 0.97 (Figure 5.5). The trend and interannual variability of Tmax anomalies are also captured by ERA5. Therefore, the Tmax and atmospheric circulation field data obtained from the ERA5 reanalysis dataset are used to analyze this extreme event.

The Climate Model Intercomparison Project (CMIP), the Detection and Attribution Model Intercomparison Project (DAMIP) and the Scenario Model Intercomparison Project (ScenarioMIP) from CMIP6 are used in this study (Eyring et al., 2016; Gillett et al., 2016). The historical simulations from CMIP6 cover the period 1850-2014. To analyze the influence of anthropogenic forcings on the likelihood of the 2022-like summer heatwave event, a 10-year window of 2018-2027 is selected to represent 2022. The simulations over this 10-year period from the SSP2-4.5 experiment in ScenarioMIP are used as 2022 all-forcing simulations (hist-ALL), and the simulations over the period of 2018-2020 from the hist-NAT experiment and the period of 2021-2027 from the ssp245-NAT experiment in DAMIP are used as 2022 natural-forcing simulations. The all-forcing simulations are forced by both anthropogenic forcings (well-mixed greenhouse gases, anthropogenic aerosols, ozone, and land use change) and natural forcings (volcanic and solar activities), while the

natural-forcing simulations are driven by natural external forcings alone (Gillett et al., 2016). Additionally, the 10-year simulations are also selected from the hist-GHG and ssp245-GHG experiments and the hist-AER and ssp245-AER experiments in DAMIP to analyze the relative roles of greenhouse gas forcing and aerosol forcing on the 2022-like summer event. The greenhouse gas-forcing simulations are forced by well-mixed greenhouse gas changes only and the aerosol-forcing results are forced by changes in aerosol forcing only (Gillett et al., 2016). The detailed introductions about the ssp245 experiments in DAMIP are illustrated in Supplementary Data. To analyze the changes in future risk, the future projections from ScenarioMIP are used over the period of 2015-2100. Specifically, we use scenario SSP3-7.0, which reaches a radiative forcing of 7.0 $W \cdot m^{-2}$ in 2100 with particularly high aerosol emissions, and SSP5-8.5, which represents the highest forcing pathway with a radiative forcing of 8.5 $W \cdot m^{-2}$ in 2100 (O'Neill et al., 2016). The bilinear interpolation method is used to regrid the model outputs to a common 1.5° × 1.5° grid to facilitate model intercomparison. In total, multi-ensemble simulations from 10 models are used (see Table 5.1). For probability assessment, all year results of ensemble model simulations during the selected time window are used without time or ensemble averaging. For multi-model mean, the multi-ensemble mean is calculated for each individual model first and then the multi-model mean is the mean of all models.

5.2.2 Methods

a. Definition of the extreme index

This study focuses on regions from the Sichuan Basin to the middle and lower reaches of the Yangtze River valley (28~34°N, 102.5~121.5°E, black box in Figure 5.1a). Considering the spatial extent and the magnitude of the temperature anomalies during summer 2022, an index of the highest 10-day running mean of Tmax anomalies in summer (June-July-August) (TXa10day) is defined over this study region. Firstly, in order to remove impacts of the seasonal cycle on event selection, the daily Tmax anomalies relative to the daily 1961-1990 climatology are calculated for each calendar day at each grid box (Peterson et al., 2012). Then, the gridded Tmax anomalies are area-averaged over the study region. Finally, the 10-day running mean area-averaged Tmax anomalies in summer for each year

are calculated and the hottest value is chosen to be the TXa10day for each year. Furthermore, each grid box can have its TXa10day in each year by using the above methods. If the TXa10day in 2022 of one grid box is the largest since 1961, this grid box will be defined as a record-breaking grid box. To correct the model systematic biases in simulating the TXa10day over the region, TXa10day anomaly for observations and various model simulations is calculated as the anomaly relative to the corresponding 1961–1990 climatologies in observations and CMIP6 historical simulations.

The probability density functions (PDF) of TXa10day for each experiment is estimated using generalized extreme value (GEV) distribution (Ailliot et al., 2011). The exceedance probability for the 2022-like summer heatwave event is estimated from GEV fitted PDFs for various experiments. The samples used in GEV distribution are based on all the simulated years during the time window of all members (e.g. 37 members x 10 years = 370 data points). The probability ratio (PR) in hist-ALL relative to hist-NAT is calculated to quantify the changing likelihood of the 2022-like summer heatwave event due to anthropogenic influences (Coles, 2001; Allen, 2003). The PR in future projections is calculated relative to hist-ALL to assess the likelihood changes relative to the present climate. The probability and PR uncertainty with the 95% confidence interval (95% CI) are estimated by bootstrap in 1000 resamples of model ensemble members to determine the empirical 2.5th and 97.5th percentiles (Peterson et al., 2012). The detailed method is shown in Supplementary Method.

b. Time windows of the 1.5℃, 2℃, 3℃ and 4℃ global warming levels

In accordance with the IPCC AR6 report (Lee et al., 2021), the GWLs refer to the time periods when the GMST has warmed by 1.5°C, 2°C, 3°C and 4°C relative to the pre-industrial period (1850-1900). In order to remove the interannual variability, a 20-year running average is used to smooth the GMST time series (Liu et al., 2020). Specifically, we use a 20-year window that has 10 years before and 9 years after the year that exceeds these four global warming thresholds to obtain relatively stabilized future climate states at different GWLs (Zhang et al., 2024c). Each model member has its individual time window of each GWL (Table 5.2 & 3). All members reach 3°C GWL under the two scenarios (not

shown). By the end of the 21st century, all members under the SSP5-8.5 reach the 4°C GWL, but only 19 members (7 models) reach this warming level under the SSP3-7.0.

5.3 Results

5.3.1 Observed characteristics of the 2022 summer heatwave event

Figure 5.1a and c show the spatial patterns of the summer mean Tmax anomalies and TXa10day during summer 2022, respectively. It can be seen that the TXa10day over the study region is much larger than the other regions with a lot of record-breaking grid boxes. Large TXa10day values are also collocated with large seasonal mean Tmax anomalies. By taking the regional average, the TXa10day during summer 2022 over the study region occurred on 17th August with a value of 6.50℃ (Figure 5.1b), corresponding to the 10-day running mean Tmax of 35.40℃ during the period (13th -22nd August) in the region. The observed time series of the regional averaged TXa10day anomalies during 1961-2022 are also shown in Figure 5.1d. Over the study region, TXa10day anomaly is 4.15℃ in summer 2022, which is the highest since 1961 and 4 times the interannual standard deviation.

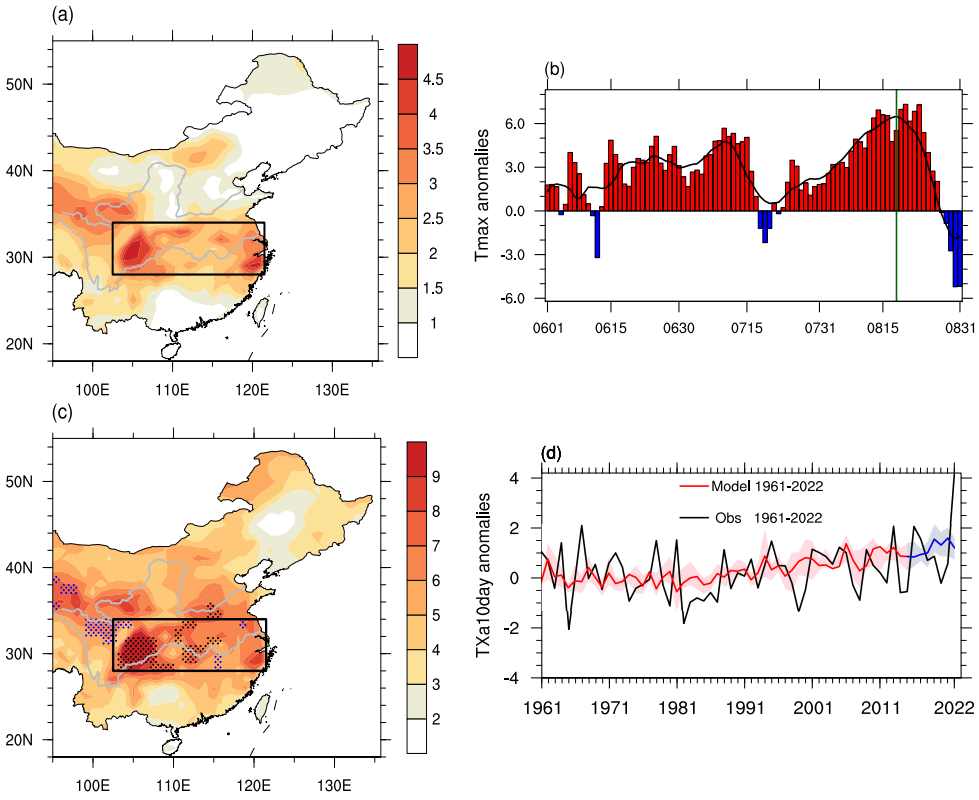

Figure 5.1 (a) Spatial distribution of summer mean Tmax anomalies (°C) in 2022 relative to the baseline period 1961-1990 in observations. The black box represents the study region. (b) Time series of the observed daily Tmax anomalies and its 10-day running mean (°C) averaged over the study region during the 2022 summer. Red (blue) bars denote positive (negative) Tmax anomalies relative to the baseline period. The vertical green line represents the date when the TXa10day occurs in summer 2022. (c) Spatial distribution of the observed TXa10day (°C) in summer 2022. The black dotted regions are record-breaking areas and the blue dotted regions are the areas where the TXa10day of summer 2022 is the second largest since 1961. (d) Time series of regional averaged TXa10day anomalies (°C) relative to the climatology of TXa10day during 1961-1990 over the study region. The black line is observations during 1961-2022. The red (blue) line is multi-model ensemble mean based on historical simulation (SSP2-4.5) during 1961-2014 (2015-2022). The red and blue shaded is the interquartile ranges of the CMIP6 models.

Figure 5.2 illustrates the anomalous atmospheric circulations on 13th-22nd August associated with the 2022 heatwave event. The western Pacific subtropical high shows a westward shift and its western edge reaches the Tibetan Plateau (Figure 5.2a). Under the control of this extremely westward subtropical high, the study region is dominated by anomalous descent (Figure 5.2b), which will suppress convection and precipitation, and is consistent with the increases in the net surface shortwave radiation (Figure 5.2c and 2d, Wang et al., 2016; Liu et al., 2019b). The northward movement of the 200-hPa jet stream

can also influence the vertical motion and water transport (Zhou et al., 2022b, Figure 5.2e), which is associated with positive temperature anomalies and reduced precipitation over the Yangtze River Valley (Liu et al., 2019a; Zhou et al., 2022a). This long-lasting and extreme heatwave event over the study region is consistent with the above anomalous atmospheric circulations.

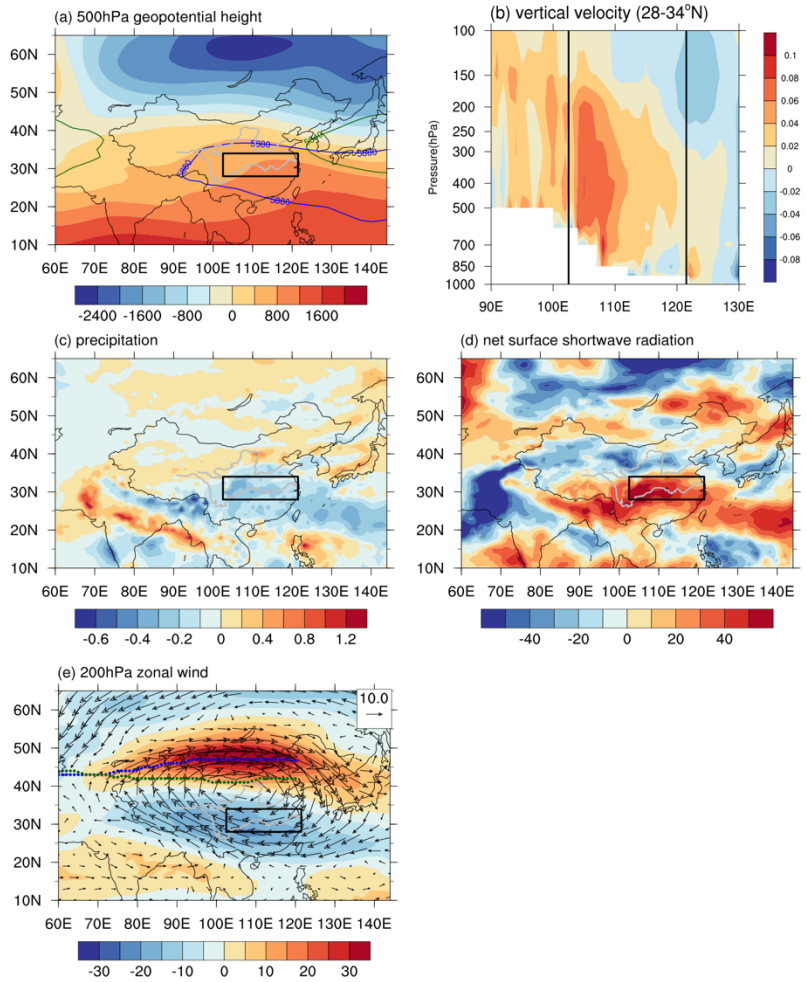

Figure 5.2 Spatial distributions of (a) 500-hPa geopotential height anomalies (m), (b) vertical velocity anomalies (Pa·s^{-1}) averaged over 28~34°N, (c) precipitation anomalies (mm·day^{-1}), (d) net surface shortwave radiation anomalies (W·m^{-2}) and (e) 200-hPa zonal wind anomalies and 200-hPa wind anomalies vector (m·s^{-1}) during 13th -22nd August relative to the climatology of 13th -22nd August during 1961-1990. The blue (green) lines in (a) and (e) are the locations of the western Pacific subtropical high and 200-hPa westerly jet axis during 13th -22nd August 2022 (1961-1990 climatology) respectively. The black box represents the study region.

5.3.2 Anthropogenic influences on the 2022-like summer heatwave event

Due to the influence of anthropogenic forcings, the occurrence of extreme heatwave events becomes more frequent across China (Ma et al., 2017; Ren et al., 2020). Considering

the high intensity and adverse impacts of the 2022 summer heatwave event, we now discuss the roles of anthropogenic forcings on the likelihood of this event.

The model performance of simulating TXa10day anomalies is evaluated by using the historical simulations and results are given in Figure 5.1d and Figure 5.6. The multi-model ensemble mean of CMIP6 captures a slight increasing trend of TXa10day anomalies during 1961-2014 (Figure 5.1d), especially a significant increasing trend (P=0.05) after 1982, which is also shown in observations. Note that the multi-model mean times series is not highly correlated with observed time series. This is expected since observed time series is the combined effects of external forcing and internal climate variability while the multi-model mean times series is the response to external forcing (Hawkins and Sutton., 2009; Deser et al., 2016). By using the K-S test, the distributions of the observed and simulated TXa10day anomalies for summers during 1961-2022 are found to be statistically indistinguishable (P=0.05, Figure 5.6). Therefore, CMIP6 model simulations are appropriate for further attribution analysis. However, the 2022 summer heatwave event is too rare in both observations and model simulations during the historical period 1961-2022 (Figure 5.6), which hinders robust conclusions on the influence of anthropogenic forcings on an event of the observed magnitude. Therefore, we define a 2022-like summer heatwave event by using the threshold of a 1-in-100-year heatwave event in observations with a value of TXa10day anomaly 3.19℃, which is still larger than the observed TXa10day anomalies before 2022. The simulated probability of the 2022-like summer heatwave event is 1.2%, which is also close to the 1% probability in observations.

Figure 5.3 shows the PDFs of TXa10day anomalies in 2022 summer under different forcings. In simulations with natural forcings, the probability of TXa10day which is larger than the 2022-like event is 1.9% (CI: 0.1%-3.4%), corresponding to a return period of 53 years. Under the influences of anthropogenic forcings, the PDF shifts rightward to large TXa10day anomalies under all-forcing simulations relative to natural-forcing simulations, with the probability of 6.0% (CI: 4.1%-7.7%) for extreme events similar to the 2022-like summer one. These results indicate that the 2022-like summer heatwave event is more likely to occur under the influences of anthropogenic forcings and that, furthermore, the

anthropogenic forcings have increased the occurrence of the 2022-like summer heatwave event by about 3 times relative to the probability under natural forcings. Such a change corresponds to a change of return period from 1-in-53-year event under natural forcing to 1-in-17-year event under all forcing.

The PDFs of TXa10day anomalies in single forcing (hist-GHG and hist-AER) have also been analyzed to quantify relative roles of greenhouse gas forcing and aerosol forcing on the likelihood of the 2022-like summer heatwave event and results are also shown in Figure 5.3. The probability of the 2022-like event under aerosol forcing is zero (CI: 0-0.06%), due to the surface cooling caused by aerosols (Krishnan and Ramanathan, 2002). In contrast, the likelihood of the 2022-like summer heatwave event is the largest under the greenhouse gas forcing with a probability of 23.1% (CI: 18.9%-26.8%). The impacts from greenhouse gas changes overwhelm the impacts from aerosol changes, leading to an increased probability of the 2022-like summer heatwave event from natural-forcing simulations to all-forcing simulations. Considering aerosol property in the real-world and model simulations over the study region, Figure 5.7 shows the variations of aerosol optical depth at 550nm (AOD). The time evolutions of AOD in CMIP6 model historical simulations are similar to those in observations with a correlation coefficient of 0.87 and the magnitude is close to that in observations, suggesting the magnitude and variation of AOD over the Yangtze River valley are realistically captured by CMIP6 models. Given the fact that only three models have the ensemble ssp245-NAT, ssp245-GHG and ssp245-AER experiments that are included in Figure 5.3, in order to show the sensitivity to including these three models, Figure 5.8 shows the PDFs of TXa10day anomalies in 2022 summer after removing the ensemble members of these three experiments. The shapes of these PDFs are very similar to the original ones, especially the parts of the lines which are over the 3.19℃ threshold. These results indicate that the conclusions about the human influence are not sensitive to using of the ensemble members under ssp245-NAT, ssp245-GHG and ssp245-AER experiments.

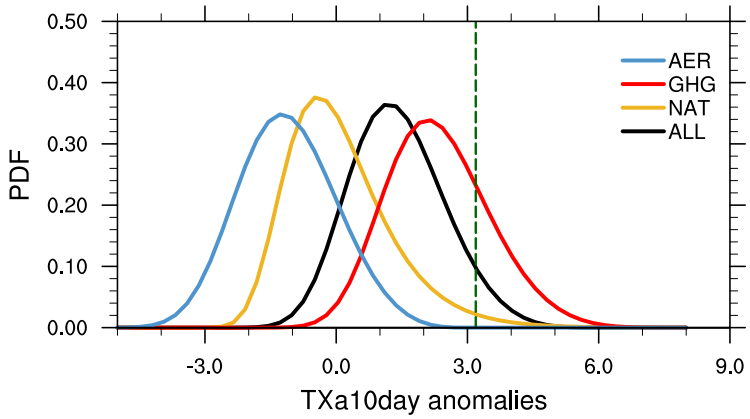

Figure 5.3 The GEV fitted probability density functions of regional averaged TXa10day anomalies for the present climate under all forcing (black), natural forcing (yellow), greenhouse gas forcing (red) and aerosol forcing (blue). The green vertical dashed line represents the threshold of the observed 2022-like summer heatwave event. The samples used in GEV fitting are all the year's results during the 10-year time window of all ensemble members.

5.3.3 Future projections of the 2022-like summer heatwave event at different global warming levels

As GMST increases under different future forcing scenarios, it is expected that there will be more warm extremes across China, which may lead to increases of heat-related mortality (Zhang et al., 2023a). Therefore, we now assess how future climate change will increase the likelihood of the 2022-like summer heatwave event.

The time series of TXa10day anomalies over the study region during the period 2023-2100 from CMIP6 simulations are shown in Figure 5.4a. The TXa10day anomalies over the study region increase significantly in the future climate. The TXa10day anomalies under the SSP5-8.5 are larger than the ones under the SSP3-7.0 in most years, consistent with the larger anthropogenic forcing of SSP5-8.5. After 2055 (2046), the TXa10day anomalies under SSP3-7.0 (SSP5-8.5) are projected to be larger than the threshold of 2022-like summer heatwave event.

Considering the different GWLs, Figure 5.4b shows that the PDFs of the TXa10day anomalies shift to warmer values at the four GWLs compared with the present climate (2018-2027). For the 2022-like summer heatwave event, the probabilities that any given summer exceeds this threshold at the 1.5℃, 2℃, 3℃ and 4℃ GWLs are about 7.7%, 15.6%, 36.0% and 69.2% (11.9%, 19.5%, 47.5% and 79.4%) under the SSP3-7.0 (SSP5-8.5), respectively

(CIs are shown in Figure 5.4c). These probabilities indicate this magnitude of extreme will become a 1-in-13-year, 1-in-6.4-year, 1-in-2.7-year and 1-in-1.4-year (1-in-8.4-year, 1-in-5-year, 1-in-2-year and 1-in-1.3-year) event at the four GWLs under the SSP3-7.0 (SSP5-8.5). In other words, probabilities of the 2022-like summer heatwave event are projected to increase by 1.3-fold, 2.6-fold, 6-fold and 11.5-fold (2-fold, 3.3-fold, 7.9-fold and 13.2-fold) at the 1.5℃, 2℃, 3℃ and 4℃ GWLs under the SSP3-7.0 (SSP5-8.5) relative to the probability under all forcing during the present climate with a value of 6.0%. Furthermore, the probability under the SSP5-8.5 is larger than the one under the SSP3-7.0 at each GWL. Hence, the occurrence of the 2022-like summer heatwave event over the study region will be more frequent in the future climate under the influence of global warming.

Additionally, the variations of the exceedance probabilities and PRs for the 2022-like summer heatwave event with the changing GWLs are shown in Figure 5.4c and d. With the increasing of GWLs, the probabilities and PRs of the 2022-like summer heatwave event exhibit exponential growth. Figure 5.4e shows the relationships between magnitude of the TXa10day anomalies and the GWLs. The slope between TXa10day anomalies and GWLs is 1.06 and 1.15 under the SSP3-7.0 and SSP5-8.5, respectively. These results indicated that the magnitude of change in TXa10day anomalies is almost linear with GWLs and is slightly faster than GWLs.

To show the sensitivity to models of the projected likelihood of the 2022-like summer heatwave event at different GWLs, we calculated probability ratios in five models with multi-ensemble simulations and one group model by combining those models with only one member together. The probability ratios and their CIs at different GWLs in those individual models are shown in Figure 5.9. It can be seen that the PRs in these individual models increase with the increasing GWLs and show exponential growth. The characteristics are consistent with the ones in Figure 5.4d and indicate that projected likelihood changes are consistent among different models.

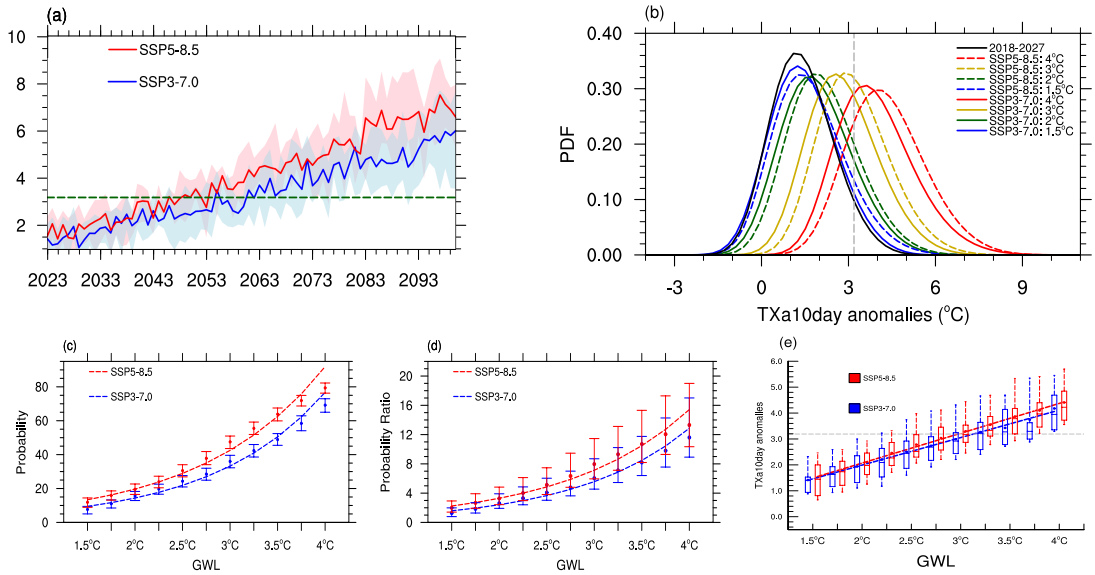

Figure 5.4 (a) Time series of simulated regional averaged TXa10day anomalies (°C) during the future climate under the SSP5-8.5 (red) and SSP3-7.0 (blue) based on multi-model ensemble mean. The anomalies are relative to the baseline period 1961-1990. The shaded is the interquartile ranges among all models. (b) The GEV fitted probability density functions of simulated regional averaged TXa10day anomalies in the present climate (2018-2027), at the 1.5°C, 2°C, 3°C and 4°C GWLs. The samples used in GEV fitting are all the year's results during the 20-year time window of all members. Solid (Dashed) lines represent SSP 3-7.0 (SSP5-8.5). The grey dashed lines in (a) and (b) represent the threshold of the 2022-like summer heatwave event in observations. (c) The probabilities and the 95% confidence intervals (CIs) of the 2022-like summer heatwave event at the different GWLs and the fitted exponential curves under the two scenarios. (d) Same as (c), but for the probability ratios at the different GWLs. (e) Box plots of the TXa10day anomalies (°C) at different GWLs under the two scenarios. With each box, the horizontal lines from top to bottom denote the maximum value, the 75th percentile, the median value, the 25th percentile and the minimum value of the 10 models. The dot represents the multi-model ensemble mean. The dashed lines are the line-plot of multi-model ensemble mean. The grey line is the observed threshold of the 2022-like summer heatwave event.

5.4 Conclusions

Over the regions from the Sichuan Basin to the middle and lower reaches of the Yangtze River valley, a record-breaking heatwave event occurred during the 2022 summer. Observational analysis shows that the regional averaged heatwave index (TXa10day) appears on 17th August with a value of 6.50°C during the period (13^{th}-22^{nd} August). This corresponds to a TX10day anomaly of 4.15°C relative to the baseline period (1961-1990) climatology, which is 4 times the interannual standard deviation. This heatwave event is mainly controlled by the westward movement of the western Pacific subtropical high. The

intense and stable subtropical high leads to a decrease of precipitation and increases of shortwave radiation over the study region, which promotes the formation of this long-lasting and extreme heatwave event.

In this study, considering the rare probability of the 2022 summer heatwave event, a 2022-like summer heatwave event is defined by using the threshold of a 1-in-100-year heatwave event with a TXa10day anomaly of 3.19℃ in observations during 1961-2022 in order to generate robust attribution conclusions. We used the multi-model ensemble simulations of CMIP6 models under all forcing, natural forcing, greenhouse gas forcing and aerosol forcing to explore the contributions of anthropogenic influences on the 2022-like summer heatwave event. Our results show that the probability of the 2022-like summer heatwave event is 1.9% under natural forcing and 6.0% under all forcing in the present climate (2018-2027), which means that the anthropogenic forcing has increased the likelihood of the 2022-like summer heatwave event by about 3 times relative to naturally forced changes. Considering the individual role of the detailed anthropogenic forcing, the probability of such an extreme event in 2022 summer under greenhouse gas forcing is 23.1%, while this kind of extreme event is unlikely to occur only under the aerosol forcing.

In the future climate, the magnitudes of the TXa10day anomalies are projected to be larger than the threshold of the 2022-like summer heatwave event after 2055 (2046) under the SSP3-7.0 (SSP5-8.5). The probabilities and probability ratios of the 2022-like summer heatwave event increase exponentially with the increasing of GWLs and the probability under the SSP5-8.5 is larger than the one under the SSP3-7.0 at each GWL. At the 4°C GWL, the 2022-like extreme event will become a 1-in-1.4-year and 1-in-1.3-year event under the SSP3-7.0 and SSP5-8.5, respectively, which is an increase of 11.5-fold and 13.2-fold compared with the all-forcing return period during the present climate. The main characteristics of projected likelihood changes of the 2022-like summer heatwave event are consistent among different models. The increases of the likelihood suggest that the ecosystem, society and human health over East China would face higher risks for the 2022-like summer heatwave event. Local government and environment agencies would face a challenge to take adaptation measures to cope with the projected frequency increase of the

2022-like summer heatwave. In this study, we only have analyzed the likelihood changes of this kind of event in the future at different global warming levels. The previous studies demonstrated that the seasonal mean temperature changes control the future changes of heatwaves across the world (Argueso et al., 2016). Therefore, the physical mechanism about how the seasonal mean temperature changes influence the exponentially increased probability of the 2022-like summer heatwave event is worthy to be investigated for the understanding of those projected changes in further studies. Furthermore, the model uncertainty of probability ratios due to human influence could also be assessed in future work if the necessary single-forcing experiments become available for more models and ensemble members.

Acknowledgements

We acknowledge the international modeling groups for providing their data for analysis, the Program for Climate Model Diagnosis and Inter-comparison (PCMDI) for collecting and achieving the model data, the World Climate Research Programme's (WCRP's) Coupled Model Inter-comparison Project (CMIP) for organizing the model data analysis activity. We would like to thank Prof. Andrew Turner and Dr. Laura Wilcox for providing suggestions which help to improve this paper. We would also like two anonymous reviewers for their valuable comments and suggestions on the early version of the manuscript.

Data Availability

The CMIP6 datasets were obtained from CEDA (https://help.ceda.ac.uk/article/4801-cmip6-data). The daily ERA5 dataset is available at https://cds.climate.copernicus.eu/datasets. The observation data CN05 used in Supplementary file was downloaded from CMA (http://data.cma.cn).

5.5 Supporting information

Table 5.1 The model information used in this chapter.

	Model	Resolution (lon x lat)	Members in attribution analysis			Members in future risk analysis
			ssp2-4.5 (2018-2027)	hist-NAT hist-GHG hist-AER (2018-2020)	ssp245-NAT ssp245-GHG ssp245-AER (2021-2027)	
1	BCC-CSM2-MR	320x160	1	1	\	1
2	FGOALS-g3	180x80	1	1	\	1
3	CNRM-CM6-1	256x128	1	1	\	1
4	ACCESS-ESM1-5	192x144	3	3	\	3
5	ACCESS-CM2	192x144	3	3	\	3
6	MIROC6	256x128	10	10	10	3
7	IPSL-CM6A-LR	144x143	5	5	\	1
8	MRI-ESM2-0	320x160	5	5	\	5
9	NorESM2-LM	144x96	3	3	1	1
10	CanESM5	128x64	5	5	10	5

	Model	Resolution (lon x lat)	Members in historical analysis	
			historical (1961-2014)	ssp2-4.5 (2015-2022)
1	BCC-CSM2-MR	320x160	1	1
2	FGOALS-g3	180x80	1	1
3	CNRM-CM6-1	256x128	1	1
4	ACCESS-ESM1-5	192x144	3	3
5	ACCESS-CM2	192x144	3	3
6	MIROC6	256x128	10	10
7	IPSL-CM6A-LR	144x143	5	5
8	MRI-ESM2-0	320x160	5	5
9	NorESM2-LM	144x96	3	3
10	CanESM5	128x64	5	5

Table 5.2 The 20-yr windows of each member at different global warming levels under SSP3-7.0.

Model	1.5°C	2°C	3°C	4°C
BCC-CSM2-MR	2016-2035	2027-2046	2051-2070	2075-2094
FGOALS-g3	2012-2031	2028-2047	2063-2082	/
CNRM-CM6-1	2013-2032	2027-2046	2045-2064	2061-2080
ACCESS-ESM1-5	2014-2033	2032-2051	2048-2067	2066-2085
	2011-2030	2025-2044	2044-2063	2066-2085
	2015-2034	2031-2050	2048-2067	2070-2089
ACCESS-CM2	2010-2029	2021-2040	2042-2061	2060-2079
MIROC6	2024-2043	2036-2055	2060-2079	/
	2023-2042	2034-2053	2065-2084	/
	2026-2045	2038-2057	2062-2081	/
IPSL-CM6A-LR	2005-2024	2014-2033	2034-2053	2051-2070
MRI-ESM2-0	2011-2030	2024-2043	2047-2066	2071-2090
	2014-2033	2026-2045	2048-2067	2072-2091
	2013-2032	2025-2044	2053-2072	2075-2094
	2013-2032	2023-2042	2048-2067	2074-2093
	2011-2030	2023-2042	2048-2067	2075-2094
NorESM2-LM	2032-2051	2049-2068	2073-2092	/
CanESM5	2005-2024	2007-2026	2022-2041	2038-2057
	2005-2024	2006-2025	2020-2039	2035-2054
	2005-2024	2005-2024	2020-2039	2034-2053
	2005-2024	2005-2024	2020-2039	2036-2055
	2005-2024	2005-2024	2021-2040	2036-2055

Table 5.3 Same as Table 5.2, but for SSP5-8.5.

Model	1.5°C	2°C	3°C	4°C
BCC-CSM2-MR	2014-2033	2025-2044	2044-2063	2064-2083
FGOALS-g3	2012-2031	2032-2051	2052-2071	2077-2096
CNRM-CM6-1	2008-2027	2020-2039	2040-2059	2052-2071
ACCESS-ESM1-5	2011-2030	2022-2041	2040-2059	2056-2075
	2012-2031	2022-2041	2040-2059	2057-2076
	2015-2034	2026-2045	2042-2061	2058-2077
ACCESS-CM2	2010-2029	2021-2040	2038-2057	2051-2070
MIROC6	2021-2040	2034-2053	2053-2072	2069-2088
	2022-2041	2034-2053	2055-2074	2071-2090
	2020-2039	2032-2051	2051-2070	2067-2086
IPSL-CM6A-LR	2005-2024	2015-2034	2032-2051	2046-2065
MRI-ESM2-0	2008-2027	2018-2037	2038-2057	2059-2078
	2011-2030	2021-2040	2039-2058	2058-2077
	2012-2031	2025-2044	2046-2065	2063-2082
	2011-2030	2022-2041	2042-2061	2060-2079
	2007-2026	2019-2038	2040-2059	2057-2076
NorESM2-LM	2027-2046	2040-2059	2060-2079	2075-2094
CanESM5	2005-2024	2007-2026	2021-2040	2034-2053
	2005-2024	2005-2024	2018-2037	2032-2051
	2005-2024	2005-2024	2019-2038	2032-2051
	2005-2024	2005-2024	2019-2038	2033-2052
	2005-2024	2005-2024	2020-2039	2033-2052

Supplementary Data

1. ssp245-NAT, ssp245-GHG and ssp245-AER experiments

These three experiments cover the period 2015-2100. ssp245-NAT, ssp245-GHG and ssp245-AER experiments involves at least one of the hist-NAT, hist-GHG and hist-AER simulations to 2100 using SSP2-4.5 solar and volcanic forcing, well-mixed greenhouse gas concentrations and aerosol concentrations, respectively (Gillett et al., 2016).

Gillett N P, Shiogama H, Funke B, et al. The detection and attribution model intercomparison project (DAMIP v1. 0) contribution to CMIP6. *Geoscientific Model Development*, 2016, 9(10): 3685-3697.

Supplementary Method

1. Probability, probability ratio and confidence interval

In this study, the probability is estimated from the Generalized Extreme Value (GEV) distribution fitted to the Tx10day anomalies (Wilks, 2011). The cumulative probability distribution (CDF) for the GEV distribution is determined as follow:

$$F(x) = exp\left\{-\left[1+\frac{\kappa(x-\mu)}{\sigma}\right]^{-\frac{1}{\kappa}}\right\}$$

where μ, σ and ξ are the location, scale and shape parameter, respectively. These parameters are estimated with the method of maximum likelihood estimation (e.g., Ma et al., 2020). The probability for the 2022 summer-like event is calculated by *(1-F(x))* and the corresponding return period is *1/(1-F(x))*.

The probability ratio (PR) is defined as the ratio between the probabilities of the observed 2022 summer-like heatwave event occurring under all forcing and natural forcing or the probabilities occurring at different global warming levels (GWLs) under future scenarios with all forcing. The confidence intervals (CI) of the probability and PR are estimated based on 1000 bootstrap samplings by repeated resampling. The 2.5th and 97.25th percentiles of the 1000 bootstrap results are used to estimate the 95% CI.

WILKS, D. S. Statistical methods in the atmospheric sciences. San Diego: Academic Press, 2011.

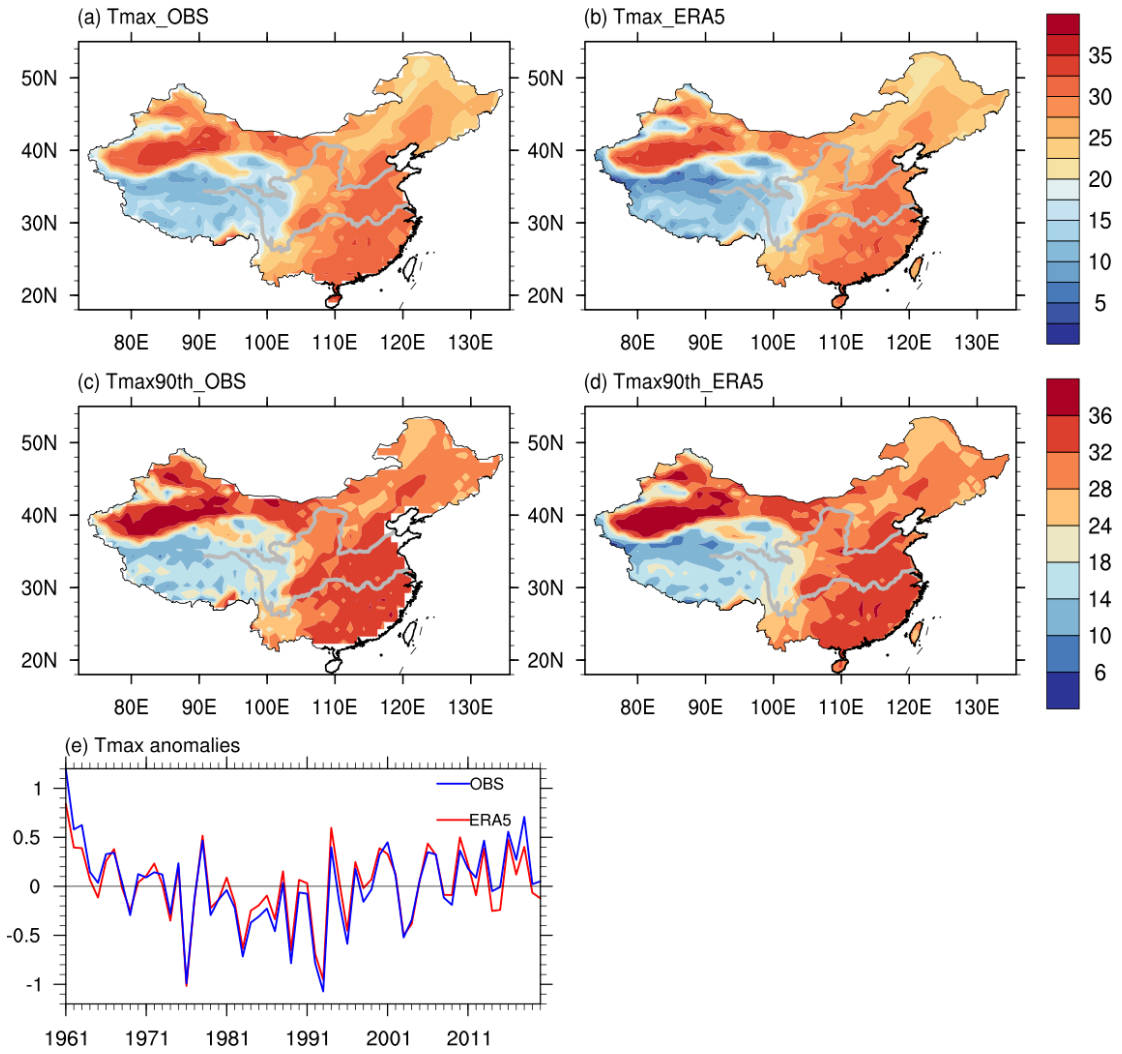

Figure 5.5 Spatial patterns of (a, b) climatology (°C) and (c, d) 90th percentile (°C) of Tmax in observations and ERA5 in summer of 1961-2020. (e) Time series of Tmax anomalies (°C) averaged over China during 1961-2020 in observations (blue line) and ERA5 (red line). The anomalies are relative to the baseline period 1961-1990.

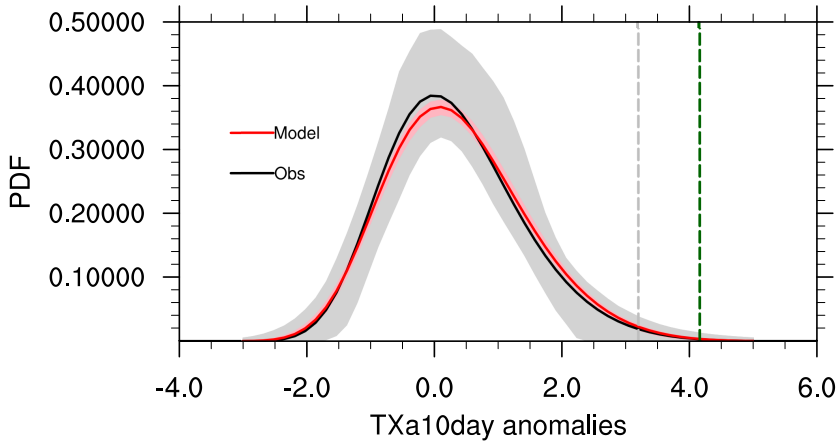

Figure 5.6 The GEV fitted probability density function of the observed (black line) and simulated (red line) regional averaged TXa10day anomalies over the study region (28~34°N, 102.5~121.5°E) during 1961-2022. The model results during 1961-2014 are from the ensemble historical simulations and the model results during 2015-2022 are from the SSP2-4.5 ensemble simulations. The green line is the observed threshold of the 2022 summer heatwave event. The grey line is the observed threshold of the 2022-like summer heatwave event, defined by using the threshold of a 1-in-100-year heatwave event in observations with a value of TXa10day anomaly 3.19℃. The shaded is the 95% confidence interval by using bootstrap 1000 times.

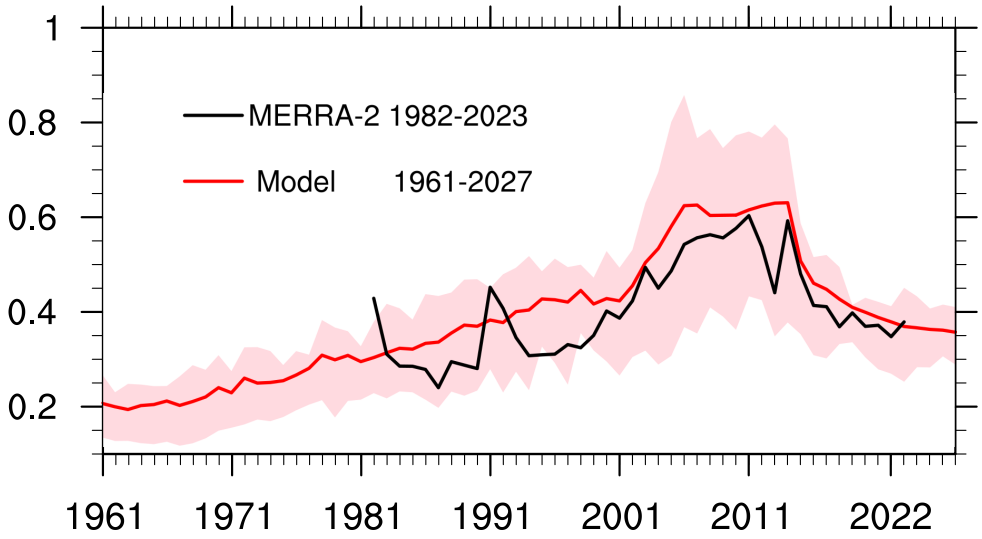

Figure 5.7 Time series of summer mean aerosol optical depth at 550nm averaged over the study region in observations and the multi-model mean CMIP6 simulations. Observation data is derived from MERRA-2 reanalysis dataset. The red shaded is the interquartile ranges of the CMIP6 models.

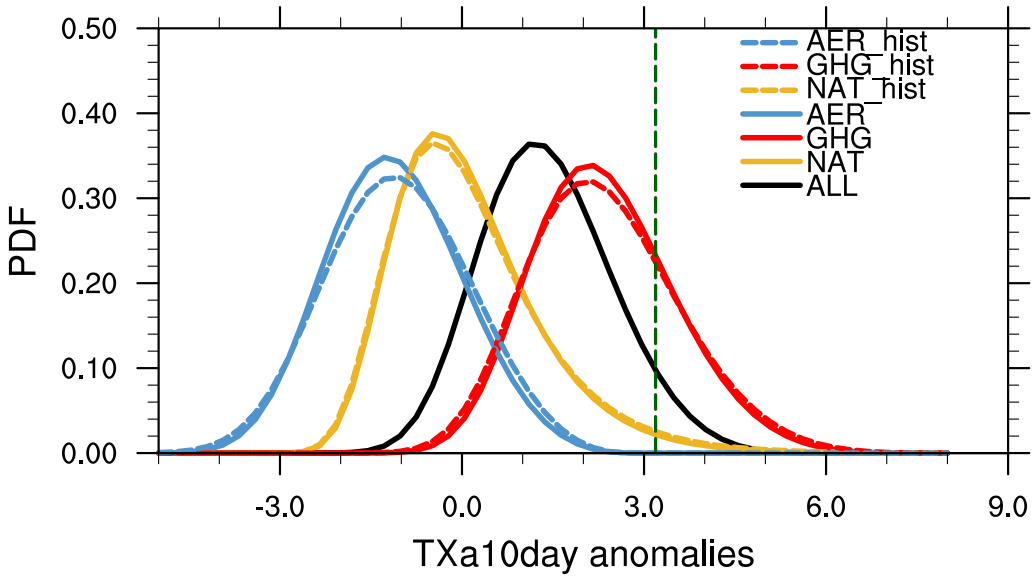

Figure 5.8 The GEV fitted probability density functions of regional averaged TXa10day anomalies for the present climate under all forcing (black), natural forcing (yellow), greenhouse gas forcing (red) and aerosol forcing (blue). The solid lines are the results based on the combined ensemble members of hist-NAT, hist-GHG, hist-AER, with ssp245-NAT, ssp245-GHG and ssp245-AER. The dashed lines are the results based on the ensemble members from hist-NAT, hist-GHG and hist-AER. The green vertical dashed line represents the threshold of the observed 2022-like summer heatwave event.

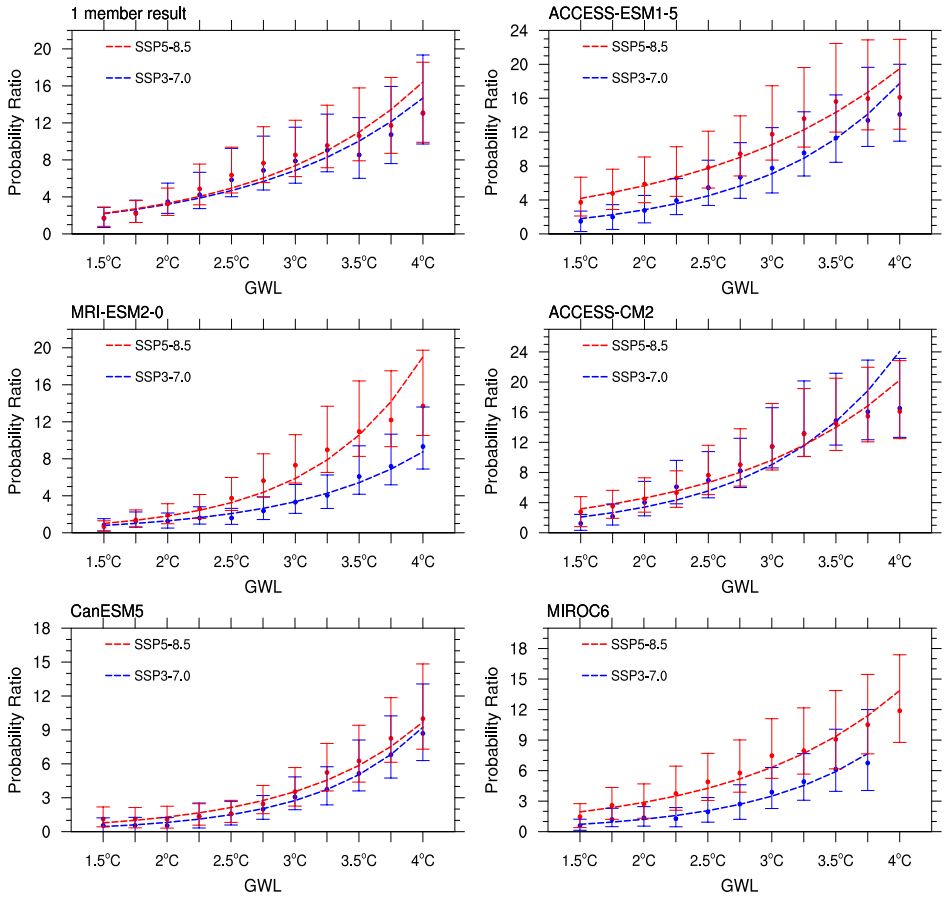

Figure 5.9 The probabilities ratios and the 95% confidence intervals (CIs) of the 2022-like summer heatwave event at the different GWLs and the fitted exponential curves under the two scenarios based on one-member model group and the other five models.

Chapter 6

Conclusions and Discussion

Heatwaves (HWs) are weather events characterized by extreme hot surface air temperature anomalies that persist for several days, and thus leading to devastating impacts on society. Understanding how HW properties have changed during the historical period and how they might change in future is an important for helping local governments in making policy decisions and mitigating the risks associated with these hot extremes. Process understanding of the involved drivers and physical mechanisms for historical changes and projected changes is key scientific challenges in climate research. Based on observations and the CMIP6 multi-model ensembles, this thesis aims to understand drivers of the historical changes of summer HWs over China, assess future projected changes and model uncertainty at different global warming levels (GWLs), understand the physical processes involved, and assess how anthropogenic forcings have influenced the likelihood of the 2022 extreme HWs over China and how the likelihood of this kind of event will change in the future.

This thesis has advanced understanding drivers and physical processes of HW changes in China during the recent decades and their projected changes in the future at different GWLs. The main findings and conclusions drawn from the thesis and future works are summarized in this Chapter. Chapter 1 raised four scientific questions, and Section 6.1 summarizes the answers found through the work presented in Chapters 2-5. Section 6.2 discusses implications of this thesis and the ideas related with the HWs over China which are worthy to be analyzed in the future studies.

6.1 Conclusions

6.1.1 How have summer HWs changed during the historical period over China?

In this study, Compound HWs are identified when the daily maximum and minimum temperature exceed the baseline 90th percentile for at least three consecutive days. Daytime (Nighttime) HWs are identified when the daily maximum (minimum) temperature exceeds the baseline 90th percentile for at least three consecutive days.

During the 1961-2020, the frequency, intensity and duration of Compound HWs and Nighttime HWs have increased with an abrupt increase around the mid-1990s over China. The largest increase in frequency and duration of HWs, as measured by a linear trend fitted over 1960-2020, is found for Nighttime HWs. Indeed, the trends of the frequency and duration of Daytime HWs are non-significant, but there is still an obvious increase in intensity around the mid-1990s. Although there is no increase in frequency of daytime HWs when averaged over the entire China, there is an increase in frequency of the most intense daytime HWs. It is found that Compound HWs and Nighttime HWs become more frequent with events becoming hotter and durations becoming longer across China in the period 1995-2020 compared with the period 1961-1994.

The historical changes of these three types of HWs show regional differences. The frequency of Compound HWs have increased across much of China, except for the regions between the Yangtze River and Yellow River. The intensity and duration of Compound HWs increase over most regions of China, especially over the central China and western China. The frequency and intensity of Daytime HWs over the central China increase significantly during the recent years. The frequency, intensity and duration of Nighttime HWs increase over China, especially over the western China. The largest frequency and duration appear over the Tibetan Plateau. Among the three types of HWs, the largest historical changes of frequency and duration appear over Southwest China in Nighttime HWs. The historical changes of intensity over Northeast China and Northwest China in Daytime HWs are larger than the other regions.

6.1.2 What role does the external forcing play on the historical changes of HWs? What are the relative roles of greenhouse gas forcing and aerosol forcing on the historical changes of HWs over China and the responsible physical processes?

To assess the role of external forcings and quantify the relative roles of different forcings on the historical changes of these three types of HWs, we used 11 CMIP6 multi-model ensemble historical simulations and DAMIP single forcing simulations.

CMIP6 historical simulations capture the main changes in the frequency, intensity, and duration of all three types of HWs seen in observations during recent decades. The

magnitudes of the historical changes under historical external forcing are similar to the observed ones in most regions except that models overestimate changes in HW duration. These results indicate that external forcings have played an important role in the historical changes of HWs over China during recent decades.

Analyses of DAMIP single forcing simulations indicate that the historical changes of HWs over China in all forcing simulations are predominantly induced by changes in greenhouse gas forcing (GHG). The significant increases in simulated Compound HWs and Nighttime HWs over the entire China and the significant increases in Daytime HWs over central China are mainly contributed by GHG changes. Aerosol forcing (AA) changes lead to a dipole pattern of changes in three HW properties with increases over the northern part of China and decreases over the southern part of China.

The historical changes in the properties of HWs can be contributed by the changes in the climatological seasonal mean temperature and the changes in temperature variability. Their relative roles on historical changes in HW properties are assessed. Since there is little change in temperature variability between two periods, the changes in seasonal mean warming (seasonal mean changes in Tmax and Tmin) play the dominant role on the historical changes of HWs over China during recent decades compared with the changes in temperature variability.

The historical changes in the climatological seasonal mean state of physical processes are further discussed to explain the historical changes of seasonal mean warming and therefore HWs. In terms of the physical processes due to GHG changes, the increase of greenhouse gas concentrations and GHG change induced increases of water vapor in the atmosphere lead to the increase of surface longwave radiation. The increases of surface longwave radiation result in the surface warming across China, which is associated with the increases of Compound HWs and Nighttime HWs. Influenced by a decrease of total cloud cover, the surface air temperature becomes warm due to the increases of net surface shortwave radiation, associated with the significant increases of seasonal mean Tmax and Daytime HWs over the central China. Increased aerosol emissions over East Asia and South Asia during recent decades lead to increased AOD and increased cloud cover over large part

of China through aerosol-radiation and aerosol cloud interactions. These are associated with significant decreases in net surface shortwave radiation over Southwest China and eastern China. The dipole pattern of the changes in water vapor with increased water vapor over the northern part of China and the decreases over the southern part of China contributes to the increases of surface clear-sky downward longwave radiation over the northern part of China and the decreases over the southern part of China. These changes in surface radiations in response to AA changes are associated with a dipole pattern of summer mean surface temperature (both Tmax and Tmin) changes with warm anomalies over the northern part of China and cold anomalies over the southern part of China. This north-south dipole pattern of temperature changes explains the larger decadal decreases in three properties of three type HWs over the eastern China and the southern part of China and weak increases over northern China in response to aerosol emission changes.

6.1.3 How will summer Compound HWs over China change in the future at different GWLs?

Wang et al. (2020) showed that compound HWs will most frequently affect societies in the Northern Hemisphere after 2030. Hence, Chapter 3 focused on the future projections of Compound HWs at different GWLs under SSP3-7.0 and SSP5-8.5 scenarios.

The magnitudes and spatial distributions of Compound HW changes relative to the recent climate over China in the future are primarily dependent on the GWL and they are not very sensitive to forcing scenarios used. The frequency of Compound HWs increases significantly over the entire China, especially over Northwest China and Southeast China with a maximum increase of 1.71 (2.74; 4.45; 5.81) events·a^{-1} at the 1.5℃ (2℃; 3℃; 4℃) GWL. The intensity of HWs also increases with increasing GWL and the largest future changes occur over the Northwest China. The duration of HWs also becomes longer with increasing GWL, with the maximum duration of 7.85 (9.75; 15.71 and 26.79) days at the 1.5°C (2°C; 3°C; 4°C) GWL.

The likelihood of extremely rare Compound HWs over China increases with increasing GWLs, which can be expressed as a decrease in return times. Both the 50-year and 100-year rare events are projected to become 1-year event at the 4℃ GWL across China. The 50-year

(100-year) high-intensity event over Northwest China is projected to become a 1.7-year and 1.1-year (2.7-year and 1.2-year) event in the future at the 3℃ and 4℃ GWLs. Furthermore, the 50-year and 100-year long-duration events over Southwest China are projected to become 1-year and 1.2-year events, respectively.

The seasonal mean warming dominates the projected changes in HW properties over China at the different GWLs. Due to the difference in radiative forcing between the SSP5-8.5 and SSP3-7.0, although the spatial patterns and magnitudes of the projected changes are not very sensitive to the scenarios, the physical processes under these two scenarios still show some differences. Under both scenarios, the seasonal mean warming in summer over China is related to the increases of longwave radiation across China, which are partly resulted from increase in greenhouse gas forcing and partly resulted from increased water vapor. This seasonal mean surface warming results in enhanced upward sensible and latent heat fluxes, leading to increased summer mean daily Tmax and Tmin and the enhancement of Compound HWs properties over the entire China. Additionally, surface shortwave radiation also tends to warm the surface air temperature over eastern China and then contributes to the increases of Compound HWs. However, the future changes of shortwave radiation play a weaker role for surface warming relative to the recent climate under the SSP3-7.0 than those under the SSP5-8.5, which is related to increased aerosol changes under the SSP3-7.0 and decreased aerosol changes under the SSP5-8.5.

6.1.4 What is the model uncertainty in the future projections of summer HWs over China and what are the associated physical processes?

There is a model spread in the future projected changes of Compound HWs properties at the 1.5°C, 2°C, 3°C and 4°C GWLs under the SSP5-8.5 among the 24 CMIP6 models. By classifying the models into high-change models and low-change models (hereafter as high-model and low-model), Chapter 4 showed that the magnitudes of the future changes in frequency of high-model are larger than low-model over China at the four GWLs. The maximum difference occurs over the Northeast China with a value of 1.34 (1.80; 2.27) events·a^{-1} at the 1.5℃ (2℃; 3℃) GWL. Except the western part of the Tibetan Plateau, the future changes in intensity of high-model are larger than low-model at the four GWLs. The

differences in the changes of duration between high-model and low-model are small with a value of less than 1 day at the 1.5℃ and 2℃ GWLs. The duration lasts much longer over the Northeast China in high-model compared to the low-model at the 3°C and 4°C GWLs. The ratio of difference between high-model and low-model relative to low-model becomes smaller with the increasing GWLs. It's indicated that the model uncertainty becomes relatively less important at higher GWLs.

In terms of the physical processes related with the difference in HW properties between the high-model and low-model, the increases of surface clear-sky downward longwave radiation of high-model relative to the recent climate are larger than those of low-model over China, resulting from the larger increase of water vapor in the atmosphere in the high-model group. The net clear-sky surface shortwave radiation plays a weak role on the differences of the HWs between the two groups. However, the differences of the net surface shortwave radiation between the two model groups show large positive values over China, especially over the eastern China, which is related to the larger decreases of total cloud cover in high-model. These results suggest that the water vapor feedback and the shortwave cloud radiative effect are two important factors for the spread of projected summer mean warming and HW property changes over China.

6.1.5 How does the anthropogenic forcing influence the likelihood of the 2022 extreme HWs over China? How will the likelihood of this kind of event change in the future?

During summer 2022, China was affected by an unprecedentedly long and intense heatwave (Hua et al., 2023, Ma et al., 2023, Tang et al., 2023, Yin et al., 2023). By the end of August, 23 provinces had experienced temperature over 40℃ and the daily maximum temperature (Tmax) equaled or exceeded their historical record at 366 national meteorological stations. To represent this event, Chapter 5 defined an index named TXa10day, which is the highest 10-day running mean of Tmax anomalies (TXa10day) with the climatological daily mean seasonal cycle removed in summer. The study focuses on regions from the Sichuan Basin to the middle and lower reaches of the Yangtze River valley (28~34°N, 102.5~121.5°E).

Observational analysis shows that the TXa10day over the study region is much larger than the other regions with a lot of record-breaking areas. The largest regional averaged TXa10day over the study region in summer 2022 appears around 17th August with a value of 6.5°C. TXa10day anomaly is calculated as the anomaly relative to the corresponding 1961–1990 TXa10day climatology. Over the study region, TXa10day anomaly is 4.15℃ in summer 2022, which is the highest since 1961 and 4 times the interannual standard deviation. This extreme event is influenced by the westward subtropical high and the northward movement of the 200-hPa jet stream. The study region is dominated by anomalous descent, which is associated with positive temperature anomalies and reduced precipitation over the Yangtze River Valley (Liu et al 2019a, Zhou et al 2022a). The increases in the net surface shortwave radiation also contribute to the warming of surface air temperature.

This event is too rare in both observations and model simulations during the historical period 1961-2022 to make robust attribution statements. Therefore, we assess anthropogenic influences and future changes of a 2022-like summer heatwave event by using the threshold of a 1-in-100-year event in observations with a TXa10day anomaly of 3.19℃. Based on the multi-model ensembles of 10 CMIP6 models, we find that the impacts from greenhouse gas changes overwhelm the impacts from aerosol changes, leading to an increased likelihood of the 2022-like summer heatwave event by about 3 times, which is corresponding to a change of return period from 1-in-53-year event under natural forcing to 1-in-17-year event under all forcing in the present climate (2018-2027).

Climate model projections show that the magnitudes of the TXa10day anomalies are projected to be larger than the threshold of the 2022-like summer heatwave event after 2055 (2046) under the SSP3-7.0 (SSP5-8.5). The probabilities and probability ratios of the 2022-like summer heatwave event increase exponentially with the increasing of GWLs and the probability under the SSP5-8.5 is larger than the one under the SSP3-7.0 at each GWL, but the difference is within the model spreads in both scenarios. Such extreme event will become a 1-in-8.4-year, 1-in-5-year, 1-in-2-year and 1-in-1.3-year event under the SSP5-8.5 at the 1.5℃, 2℃, 3℃ and 4℃ GWLs compared with the present climate.

6.2 Implications and Future work

6.2.1 Implications

Chapter 2 gives a view of the historical changes of HWs over China and showed the dominating role of GHG on the historical changes of HWs. Meanwhile, Chapter 3 suggests that China would face a future with projected frequency increase, intensity enhancement and duration extension of Compound HWs. Considering the adverse impacts of HWs on human well-being and ecosystem (Yin et al., 2023), the increases of HWs in the recent climate and future climate provide important context for the development of better mitigation strategies and adaptation measures to reduce the severe impacts of the increasing HWs on society. Furthermore, the model uncertainty shown in Chapter 4 indicated that the water vapor feedback and the shortwave cloud radiative effect play important roles on the future projections of HWs. It's necessary to improve model performance to decrease the influence of model uncertainty on the projected HWs.

Chapter 5 has shown that the ecosystem, society and human health over East China would face higher risks for the 2022-like summer heatwave event in the future. China would face a challenge to take adaptation measures to cope with the projected frequency increase of the 2022-like summer heatwave. Considering to roles of anthropogenic forcings on the increased probability of the 2022-like summer heatwave event, actions to reduce greenhouse gas emissions are necessary to reduce the impact of such events in the future.

6.2.2 Future work

The research presented in this thesis advances understanding of the historical changes and future projections of summer HWs over China. Nevertheless, it also highlights new questions and ideas for future work.

Chapter 2 discusses the role of external forcing and the relative role of GHG and AA on the recent historical changes of the three types of HWs over China. However, natural climate variability could also influence the decadal warming over Asia around the mid-1990s, such as the Atlantic multidecadal variability and the Interdecadal Pacific Oscillation (Kwon et al., 2007; Hong et al., 2017; Zhang et al., 2024b). Further study is still needed to give a

more comprehensive understanding of the contributions of these factors on the historical changes of HWs over China and how important they might be in the future.

Chapter 4 describes that the model spread in future projections of Compound HWs over China and the responsible physical processes. The results suggest that water vapor feedback and the shortwave cloud radiative effect are two important factors for the spread of projected summer mean warming and HW property changes over China. The previous studies pointed out that clouds and their effects have an important impact on net surface short radiation (Schneider, 1972; Aumann et al., 2012; Chen et al., 2012), which is also identified as a key uncertainty in climate model (Solomon et al., 2007). However, the processes for the spreads of water vapor feedback and shortwave cloud radiative effect among models in projected changes over China are still not clear. It needs more analyses to further understand these spreads.

Chapter 5 finds that the probability of the 2022-like heatwave event increases due to human influence, in which the impacts from greenhouse gas changes overwhelm the impacts from aerosol changes. However, the recent changes (decreases) in aerosols emissions are much larger than those used in CMIP6 model simulations (Wang et al., 2022). It is therefore necessary to explore the influence of the aerosol emission change biases on the changes of likelihood of the extreme event.

The performance of the multi-model ensemble mean of CMIP6 on simulating the HWs is evaluated in Chapter 2-4. Although the models can capture the main features of the observed HWs during the historical period, there are still relatively large biases over the western China which may be related with the relatively large biases in simulating temperature over the western China than the other regions. Hence, it's necessary to improve the model performance on simulating temperature over the western China.

In this study, we used the multi-model ensemble mean as the results of future projections, which is an unconstrained method. O'Reilly et al. (2024) found that the constrained projections are more accurate and reliable for regional temperature projections compared to the unconstrained projections, especially during summer. There are several constrained methods, such as the reliability ensemble averaging method (Giorgi et al., 2003),

the Kriging for Climate Change method (Ribes et al., 2021) and so on. Therefore, the future projections of HWs could also be discussed by using new methods to be compared with the current results.

Heatwaves are not only seen in summer, but also appear in spring and autumn, even in winter (Salzano et al., 2023; Wu et al., 2023). Previous studies found that spring, autumn and winter heatwaves could increase the risks of hospitalization (Schwarz et al., 2020), drive snowmelt (McEvoy and Hatchett, 2022) and lead severe impacts on crop growth (Ding et al., 2022). Hence, the framework provided by chapter 2-4 could be used to assess the historical changes and future changes of the three types of HWs in other seasons and the seasonal-variations of HWs could also be analyzed.

Bibliography

An N, Zuo Z. Changing structures of summertime heatwaves over China during 1961–2017. *Science China Earth Sciences*, 2021, 64: 1242-1253.

Ailliot P, Thompson C, Thomson P. Mixed methods for fitting the GEV distribution. *Water Resources Research*, 2011, 47(5).

Alizadeh M R, Abatzoglou J T, Adamowski J F, et al. Increasing heat-stress inequality in a warming climate. *Earth's Future*, 2022, 10(2): e2021EF002488.

Allen M. Liability for climate change. *Nature*, 2003, 421(6926): 891-892.

Argüeso D, Di Luca A, Perkins-Kirkpatrick S E, et al. Seasonal mean temperature changes control future heat waves. *Geophysical Research Letters*, 2016, 43(14): 7653-7660.

Aumann H H, Ruzmaikin A, Behrangi A. On the surface temperature sensitivity of the reflected shortwave, outgoing longwave, and net incident radiation. *Journal of climate*, 2012, 25(19): 6585-6593.

Awasthi A, Vishwakarma K, Pattnayak K C. Retrospection of heatwave and heat index. *Theoretical and Applied Climatology,* 2022, 147(1): 589-604.

Baldwin J W, Dessy J B, Vecchi G A, et al. Temporally compound heat wave events and global warming: An emerging hazard. *Earth's Future*, 2019, 7(4): 411-427.

Barichivich J, Osborn T, Harris I, et al. Monitoring global drought using the self-calibrating Palmer Drought Severity Index [in" State of the Climate in 2020" eds. Dunn RJH, Aldred F, Gobron N, Miller JB & Willett KM]. *Bulletin of the American Meteorological Society*, 2021, 102(8): S68-S70.

Bevacqua E, Zappa G, Lehner F, et al. Precipitation trends determine future occurrences of compound hot–dry events. *Nature Climate Change*, 2022, 12(4): 350-355.

Boé J, Terray L. Land–sea contrast, soil-atmosphere and cloud-temperature interactions: interplays and roles in future summer European climate change. *Climate Dynamics*, 2014, 42(3): 683-699.

Boucher O, Randall D, Artaxo P, et al. Clouds and aerosols//Climate change 2013: The physical science basis. Contribution of working group I to the fifth assessment report of the intergovernmental panel on climate change. *Cambridge University Press*, 2013: 571-657.

Brás T A, Seixas J, Carvalhais N, et al. Severity of drought and heatwave crop losses tripled over the last five decades in Europe. *Environmental Research Letters*, 2021, 16(6): 065012.

Callahan C W, Mankin J S. Globally unequal effect of extreme heat on economic growth. *Science Advances*, 2022, 8(43): eadd3726.

Campbell S, Remenyi T A, White C J, et al. Heatwave and health impact research: A global review. *Health & place*, 2018, 53: 210-218.

Chambers J. Global and cross-country analysis of exposure of vulnerable populations to heatwaves from 1980 to 2018. *Climatic Change*, 2020, 163(1): 539-558.

Chen H, Sun J, Lin W, et al. Comparison of CMIP6 and CMIP5 models in simulating climate extremes. *Science Bulletin*, 2020, 65(17): 1415-1418.

Chen H, Zhao L, Dong W, et al. Spatiotemporal variation of mortality burden attributable to heatwaves in China, 1979–2020. *Science Bulletin*, 2022, 67(13): 1340-4.

Chen L, Yan G, Wang T, et al. Estimation of surface shortwave radiation components under all sky conditions: Modeling and sensitivity analysis. *Remote Sensing of Environment*, 2012, 123: 457-469.

Chen M, Geng FH, Ma LM, Zhou WD. Analyses on the heat wave events in Shanghai in Recent 138 years . *Plateau Meteorology*, 2013, 32(2):597–607 (in Chinese).

Chen R, Lu R. Dry tropical nights and wet extreme heat in Beijing: Atypical configurations between high temperature and humidity. *Monthly Weather Review*, 2014, 142(5): 1792-1802.

Chen W, Dong B. Anthropogenic impacts on recent decadal change in temperature extremes over China: Relative roles of greenhouse gases and anthropogenic aerosols. *Climate Dynamics*, 2019, 52(5): 3643-3660.

Chen W, Dong B. Projected near-term changes in temperature extremes over China in the mid-twenty-first century and underlying physical processes. *Climate Dynamics*, 2021, 56(5): 1879-1894.

Chen Y, Li Y. An inter-comparison of three heat wave types in China during 1961–2010: Observed basic features and linear trends. *Scientific reports*, 2017, 7(1): 45619.

Chen Y, Zhai P. Revisiting summertime hot extremes in China during 1961–2015: Overlooked compound extremes and significant changes. *Geophysical Research Letters*, 2017, 44(10): 5096-5103.

Choi N, Lee M I, Cha D H, et al. Decadal changes in the interannual variability of heat waves in East Asia caused by atmospheric teleconnection changes. *Journal of Climate*, 2020, 33(4): 1505-1522.

Coles S, Bawa J, Trenner L, et al. An introduction to statistical modeling of extreme values. London: Springer, 2001.

Coumou D, Rahmstorf S. A decade of weather extremes. *Nature climate change*, 2012, 2(7): 491-496.

Della-Marta P M, Luterbacher J, von Weissenfluh H, et al. Summer heat waves over western Europe 1880–2003, their relationship to large-scale forcings and predictability. *Climate Dynamics*, 2007, 29: 251-275.

Deng K, Yang S, Ting M, et al. Dominant modes of China summer heat waves driven by global sea surface temperature and atmospheric internal variability. *Journal of Climate*, 2019, 32(12): 3761-3775.

Deser C, Terray L, Phillips A S. Forced and internal components of winter air temperature trends over North America during the past 50 years: Mechanisms and implications. *Journal of Climate*, 2016, 29(6): 2237-2258.

Ding S, Chen A. Comprehensive assessment of daytime, nighttime and compound heatwave risk in East China. *Natural Hazards*, 2024: 1-19.

Ding T, Qian W, Yan Z. Changes in hot days and heat waves in China during 1961–2007. *International Journal of Climatology,* 2010, 30(10): 1452-1462.

Ding T, Qian W. Geographical patterns and temporal variations of regional dry and wet heatwave events in China during 1960–2008. *Advances in Atmospheric Sciences*, 2011, 28: 322-337.

Ding T, Li X, Gao H. An unprecedented high temperature event in southern China in autumn 2021 and the essential role of the mid-latitude trough. *Advances in Climate Change Research*, 2022, 13(6): 772-777.

Domeisen D I V, Eltahir E A B, Fischer E M, et al. Prediction and projection of heatwaves. *Nature Reviews Earth & Environment*, 2023, 4(1): 36-50.

Donat M G, Alexander L V, Yang H, et al. Updated analyses of temperature and precipitation extreme indices since the beginning of the twentieth century: The HadEX2 dataset. *Journal of Geophysical Research: Atmospheres*, 2013, 118(5): 2098-2118.

Dong B, Gregory J M, Sutton R T. Understanding land–sea warming contrast in response to increasing greenhouse gases. Part I: Transient adjustment. *Journal of Climate*, 2009, 22(11): 3079-3097.

Dong B, Sutton R T, Shaffrey L, et al. Recent decadal weakening of the summer Eurasian westerly jet attributable to anthropogenic aerosol emissions. *Nature Communications*, 2022, 13(1): 1148.

Dong L, McPhaden M J. The role of external forcing and internal variability in regulating global mean surface temperatures on decadal timescales. *Environmental Research Letters*, 2017, 12(3): 034011.

Dong W, Zeng Q, Ma Y, et al. Impact of heat wave definitions on the added effect of heat waves on cardiovascular mortality in Beijing, China. *International journal of environmental research and public health*, 2016, 13(9): 933.

Douville H, Chauvin F, Broqua H. Influence of soil moisture on the Asian and African monsoons. Part I: Mean monsoon and daily precipitation. *Journal of Climate*, 2001, 14(11): 2381-2403.

Ebi K L, Capon A, Berry P, et al. Hot weather and heat extremes: health risks. *The lancet*, 2021, 398(10301): 698-708.

Eyring V, Bony S, Meehl G A, et al. Overview of the Coupled Model Intercomparison Project Phase 6 (CMIP6) experimental design and organization. *Geoscientific Model Development*, 2016, 9(5): 1937-1958.

Freychet N, Sparrow S, Tett S F B, et al. Impacts of anthropogenic forcings and El Niño on Chinese extreme temperatures. *Advances in Atmospheric Sciences*, 2018, 35: 994-1002.

Gao J, Yang Y, Wang H, et al. Climate responses in China to domestic and foreign aerosol changes due to clean air actions during 2013–2019. *npj Climate and Atmospheric Science*, 2023, 6(1): 160.

García-León D, Casanueva A, Standardi G, et al. Current and projected regional economic impacts of heatwaves in Europe. *Nature communications*, 2021, 12(1): 5807.

Gershunov A, Cayan D R, Iacobellis S F. The great 2006 heat wave over California and Nevada: Signal of an increasing trend. *Journal of Climate*, 2009, 22(23): 6181-6203.

Gillett N P, Shiogama H, Funke B, et al. The detection and attribution model intercomparison project (DAMIP v1. 0) contribution to CMIP6. *Geoscientific Model Development*, 2016, 9(10): 3685-3697.

Giorgi F, Mearns L O. Probability of regional climate change based on the Reliability Ensemble Averaging (REA) method. *Geophysical research letters*, 2003, 30(12).

Gong H, Ma K, Hu Z, et al. Attribution of the August 2022 extreme heatwave in Southern China: role of dynamical and thermodynamical processes. *Bulletin of the American Meteorological Society*, 2024, 105(1): E193-E199.

Gu P, Gan B, Cai W, et al. Role of external forcing in the time-varying trends of global-mean surface temperature under current and future climates. *Environmental Research Letters*, 2024, 19(4): 044038.

Gumbel E J. On the frequency distribution of extreme values in meteorological data. *Bulletin of the American Meteorological Society*, 1942, 23(3): 95-105.

Guo Y, Chen P, Xie Y, et al. Association of daytime-only, nighttime-only, and compound heat waves with preterm birth by urban-rural area and regional socioeconomic status in China. *JAMA Network Open*, 2023, 6(8): e2326987-e2326987.

Hansen A L, Bi P, Nitschke M, et al. The effect of heatwaves on mental health in a temperate Australian city. *Epidemiology*, 2008, 19(6): S85.

Hatvani-Kovacs G, Belusko M, Pockett J, et al. Assessment of heatwave impacts. *Procedia Engineering*, 2016, 169: 316-323.

Hatzianastassiou N, Matsoukas C, Drakakis E, et al. The direct effect of aerosols on solar radiation based on satellite observations, reanalysis datasets, and spectral aerosol optical properties from Global Aerosol Data Set (GADS). *Atmospheric Chemistry and Physics*, 2007, 7(10): 2585-2599.

Hawkins E, Sutton R. The potential to narrow uncertainty in regional climate predictions. *Bulletin of the American Meteorological Society*, 2009, 90(8): 1095-1108.

Hegerl G, Zwiers F. Use of models in detection and attribution of climate change. *Wiley interdisciplinary reviews: climate change*, 2011, 2(4): 570-591.

Hoffmann P, Menz C, Spekat A. Bias adjustment for threshold-based climate indicators. *Advances in Science and Research*, 2018, 15: 107-116.

Hong X, Lu R, Li S. Amplified summer warming in Europe–West Asia and Northeast Asia after the mid-1990s[J]. *Environmental Research Letters*, 2017, 12(9): 094007.

Horton D E, Johnson N C, Singh D, et al. Contribution of changes in atmospheric circulation patterns to extreme temperature trends. *Nature*, 2015, 522(7557): 465-469.

Hu T, Sun Y. Projected changes in extreme warm and cold temperatures in China from 1.5 to 5 C global warming. *International Journal of Climatology*, 2020, 40(8): 3942-3953.

Hua W, Dai A, Qin M, et al. How unexpected was the 2022 summertime heat extremes in the middle reaches of the Yangtze River?. *Geophysical Research Letters*, 2023, 50(16): e2023GL104269.

Intergovernmental Panel on Climate Change (IPCC) (2022) The Ocean and Cryosphere in a Changing Climate. Ocean Cryosph a Chang Clim. https://doi.org/10.1017/9781009157964

Jiang D, Tian Z, Lang X. Reliability of climate models for China through the IPCC Third to Fifth Assessment Reports. *International Journal of Climatology*, 2016, 36(3).

Jehn F U, Schneider M, Wang J R, et al. Betting on the best case: Higher end warming is underrepresented in research. *Environmental Research Letters*, 2021, 16(8): 084036.

Jehn F U, Kemp L, Ilin E, et al. Focus of the IPCC assessment reports has shifted to lower temperatures. *Earth's Future*, 2022, 10(5): e2022EF002876.

Jeong D, Yoo C, Yeh S W. Contributions of external forcing and internal variability to the multidecadal warming rate of East Asia in the present and future climate. *npj Climate and Atmospheric Science*, 2024, 7(1): 22.

John A, Douville H, Ribes A, et al. Quantifying CMIP6 model uncertainties in extreme precipitation projections. *Weather and Climate Extremes*, 2022, 36: 100435.

Krishnan R, Ramanathan V. Evidence of surface cooling from absorbing aerosols. *Geophysical Research Letters*, 2002, 29(9): 54-1-54-4.

Kwon M H, Jhun J G, Ha K J. Decadal change in east Asian summer monsoon circulation in the mid-1990s. *Geophysical Research Letters*, 2007, 34(21).

Lehner F, Deser C, Maher N, et al. Partitioning climate projection uncertainty with multiple large ensembles and CMIP5/6. *Earth System Dynamics*, 2020, 11(2): 491-508.

Lesk C, Anderson W, Rigden A, et al. Compound heat and moisture extreme impacts on global crop yields under climate change. *Nature Reviews Earth & Environment*, 2022, 3(12): 872-889.

Lee J Y, Marotzke J, Bala G, et al. Future global climate: scenario-based projections and near-term information//Climate change 2021: The physical science basis. Contribution of working group I to the sixth assessment report of the intergovernmental panel on climate change. Cambridge University Press, 2021: 553-672.

Li X, Ren G, Wang S, et al. Change in the heatwave statistical characteristics over China during the climate warming slowdown. *Atmospheric Research*, 2021, 247: 105152.

Li Y, Ding Y, Li W. Observed trends in various aspects of compound heat waves across China from 1961 to 2015. *Journal of Meteorological Research*, 2017, 31(3): 455-467.

Liang L, Yu L, Wang Z. Identifying the dominant impact factors and their contributions to heatwave events over mainland China. *Science of the Total Environment*, 2022, 848: 157527.

Liang W, Li C, Wu Y, et al. Anthropogenic forcing and subtropical anticyclonic drivers of the August 2022 heatwave in China. *Weather and Climate Extremes*, 2024, 45: 100707.

Liao W, Li D, Malyshev S, et al. Amplified increases of compound hot extremes over urban land in China. *Geophysical Research Letters*, 2021, 48(6): e2020GL091252.

Liu L, Zhou T, Ning L, et al. Linkage between the Arctic Oscillation and summer climate extreme events over the middle reaches of Yangtze River Valley. *Climate Research*, 2019a, 78(3): 237-247.

Liu Q, Zhou T, Mao H, et al. Decadal variations in the relationship between the western Pacific subtropical high and summer heat waves in East China. *Journal of Climate*, 2019b, 32(5): 1627-1640.

Liu Y, Geng X, Hao Z, et al. Changes in climate extremes in Central Asia under 1.5 and 2 C global warming and their impacts on agricultural productions. *Atmosphere*, 2020, 11(10): 1076.

Luo M, Ning G, Xu F, et al. Observed heatwave changes in arid northwest China: Physical mechanism and long-term trend. *Atmospheric Research*, 2020, 242: 105009.

Luo M, Lau N C, Liu Z. Different mechanisms for daytime, nighttime, and compound heatwaves in southern China. *Weather and Climate Extremes*, 2022, 36: 100449.

Ma F, Yuan X. When will the unprecedented 2022 summer heat waves in Yangtze River basin become normal in a warming climate?. *Geophysical Research Letters*, 2023, 50(4): e2022GL101946.

Ma F, Yuan X, Jiao Y, et al. Unprecedented Europe heat in June–July 2019: Risk in the historical and future context. *Geophysical Research Letters*, 2020, 47(11): e2020GL087809.

Ma S, Zhou T, Stone D A, et al. Attribution of the July–August 2013 heat event in Central and Eastern China to anthropogenic greenhouse gas emissions. *Environmental Research Letters*, 2017, 12(5): 054020.

McEvoy D J, Hatchett B J. Spring heat waves drive record western United States snow melt in 2021. *Environmental Research Letters*, 2023, 18(1): 014007.

Meehl G A, Washington W M, Arblaster J M, et al. Climate system response to external forcings and climate change projections in CCSM4. *Journal of Climate*, 2012, 25(11): 3661-3683.

Meehl G A, Hu A, Arblaster J M, et al. Externally forced and internally generated decadal climate variability associated with the Interdecadal Pacific Oscillation. *Journal of Climate*, 2013, 26(18): 7298-7310.

Miao C, Sun Q, Kong D, et al. 19. RECORD-BREAKING HEAT IN NORTHWEST CHINA IN JULY 2015: ANALYSIS OF THE SEVERITY AND UNDERLYING CAUSES. *Bulletin of the American Meteorological Society*, 2016, 97(12): S97-S101.

NOAA. “State of the Climate: Global Climate Report for Annual 2013.” NOAA National Centers for Environmental Information. 2013.

NOAA. “State of the Climate: Global Climate Report for Annual 2015.” NOAA National Centers for Environmental Information. 2016.

O'Neill B C, Tebaldi C, Van Vuuren D P, et al. The scenario model intercomparison project (ScenarioMIP) for CMIP6. *Geoscientific Model Development*, 2016, 9(9): 3461-3482.

O’Neill B C, Kriegler E, Ebi K L, et al. The roads ahead: Narratives for shared socioeconomic pathways describing world futures in the 21st century. *Global environmental change*, 2017, 42: 169-180.

O’Reilly C H, Brunner L, Qasmi S, et al. Assessing observational constraints on future European climate in an out-of-sample framework. *npj Climate and Atmospheric Science*, 2024, 7(1): 95.

Otto F E L, Massey N, van Oldenborgh G J, et al. Reconciling two approaches to attribution of the 2010 Russian heat wave. *Geophysical Research Letters*, 2012, 39(4).

Peterson T C, Stott P A, Herring S. Explaining extreme events of 2011 from a climate perspective. *Bulletin of the American Meteorological Society*, 2012, 93(7): 1041-1067.

Perkins S E, Alexander L V. On the Measurement of Heat Waves. *Journal of Climate*, 2013, 26(13), 4500–4517.

Perkins-Kirkpatrick S E, Lewis S C. Increasing trends in regional heatwaves. *Nature communications*, 2020, 11(1): 3357.

Piao S, Ciais P, Huang Y, et al. The impacts of climate change on water resources and agriculture in China. *Nature*, 2010, 467(7311): 43-51.

Raftery A E, Zimmer A, Frierson D M W, et al. Less than 2 C warming by 2100 unlikely. *Nature climate change*, 2017, 7(9): 637-641.

Ribes A, Qasmi S, Gillett N P. Making climate projections conditional on historical observations. *Science Advances*, 2021, 7(4): eabc0671.

Ren G, Guan Z, Shao X, et al. Changes in climatic extremes over mainland China. *Climate Research*, 2011, 50(2-3): 105-111.

Ren G, Ding Y, Tang G. An overview of mainland China temperature change research. *Journal of Meteorological Research*, 2017, 31(1): 3-16.

Ren L, Wang D, An N, et al. Anthropogenic influences on the persistent night-time heat wave in summer 2018 over Northeast China. *Bulletin of the American Meteorological Society*, 2020, 101(1): S83-S88.

Salzano R, Cerrato R, Scoto F, et al. Detection of Winter Heat Wave Impact on Surface Runoff in a Periglacial Environment (Ny-Ålesund, Svalbard). *Remote Sensing*, 2023, 15(18): 4435.

Schneider S H. Cloudiness as a global climatic feedback mechanism: The effects on the radiation balance and surface temperature of variations in cloudiness. *Journal of Atmospheric Sciences*, 1972, 29(8): 1413-1422.

Schwarz L, Malig B, Guzman-Morales J, et al. The health burden of fall, winter and spring extreme heat events in Southern California and contribution of Santa Ana Winds. *Environmental Research Letters*, 2020, 15(5): 054017.

Sehler R, Li J, Reager J T, et al. Investigating relationship between soil moisture and precipitation globally using remote sensing observations. *Journal of Contemporary Water Research & Education*, 2019, 168(1): 106-118.

Seneviratne S I, Donat M G, Mueller B, et al. No pause in the increase of hot temperature extremes. *Nature Climate Change*, 2014, 4(3): 161-163.

Singh S, Mall R K, Singh N. Changing spatio-temporal trends of heat wave and severe heat wave events over India: An emerging health hazard. *International Journal of Climatology*, 2021, 41: E1831-E1845.

Smith S J, Bond T C. Two hundred fifty years of aerosols and climate: the end of the age of aerosols. *Atmospheric Chemistry and Physics*, 2014, 14(2): 537-549.

Solomon, Susan, ed. Climate change 2007-the physical science basis: Working group I contribution to the fourth assessment report of the IPCC. Vol. 4. Cambridge university press, 2007.

Song F, Zhang G J, Ramanathan V, et al. Trends in surface equivalent potential temperature: A more comprehensive metric for global warming and weather extremes. *Proceedings of the National Academy of Sciences*, 2022, 119(6): e2117832119.

Song Y, Achberger C, Linderholm H W. Rain-season trends in precipitation and their effect in different climate regions of China during 1961–2008. *Environmental Research Letters*, 2011, 6(3): 034025.

Su Q, Dong B. Recent decadal changes in heat waves over China: Drivers and mechanisms. *Journal of Climate*, 2019a, 32(14): 4215-4234.

Su Q, Dong B. Projected near-term changes in three types of heat waves over China under RCP4. 5. *Climate Dynamics*, 2019b, 53(7): 3751-3769.

Sun Y, Zhang X, Zwiers F W, et al. Rapid increase in the risk of extreme summer heat in Eastern China. *Nature Climate Change*, 2014, 4(12): 1082-1085.

Sun Y, Song L, Yin H, et al. 20. Human influence on the 2015 extreme high temperature events in Western China. *Bulletin of the American Meteorological Society*, 2016, 97(12): S102-S106.

Sun Y, Hu T, Zhang X. Substantial increase in heat wave risks in China in a future warmer world. *Earth's Future*, 2018, 6(11): 1528-1538.

Sun Y, Zhang X, Ding Y, et al. Understanding human influence on climate change in China. *National science review*, 2022, 9(3): nwab113.

Tan J, Kalkstein L S, Huang J, et al. An operational heat/health warning system in Shanghai. *International Journal of Biometeorology*, 2004, 48: 157-162.

Tan J, Zheng Y, Song G, et al. Heat wave impacts on mortality in Shanghai, 1998 and 2003. *International journal of biometeorology*, 2007, 51: 193-200.

Tang S, Qiao S, Wang B, et al. Linkages of unprecedented 2022 Yangtze River Valley heatwaves to Pakistan flood and triple-dip La Niña. *npj Climate and Atmospheric Science*, 2023, 6(1): 44.

Taylor K E. Summarizing multiple aspects of model performance in a single diagram. *Journal of Geophysical Research*, 2001, 106(D7): 7183-7192.

Tripathy K P, Mukherjee S, Mishra A K, et al. Climate change will accelerate the high-end risk of compound drought and heatwave events. *Proceedings of the National Academy of Sciences*, 2023, 120(28): e2219825120.

Ullah I, Saleem F, Iyakaremye V, et al. Projected changes in socioeconomic exposure to heatwaves in South Asia under changing climate. *Earth's Future*, 2022, 10(2): e2021EF002240.

UNFCCC (United Nations Framework Convention on Climate Change). 2015. "Adoption of the Paris Agreement." Conference of the Parties, Paris, France, November 30–December 11

Wang C, Li Z, Chen Y, et al. Drought-heatwave compound events are stronger in drylands. *Weather and Climate Extreme*s, 2023a, 42: 100632.

Wang D, Sun Y, Hu T, et al. The 2022 record-breaking heat event over the middle and lower reaches of the Yangtze River: the role of anthropogenic forcing and atmospheric circulation. *Bulletin of the American Meteorological Society*, 2024, 105(1): E200-E205.

Wang J, Chen Y, Tett S F B, et al. Anthropogenically-driven increases in the risks of summertime compound hot extremes. *Nature communications*, 2020, 11(1): 528.

Wang J, Yan Z. Rapid rises in the magnitude and risk of extreme regional heat wave events in China. *Weather and Climate Extremes*, 2021, 34: 100379.

Wang P, Tang J, Sun X, et al. Heat waves in China: definitions, leading patterns, and connections to large-scale atmospheric circulation and SSTs. *Journal of Geophysical Research: Atmospheres*, 2017, 122(20): 10,679-10,699.

Wang P, Hui P, Xue D, et al. Future projection of heat waves over China under global warming within the CORDEX-EA-II project. *Climate Dynamics*, 2019, 53: 957-973.

Wang P, Zhang W, Liu J, et al. Analysis and intervention of heatwave related economic loss: Comprehensive insights from supply, demand, and public expenditure into the relationship between the influencing factors. *Journal of Environmental Management*, 2023b, 326: 116654.

Wang Q, Wang Z, Zhang H. Impact of anthropogenic aerosols from global, East Asian, and non-East Asian sources on East Asian summer monsoon system. *Atmospheric Research*, 2017, 183: 224-236.

Wang W, Zhou W, Li X, et al. Synoptic-scale characteristics and atmospheric controls of summer heat waves in China. *Climate dynamics*, 2016, 46: 2923-2941.

Wang Z, Wang C, Yang S, et al. Evaluation of surface solar radiation trends over China since the 1960s in the CMIP6 models and potential impact of aerosol emissions. *Atmospheric Research*, 2022, 268: 105991.

Wei J, Han W, Wang W, et al. Intensification of heatwaves in China in recent decades: Roles of climate modes. *npj Climate and Atmospheric Science*, 2023, 6(1): 98.

Wu S, Luo M, Zhao R, et al. Local mechanisms for global daytime, nighttime, and compound heatwaves[J]. *npj Climate and Atmospheric Science*, 2023a, 6(1): 36.

Wu S, Luo M, Wang X, et al. Season-dependent heatwave mechanisms: a study of southern China. *Weather and Climate Extremes*, 2023b, 42: 100603.

Xia J, Tu K, Yan Z, et al. The super-heat wave in eastern China during July-August 2013: a perspective of climate change. *International Journal of Climatology*, 2016, 36(3).

Xie W, Zhou B, You Q, et al. Observed changes in heat waves with different severities in China during 1961–2015. *Theoretical and Applied Climatology*, 2020, 141: 1529-1540.

Xie W, Zhou B, Han Z, et al. Projected changes in heat waves over China: Ensemble result from RegCM4 downscaling simulations. *International Journal of Climatology*, 2021, 41(7): 3865-3880.

Xie W, Zhou B, Han Z, et al. Substantial increase in daytime-nighttime compound heat waves and associated population exposure in China projected by the CMIP6 multimodel ensemble. *Environmental Research Letters*, 2022, 17(4): 045007.

Xu H, Zhang G. Comparison of relative and absolute heatwaves in eastern China: observations, simulations and future projections. *Atmosphere,* 2022, 13(5): 649.

Xu W, Lei X, Chen S, et al. How well does the ERA5 reanalysis capture the extreme climate events over China? Part II: Extreme temperature. *Frontiers in Environmental Science*, 2022, 10: 921659.

Yang J, Yin P, Sun J, et al. Heatwave and mortality in 31 major Chinese cities: definition, vulnerability and implications. *Science of The Total Environment*, 2019, 649: 695-702.

Yang X, Zhou B, Xu Y, et al. CMIP6 evaluation and projection of temperature and precipitation over China. *Advances in Atmospheric Sciences*, 2021, 38: 817-830.

Yang Y, Jin C, Ali S. Projection of heat wave in China under global warming targets of 1.5° C and 2° C by the ISIMIP models. *Atmospheric Research*, 2020, 244: 105057.

Yao Z, Li X, Xiao J. Characteristics of daily extreme wind gusts on the Qinghai-Tibet Plateau, China. *Journal of Arid Land*, 2018, 10: 673-685.

Ye D, Yin J, Chen Z, et al. Spatial and temporal variations of heat waves in China from 1961 to 2010. *Advances in Climate Change Research*, 2014, 5(2): 66-73.

Yin J, Gentine P, Slater L, et al. Future socio-ecosystem productivity threatened by compound drought–heatwave events. *Nature Sustainability,* 2023a, 6(3): 259-272.

Yin Z, Yang S, Wei W. Prevalent atmospheric and oceanic signals of the unprecedented heatwaves over the Yangtze River Valley in July–August 2022. *Atmospheric Research*, 2023b, 295: 107018.

You Q, Jiang Z, Kong L, et al. A comparison of heat wave climatologies and trends in China based on multiple definitions. *Climate Dynamics*, 2017, 48: 3975-3989.

You Q, Cai Z, Wu F, et al. Temperature dataset of CMIP6 models over China: evaluation, trend and uncertainty. *Climate Dynamics*, 2021, 57: 17-35.

Yu X, Zeng X, Gui D, et al. Projection of flash droughts in the headstream area of Tarim River Basin under climate change through Bayesian uncertainty analysis. *Journal of Geophysical Research: Atmospheres*, 2023, 128(6): e2022JD037634.

Zampieri M, Ceglar A, Dentener F, et al. Wheat yield loss attributable to heat waves, drought and water excess at the global, national and subnational scales. *Environmental Research Letters*, 2017, 12(6): 064008.

Zhang D, Huang Y, Zhou B, et al. Who is the major player for 2022 China extreme heat wave? Western Pacific Subtropical high or South Asian high?. *Weather and Climate Extremes*, 2024a, 43: 100640.

Zhang G, Han L, Yao J, et al. Assessing future heat stress across China: combined effects of heat and relative humidity on mortality. *Frontiers in Public Health*, 2023a, 11: 1282497.

Zhang L, Yu X, Zhou T, et al. Understanding and attribution of extreme heat and drought events in 2022: current situation and future challenges. *Advances in Atmospheric Sciences*, 2023b, 40(11): 1941-1951.

Zhang K, Zuo Z, Suarez-Gutierrez L, et al. The significant influence of the Atlantic multidecadal variability to the abrupt warming in Northeast Asia in the 1990s. *npj Climate and Atmospheric Science*, 2024b, 7(1): 28.

Zhang M, Dong B, Schiemann R, et al. Summer compound heatwaves over China: projected changes at different global warming levels and related physical processes. *Climate Dynamics*, 2024c, 62(3): 1887-1907.

Zhao A, Bollasina M A, Stevenson D S. Strong influence of aerosol reductions on future heatwaves. *Geophysical Research Letters*, 2019, 46(9): 4913-4923.

Zhao Q, Guo Y, Ye T, et al. Global, regional, and national burden of mortality associated with non-optimal ambient temperatures from 2000 to 2019: a three-stage modelling study. *The Lancet Planetary Health*, 2021, 5(7): e415-e425.

Zhao Q, Li S, Ye T, et al. Global, regional, and national burden of heatwave-related mortality from 1990 to 2019: A three-stage modelling study. *PLoS medicine*, 2024, 21(5): e1004364.

Zhao C, Liu B, Piao S, et al. Temperature increase reduces global yields of major crops in four independent estimates. *Proceedings of the National Academy of Sciences*, 2017, 114(35): 9326-9331.

Zhao W. Extreme weather and climate events in China under changing climate. *National Science Review*, 2020, 7(5): 938-943.

Zhou B, Wen Q H, Xu Y, et al. Projected changes in temperature and precipitation extremes in China by the CMIP5 multimodel ensembles. *Journal of Climate*, 2014, 27(17): 6591-6611.

Zhou B, Hu S, He Y, et al. Quantitative evaluations of subtropical westerly jet simulations over East Asia based on multiple CMIP5 and CMIP6 GCMs. *Atmospheric Research*, 2022a, 276: 106257.

Zhou W, Chan J C L, Chen W, et al. Synoptic-scale controls of persistent low temperature and icy weather over southern China in January 2008. *Monthly Weather Review*, 2009, 137(11): 3978-3991.

Zhou Y, Yuan J, Wen Z, et al. The impacts of the East Asian subtropical westerly jet on weather extremes over China in early and late summer. *Atmospheric and Oceanic Science Letters*, 2022b, 15(5): 100212.

Zhu B, Sun B, Wang H. Dominant modes of interannual variability of extreme high-temperature events in eastern China during summer and associated mechanisms. *International Journal of Climatology*, 2020, 40(2): 841-857.